

**MICROFABRICATION OF A HIGH SENSITIVITY FLUIDIC AFM
PROBE**

A Dissertation
Presented to
The Academic Faculty

by

David Kipp Schoenwald

In Partial Fulfillment
of the Requirements for the Degree
Doctor of Philosophy in the
School of George W Woodruff School of Mechanical Engineering

Georgia Institute of Technology
December 2015

Copyright 2015 by David Kipp Schoenwald

MICROFABRICATION OF A HIGH SENSITIVITY FLUIDIC AFM PROBE

Approved by:

Dr. Todd Sulchek, Advisor
School of Mechanical Engineering
Georgia Institute of Technology

Dr. Wilbur Lam
School of BioMedical Engineering
Georgia Institute of Technology

Dr. Oliver Brand
School of Electrical & Computer
Engineering
Georgia Institute of Technology

Dr. Hang Lu
Chemical & Biomolecular Engineering
Georgia Institute of Technology

Dr. Peter Hesketh
School of Mechanical Engineering
Georgia Institute of Technology

Date Approved: November 10, 2015

To future giants

ACKNOWLEDGEMENTS

I would like to thank my parents, Nicholas and Annette, and siblings for their constant love and support. Particular thanks to my advisor, Dr. Todd Sulchek, for his perceptive criticisms, in-depth knowledge of the literature, and endless new ideas. I am obliged to my committee, Drs. Lu, Hesketh, Lam and Brand for generously giving of their time and expertise to my project. Special thanks are due to members of the cleanroom staff namely, Mr. Vinh Nguyen, Janet Cobb-Sullivan, Mikkell Thomas, Eric Woods, Hang Chen, Thomas Averette and William Kimes. Special thanks to Dr. Andres Garcia and his professional support and the financial support of the National Institute of Health, Cell and Tissue Engineering grant and also the NSF (Project 1063279). Much gratitude to the many researchers who have contributed to this area of work and made these steps possible. And finally, special thanks to my friends and colleagues that have graciously shared their time and knowledge: Yaser Bastani, Daniel Potter, Milad Navaei and Sarah Griffiths.

TABLE OF CONTENTS

Acknowledgements	iv
List of Tables	ix
List of Figures	x
Nomenclature	xiii
Summary	xv
CHAPTER 1 Introduction	1
1.1 Overview of Atomic Force Microscopy	1
1.2 Instrumentation in Cellular Force Spectroscopy	2
1.3 A Multimodal Analysis	4
1.4 History of Aspirating Force Probes	7
1.5 Limitations in Aspirating Force Probe Sensitivity and Integration with Existing AFM's	9
1.6 Overall Research Contributions	10
1.7 Thesis Outline	13
CHAPTER 2 High Sensitivity Composite Material Force Probe with Nanofluidic Channel	15
2.1 Objective	15
2.2 Fundamentals of AFM Probe Force Sensitivity	15
2.2.1 Lower Limit of Probe Sensitivity	16
2.3 Importance of Cantilever Stiffness	18
2.4 Parametric Analysis of Cantilever Stiffness	19
2.4.1 Euler-Bernoulli Beam Theory for a Rectangular Cantilever	19
2.4.2 Numerical Model for Parametric Analysis via Beam Theory for a Hollowed Cantilever	20
2.5 Analytical Model for Verification	22
2.5.1 Parametric Evaluation of Numerical Model	23
2.5.2 Parametric Design for Low Stiffness Hollowed Cantilever	24
2.6 Techniques in Micro and Nanochannel Fabrication	27
2.7 Sacrificial Thermally Decomposable Polymer Approach	28

2.7.1 Challenges in Polymer Based Sacrificial Channels	30
2.8 Design and Fabrication	32
2.8.1 Chip Architecture	32
2.8.2 Fabrication Process	33
2.9 Results and Discussion	36
2.9.1 Residual Film Stress Induced Bending of Composite Material Cantilevers	39
2.9.2 Mitigation of Residual Stress for a Cantilever of a Composite Material Architecture	40
2.9.3 Determining the mean and gradient stress in thin films	40
2.9.4 Design for Low Net Residual Stress in Composite Cantilevers by Complementary Stress Polarity	42
2.9.5 Design for Low Net Residual Stress in Composite Cantilevers by Minimizing Effects of High Stress Layers	43
2.9.6 Mitigation of Residual Stress by High Temperature Annealing	45
2.9.7 Within-Wafer Non-Uniformity	47
2.10 Characterization of Low Stiffness and Composite MEMS Cantilever	52
2.11 Conclusions	54
CHAPTER 3 Micro- to Nano-fluidic Interface via A Thermally Decomposable Sacrificial Polymer	56
3.1 Objective	56
3.2 Overarching Approach	57
3.3 Two Part Unity Fabrication Method	58
3.3.1 Plug Formation	60
Prewetting	61
Limitations in Unity Processing	62
3.3.2 Film Stress Concentration Reduction by Plug Planarization	68
3.3.3 Integration of a Two Part Unity Approach with Complete Chip Fabrication Process	70
3.3.4 Fabrication Challenges	73
3.3.5 Selection of Wafer Bond Chemistry	73

Methods	74
Bond Chemistries	76
3.4 Oxide Etch Stop Fabrication Method	86
3.4.1 Integration of Etch Stop Approach with Complete Chip Fabrication Process	87
3.4.2 Elective Cantilever Head Start Technique	90
3.5 Fabrication Approach Distinctions	91
3.6 Integrated Macro to Nano-Fluidic	94
3.6.1 Pressure Control System	96
3.6.2 Optimization of the pressure control system	98
3.6.3 Side-Entry Direct to Chip Interconnect	99
3.6.4 Hermetic Bond Characterization	100
3.6.5 Noise Floor	101
Minimum Detectible Displacement	102
3.7 Flow Characterization	103
3.8 Conclusions	107
CHAPTER 4 Integration of Atomic force microscopy and a microfluidic liquid cell for aqueous imaging and force spectroscopy	109
4.1 Objective	109
4.2 Microfluidic Liquid Cells for AFM	109
4.3 History of Liquid Cells	111
4.4 Challenges in Fabrication of Microfluidic Liquid Cells	111
4.5 Previous Approaches in Fluidic Channel Volume Reduction	111
4.6 Approach to Fluidic Channel Volume Reduction	112
4.7 Design and Fabrication	113
4.8 Deflection Sensitivity Characterization of Liquid Cell	116
4.9 Characterization within Aqueous Environment	118
4.10 Characterization of Laminar Dynamics	119
4.11 Discussion	120
4.12 Conclusions	123

CHAPTER 5 Conclusions	124
5.1 Summary	124
5.2 Key Achievements	127
5.3 Future Characterization	128
5.4 Limitations	129
5.5 Recommended Experiments	131
5.5.1 Aspiration and Serial stiffness measurement on single, non-adherent Cell using the AFP	131
5.5.2 Single Cell Measurement of VOCs via MicroGC Under Elicited Chemical and Physical Stress	132
5.5.3 Flagellated Cell Thrust and Sperm fusion binding affinity	133
Appendices	135
References	139
Vita	156

LIST OF TABLES

Table 1 Instrument Force Sensitivity Range by Assay Type	4
Table 2 Force Ranges in Cellular Biology	4
Table 3 Probe Sensitivity	9
Table 4 Parametric Contributions to Cantilever Stiffness	23
Table 5 Bending Moment Comparison	27
Table 6 Layer processing parameters	35
Table 7 Stress measurement according to layer	42
Table 8 Comparison of Theoretical and Actual Spring Constants	53
Table 9 Fidelity of Bond Approach	77
Table 10 XDS data for 3 regions illustrated in Figure 3-12 (wt%)	80
Table 11 Surface Preparation and Chemical Activation Methods	82

LIST OF FIGURES

Figure 1-1 AFM Force Spectroscopy by Cantilever Deflection	2
Figure 1-2 Experimental Setup of Force Spectroscopy Assays	3
Figure 1-3 Multimodal Analysis	6
Figure 1-4 Schematic of an AFM vs. AFP:	7
Figure 1-5 The Overall Thesis Flowchart	14
Figure 2-1 Schematic of Cell Mechanics Assay.	16
Figure 2-2 Illustration of Thermal Fluctuation Noise Amplitude	17
Figure 2-3 Cartoon of Hollowed Cantilever	20
Figure 2-4 Inertial Component Partitions for Euler-Bernoulli Analysis	21
Figure 2-5 COMSOL FEA Validation of Hollowed Cantilever Model	22
Figure 2-6 Area Moment of Inertia (μm^4)	24
Figure 2-7 Area Moment of Inertia (μm^4)	26
Figure 2-8 Comparison of Sacrificial Layer Methods for Nanofluidic Channels	30
Figure 2-9 Illustration of Thermogravimetric Analysis of Unity Decomposition	31
Figure 2-10 Layout of Cantilever and Chip Architecture	33
Figure 2-11 Low Stiffness Cantilever Fabrication Process	34
Figure 2-12 Bending Radii Exhibited in Cantilevers	36
Figure 2-13 PECVD Nitride Thickness Profile	37
Figure 2-14 Evaluation of Contributing Factors to Cantilever Bending Radius	38
Figure 2-15 Total Film Residual Stress	41
Figure 2-16 Film Residual Stress	42
Figure 2-17 Residual Stress Induced Fracturing	43
Figure 2-18 Sectional View of Solidworks Model	45
Figure 2-19 Mitigation of Residual Stress by High Temperature Anneal	47
Figure 2-20 Combined Thermal Decomposition and Anneal in Series	47
Figure 2-21 Deposition Rates and Thickness Uniformities	50
Figure 2-22 LPCVD and PECVD Nitride Film Uniformity	51
Figure 2-23 Force-deflection Curve	52

Figure 2-24 Composite Material Hollow Cantilever	54
Figure 3-1 Cross Section Diagram Illustrating Micro to Nano-fluidic Interface	58
Figure 3-2 Two-Part Unity Method for Micro to Nano-Fluidic Interface	60
Figure 3-3 Processing Limits for Unity Plug	63
Figure 3-4 Custom Vacuum/Pressure Chamber	64
Figure 3-5 Resist Topography Dependence on Resist Viscosity and Hole Diameter	67
Figure 3-6 Plug Profile Dependence on Spin Thickness and Well Diameter	68
Figure 3-7 Topcoat Structural Stability Dependence on Plug Profile	70
Figure 3-8 Two-Step Unity Microfabrication Process Flow for an AFP	71
Figure 3-9 Vent Structure	72
Figure 3-10 Schematic of Bond Quality Evaluation	75
Figure 3-11 Schematic of Bond Quality Evaluation	76
Figure 3-12 Aluminum and Tin Bond	79
Figure 3-13 Direct Silicon Bond	83
Figure 3-14 Surface Roughness and Feature Profile on Bonding Interface	85
Figure 3-15 Oxide Etch Stop Method for Micro to Nano-Fluidic Interface	87
Figure 3-16 Oxide Etch Stop Microfabrication Process Flow for an AFP	88
Figure 3-17 Distinction in Well Formation Fidelity Between the Two Approaches	93
Figure 3-18 Complete Macro- to Nano-Fluidic System	95
Figure 3-19 AFP Probe Mounted to AFM System Chuck	96
Figure 3-20 Two Pressure Systems Evaluated for Pressure Control	97
Figure 3-21 Pressure Control System	99
Figure 3-22 Schematic of Fluidic Interconnect	101
Figure 3-23 AFP Noise Floor	102
Figure 3-24 Deionized Water Flow Through a 500 nm by 3 μm Channel	106
Figure 4-1 Microfluidic Liquid Cell Plan and Side View Schematics	113
Figure 4-2 Fabrication of Microfluidic Liquid Cell.	116
Figure 4-3 Deflection Sensitivity of Cantilever in Liquid Cell.	117
Figure 4-4 Force Curve within a Microfluidic Liquid Cell.	119
Figure 4-5 Microparticle flow within Fluidic Liquid Cell.	120

Figure 5-1 Hypothesized Adhesion and Stiffness Relationship for Single Cell	132
Figure 5-2 Custom SPME Adapter	133
Figure 5-3 Spermatozoa Assay	134

NOMENCLATURE

AFP	aspirating force probe
AFM	atomic force microscope
BFP	bio force probe
BME	beta-mercaptoethanol
BOE	buffered oxide etchant
BSA	bovine serum albumin
CVD	chemical vapor deposition
deepRIE	deep reactive ion etching
DMAc	dimethylacetamide
DMSO	dimethylsulfoxide
DPA	dual pipette assay
GC	gas chromatography
ICP	inductively coupled plasma
LLLT	low level light therapy
LPCVD	low pressure chemical vapor deposition
MEMS	microelectromechanical systems
OT	optical tweezers
PBS	phosphate buffered saline
PDMS	polydimethylsiloxane
PECVD	plasma enhanced chemical vapor deposition
PEEK	polyether ether ketone

PMMA	poly(methyl methacrylate)
PSD	photo sensing diode
PTFE	polytetrafluoroethylene
RIE	reactive ion etching
ROS	reactive oxygen species
SPME	solid-phase microextraction
TCD	thermal conductivity detector
UV	ultraviolet
VOC	volatile organic compounds
WIWNU	within-wafer non-uniformity
μ GC	micro gas chromatograph

SUMMARY

This dissertation presents significant advancements in AFM probe fabrication technologies toward an AFM based assay that combines a spectrum of AFM capabilities into a comprehensive multimodal single cell analysis. The objective of this work is the fabrication of the world's softest hollow cantilever with a beam stiffness, k , less than 100 pN/nm that is two orders of magnitude smaller than previously published. In pursuit of this objective, the intellectual contributions of this work include: 1) formation of the first high resolution (1.87 pN noise floor), low stiffness ($k = 53.54$ pN/nm) nano-channel cantilever made from thermally decomposable sacrificial polymer; 2) a parametric analysis of the hollow cantilever that highlights critical design features to minimize beam stiffness; 3) two new methods of interfacing a bulk microfluidic channel to a surface nanofluidic channel via a thermally decomposable polymer; and 4) a microfluidic side entry glass capillary interconnect to a bulk microfluidic channel. The technology incorporates the ability to manipulate the internal fluid pressure at the cantilever terminus to enable controlled aspiration of single cells.

This work could enable the simultaneous measurement of cell mechanical properties, including mass, compressive modulus, viscoelasticity, tensile modulus, and adhesion in a single experiment. Further, an integrated analogue pressure control system is developed, using an original side-entry interconnect structure for direct-to-chip connection of glass capillary for fluidic probes as well as other lab on chip applications. The low stiffness nano-channel cantilever was fabricated, tested, and found to be more than two orders of

magnitude more force sensitive than that published to date, and is comparable to standard COTS probes for the application of cell stiffness measurements.

Within the scope of this thesis, fabrication of an integrated liquid cell was developed that integrates a 50 nL microfluidic channel around a cantilever for atomic force microscopy in aqueous environment. This is a reduction is over 3-5 orders of magnitude compared to commercial liquid cells. This device facilitates testing at high shear rates and laminar flow conditions coupled with full AFM functionality in microfluidic aqueous environments, including execution of both force displacement curves and high-resolution imaging.

CHAPTER 1 INTRODUCTION

1.1 OVERVIEW OF ATOMIC FORCE MICROSCOPY

The atomic force microscope or AFM was developed in 1986 by Binnig *et al* [1]. Derived from a scanning probe microscope and a profilometer, the AFM has evolved much over the past 30 years, becoming a commercially available and pervasive instrument in the scientific community. It has revolutionized the field of cellular and molecular biology, enabling scientists to see and feel on the micro, nano, and atomic scale. Despite numerous advancements, the fundamental mechanism of AFM operation has remained much the same. As an AFM probe is brought into contact with a sample, a laser beam is reflected off the back of the cantilever and a voltage reading proportional to cantilever deflection is detected by a photo sensing diode. For imaging of a specimen, the cantilever is raster scanned in the X-Y plane via a piezo electric actuator. The spatial data is combined with the deflection data from the photo sensing diode to generate a complete three dimensional image, depicted in Figure 1-1a. Furthermore, the stiffness, k , of the cantilever can be measured via the Sader method [2] and used to derive the applied force to a specimen according to Hooke's law and the relevant contact model [3]. A properly selected probe may apply a force commensurate to the mechanical property of a specimen, Figure 1-1b. The derived force-deflection curve precisely quantifies the specimen stiffness or the adhesion strength of molecular bonds [4].

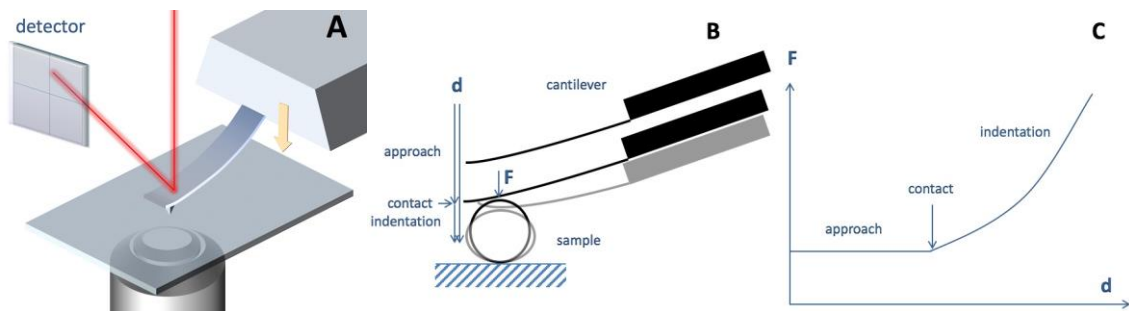


Figure 1-1 AFM Force Spectroscopy by Cantilever Deflection: (a) AFM system consisting of a probe with a cantilever and tip is raster scanned over a sample; a photo sensing diode (PSD) detects reflected laser with nanometer scale cantilever deflection. The recorded x, y, and z data form the image. (b) A force measurement is performed by bringing the probe into contact with the specimen and applying a compressive force. The cantilever deflects upward as the specimen indents downward. (c) A force-indentation curve is determined by Hooke's Law and the relevant contact model.

1.2 INSTRUMENTATION IN CELLULAR FORCE SPECTROSCOPY

Cellular force spectroscopy assays aim to accurately quantify various biomechanical responses including: adhesion frequency, contractile forces, adhesion forces (cell-cell and molecular), membrane tension, mechanically induced physiology, transmembrane diffusion, and interaction energy. Among a plethora of devices used in cellular force spectroscopy, the most established are optical tweezers, Figure 1-2a, the micropipette, Figure 1-2b and c, the pillared substrate, Figure 1-2d, the tipless (or beaded tip) AFM [5], [6], Figure 1-2e, and the more nascent method termed FluidFM, Figure 1-2f.

Measuring the physical properties of cells can be difficult using AFM, due to the incongruence of the cantilever tip with the cell. Alternative approaches to cell biophysical measurements include the use of micropipettes to grasp and manipulate cells. Various configurations may be arranged including the well-known biomembrane force probe (BFP) and the dual pipette assay (DPA) which are capable of measuring adhesive forces in the range of 10^{-2} pN to 100 nN [7]. In the case of the BFP, an erythrocyte with known stiffness and a nonspecifically bonded

microbead act as a force probe. The DPA uses known capillary and environment pressures to determine forces. The optical tweezers method utilizes a highly focused laser beam to optically trap a dielectric bead, which may be adhered to a cell. The beam is capable of inducing picoNewton forces on the bead [8]. The pillared substrates method quantifies the cell-cell interaction forces by measuring the traction forces, as evidenced by the bending of vertical pillars with known bending stiffness [9], [10]. In measuring cellular adhesion forces, a tipless or micro-beaded cantilever is used [11].

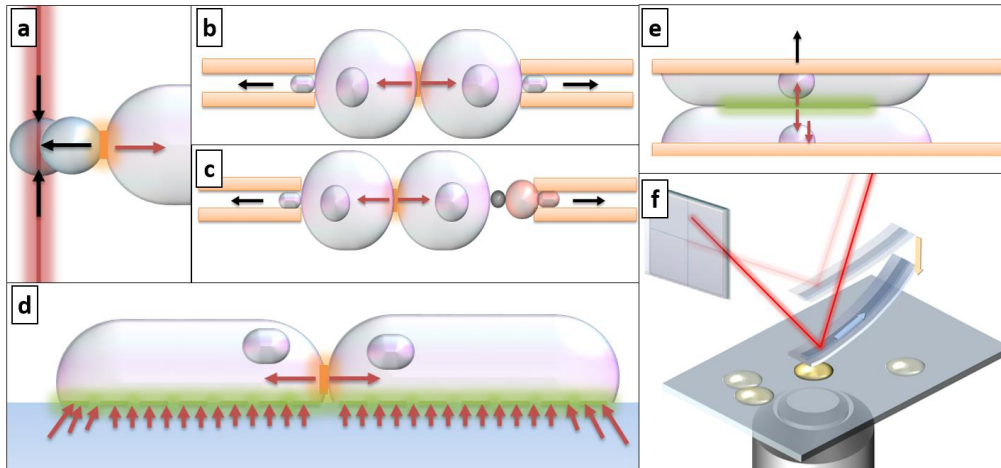


Figure 1-2 Experimental Setup of Force Spectroscopy Assays

(a) Optical tweezers, (b & c) micropipette: DPA & BFP, (d) pillared substrates, (e) AFM, (f) FluidFM. Illustrations adapted from [12], [13].

The force ranges of each assay vary according to Table 1. The AFM, enables the widest force range of all methods described [14].

Table 1 Instrument Force Sensitivity Range by Assay Type

Method	Force Range	
BFP	10^{-2} pN to 100 pN	[14]
DPA	pN to 10 nN	[13]
AFM	1 pN to 100 nN	[13]
OT	10^{-2} pN to 100 pN	[14]

1.3 A MULTIMODAL ANALYSIS

The atomic force microscope has revolutionized the field of cellular biology. The original AFM alone demonstrated deflections as low as 10^{-4} Å, having image resolutions greater than the optical diffraction limit. Force measurements were demonstrated as low as 10^{-6} pN [1]. This capability has allowed researchers to directly measure cellular and molecular interactions, Table 2.

Table 2 Force Ranges in Cellular Biology

	Force Range
Molecular Interactions	pN to nN [15]
Cell Compressive Forces	nN to 100 nN [3]

This ability to obtain information at the single-cell level is of central importance for numerous biological questions and represents a major challenge that requires development of new and more capable instruments. AFM capabilities are expanding with the ability to measure compressive modulus [3], [6], cell membrane tension [16], viscoelasticity [17], adhesion forces[11], and mass [18].

Quantification of both spatial and temporal responses of single cell [14] and cell-cell [19] interactions by force spectroscopy enables the understanding of basal cell functions as well as pathophysiology for better clinical treatment. Direct correlations have been uncovered between cellular mechanics and physiology, answering some of the toughest and most fundamental questions in pathological mechanisms and providing solutions for both detection and treatment.

Though these measurements (cell modulus, cell tension, viscoelasticity, adhesion, and mass) have all been previously performed, they have not been performed concurrently on a single cell. If one considers micropipette assays such as the biomembrane force probe (BFP) [20] and dual pipette assay (DPA) [13], we observe additional capacities to perform serial measurement by reversible binding, mechanical attachment, and the ability to work with both adherent and non-adherent cells. An AFM, in comparison, offers a greater force range as well as precise spatial and temporal control [14]. By retrofitting a standard AFM probe with a microfluidic channel, we can amalgamate these capabilities into one device to perform a comprehensive multimodal single cell analysis, by simultaneous measurement of mass, compressive modulus, viscoelasticity, tensile modulus, and adhesion simultaneously in a single experiment, Figure 1-3. The measurement begins by first determining the resonant frequency of the probe in the medium by a Lorenz fit of a thermal curve. A cell is then aspirated and the measurement is repeated to determine the cell mass by shift in resonant frequency. The cell can then be brought to a substrate and compressed to determine the compressive modulus. This is followed by a retraction of the probe by only a few microns to measure the cells viscoelastic response. This is followed by further retraction of the probe, employing the aspirating capability of the probe to impose a tensile force on the cell membrane. Furthermore,

a microfluidic liquid cell enables high shear fluid flow across the cantilever, introducing an additional parameter to the multimodal capability of the described system.

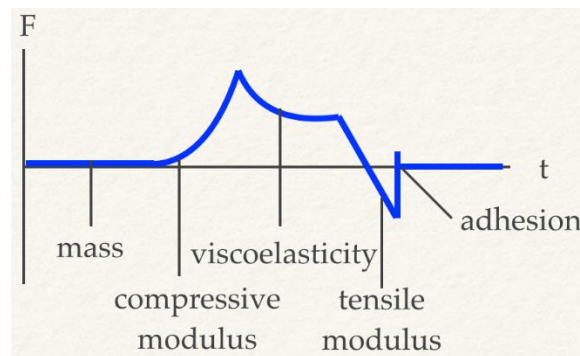


Figure 1-3 Multimodal Analysis: An aspirating force probe (AFP) introduces the additional capacity to measure mass.

An aspirating force probe (AFP) is an AFM probe with an interior micro or nano channel, (Figure 1-4, right), which enables suction pressure to be applied to a biological sample. With the full advantage of the AFM system, the microchanneled cantilever AFP probe has the additional capacity to hold individual cells through aspiration at the cantilever terminus. This enabling technology would allow for precise cellular manipulation, perfusion, injection and imaging, as well as contractile, compressive, adhesive and thrust force measurement. Furthermore, the physical grasping nature of the probe eliminates unintended receptor-ligand associated stimulus responses, while enabling rapid and reversible serial measurement on multiple cells.

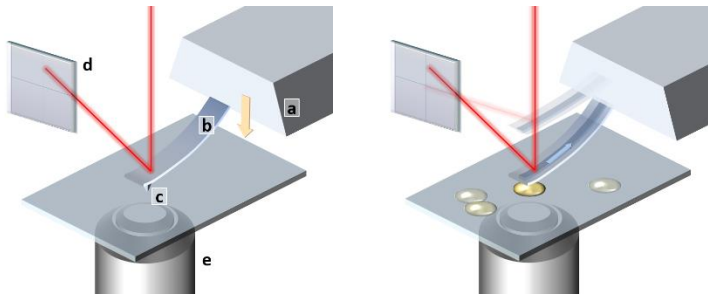


Figure 1-4 Schematic of an AFM vs. AFP:

(left) The AFM system with the standard AFM chip (a), cantilever (b), tip (c), photodetector (d), and optical targeting with microscope objective. An aspirating force probe: Immobilization of sample by underpressure (right).

1.4 HISTORY OF ASPIRATING FORCE PROBES

In 2009, Meister et al. described a class of AFM probes with an integrated nanofluidic channel that is connected to a universal liquid delivery system for single cell applications [21]. This first AFP was developed. In 2004, Meister et al. (out of CSEM SA in Neuchâtel, Switzerland) first demonstrated a ‘nanodispenser’ with the purpose of creating droplet arrays and organizing nanoparticles onto a substrate, functioning similar to a pen [22]. The specialized probe was formed from a commercial probe that was ion beam milled to create an orifice through the SiN_x tip. Though this was an open air design, this technology was then developed further to incorporate a fluidic channel, and referred to as the micromachined fountain pen (MFP). The MFP is fabricated on a silicon wafer, by depositing SiN_x films, with a channel formed from sacrificial polycrystalline-Si. Prior to etching away the sacrificial poly-Si, a Pyrex wafer is bonded on top which eventually becomes the die on which the cantilever is mounted. This allowed for transport of a continuous but limited supply of fluid from a reservoir in the die. This was promoted as a nanolithography tool, capable of both localized chemical etching and

electrochemical deposition in this highly controlled manner [23]. The use of this technology in biological applications began to emerge in 2007. Burg et al. reported, for the first time, the weighing of biomolecules and single cells using resonant frequency shifts associated with changes in mass of a cantilever probe [18]. Their original design consisted of a micro-channel which runs the length of the cantilever and then back to the chip in a loop manner. This allowed for flow of a single cell or protein containing medium to be introduced through the channel. As molecules adhere to the device wall, their cumulative mass can be measured by detecting frequency shift of the cantilever due to the additional mass. The fabrication technique remained fundamentally the same, but without either a tip or fluid aperture at the terminus. Meister's "FluidFM", in 2009, reported an improved method to microinject into subcellular domains of cells. This introduced a spatially accurate and gentle method for injecting macromolecules and transgenes into stem/progenitor cells without lethally damaging them [21], a primary challenge in subcellular injection [24]. This device features their original SiNx hollowed cantilever with a 250 nm diameter FIB milled fluidic aperture at the apex of a pyramidal tip. It should be noted that the ability to chemically stimulate cells by intracellular injection and perfusion was already possible with the microscope-micropipette system [25]; however, it was difficult to discriminate tip penetration, frequently resulting in lethally damaged cells. The benefit of the FluidFM was twofold: first, the AFM tip could gently image cells with higher resolution, revealing subcellular domains and subsequently enabling localized delivery of stimulant; second, the AFM's force sensitivity provided gentle approach and reversible penetration of the cell's membrane without significant damage to the cell. For the next few years, work expanding on the capabilities of this device continued to come out of ETH Zurich, with the demonstration of spatial manipulation cells by aspiration [26] and, more recently, the

application of measuring cell adhesion forces [27]. Enabled by the reversible aspiration nature of the AFP's, cellular manipulation and assays could now be performed rapidly, in series, abiotically and in an isotonic medium, which is more physiologically relevant. Furthermore, the ease of which these experiments were carried out is vastly improved, compared with competing assays [8], [11], [20].

1.5 LIMITATIONS IN ASPIRATING FORCE PROBE SENSITIVITY AND INTEGRATION WITH EXISTING AFM'S

Existing AFP's are stymied by high cantilever stiffness as a result of the large area moment of inertia associated with the incorporation of the additional channel forming layer, Table 3.

Table 3 Probe Sensitivity

Method	Spring Constant (pN/nm)
Bioapplications	Soft < 50 Hard > 500
Commercial Probes (Bruker MSCT)	20
Dorig <i>et al</i> (2010)	3,000
Potthoff <i>et al</i> (2012)	1,900 – 2,700
Objective of this thesis	100 or less

Furthermore, these devices control fluid flow by way of an external pressure system [21]. The interface between the fluidic pressure system and the probe currently requires destructive and irreversible modification to the AFM's costly probe mounting assembly. The probes are therefore incompatible with all AFM systems. A custom holder then requires that the functionality of the highly capable probe holders is given up entirely.

1.6 OVERALL RESEARCH CONTRIBUTIONS

In this work, numerical and fabrication methods were developed to address limitations in microfabrication techniques used in AFP construction, which can be summarized as

- Formation of the first high resolution (1.87 pN noise floor), low stiffness ($k = 53.54$ pN/nm) nano-channel cantilever. The demonstrated approach leverages the capabilities of thermally decomposable polymer to form longer channels with smaller cross sectional areas. Numerical and FEA models were developed for a channeled micro cantilever. The numerical model was used to perform a parametric analysis that would identify the key parameters contributing to the markedly stiff probes described in the literature. A low stiffness hollow cantilever was realized by reducing the top layer thickness and the channel dimensions. To achieve this, a thermally decomposable polymer was used as the sacrificial layer. A major challenge with this technique is that the overcoat layer must be deposited using a low temperature process. The PECVD nitride overcoat can be deposited at temperatures as low as 100 C. However, the film quality is poor, having residual stresses as high as 157.22 MPa. This is contrasted with the high quality film of the base layer, deposited using a low stress LPCVD method, which has a residual stress less than 100 MPa compressive and can be tailored to have tensile stress. The thermal mismatch of these materials induces a bending radius and tip deflections on the order of 100's of microns. It was hypothesized that the net residual stress of the composite material cantilever can be reduced by setting the residual stress of

each film to have complementary polarity, for example a tensile base layer and compressive overcoat. However, we find that this approach is not sufficient, as the interfacial stress is sufficient to cause stress fracturing at the features. It is shown numerically that a layer's weight or contribution to the bending moment could be enhanced by increasing its thickness. By this logic, the base layer with its lower residual stress could be made to dominate. However, this approach increases the cantilever thickness to the third power according to the model. The third approach is to perform an anneal, provided the high temperatures required for this step are conducive with the overall process flow. It has been shown that annealing at temperatures as low as 800 C will densify the PECVD nitride [28], thus decreasing its residual stress. Here, a 900 C anneal was performed, altering the overall process to allow for high temperature processing. A low stress hollowed cantilever is realized. Stiffness's of three different cantilever lengths were measured and shown to align with the numerical model.

- To integrate the cantilever into an AFM system and control pressure at the cantilever terminus, two key fabrication challenges needed to be overcome. The first was how to connect the 305 μm diameter glass capillary from the pressure control system directly into the die of the probe. This allows the probe to be used on any brand AFM, without destructive modification to the probe holder or the need to give up the complex capabilities of current holders on the market. An original side entry technique is demonstrated. The second challenge is how to connect the surface based nanofluidic channel to the subsurface microfluidic

channel. For this, two original fabrication methods are demonstrated. The key distinction between the two processes comes down to fabrication ease and repeatability versus fabrication throughput. The oxide etch-stop approach is more attractive in terms of fabrication as it is far more repeatable and forgiving, which is more optimal for non-industry based cleanrooms more variability of process control and cases where throughput is not of primary concern. The second method employs a set of entirely wafer level processing techniques for higher throughput. This technology demonstrates potential for other lab-on-chip microstructures for which channel cross sectional area is to be leveraged for testing at high shear rates and laminar flow conditions coupled with sensor systems in both aqueous and nonaqueous environments. Future work will focus on the integration of microfluidic networks in a complete sensor microsystem. As surface properties are a major concern, the characterization and the control of physicochemical properties of silicon nitride channels will also be considered.

- A liquid cell is developed that integrates a microfluidic channel around a cantilever for atomic force microscopy in aqueous environment. The device is used to record force-distance curves as well as to obtain high resolution contact mode images—both critical demonstrations of AFM capability. The volume encapsulated by the fluid cell is below 50nL and we believe further reduction in liquid volume can be achieved. This design succinctly combines batch-fabricated microcantilevers with batch-fabricated microfluidic channels.

1.7 THESIS OUTLINE

An overall description of these contributions follow. A flowchart, Figure 1-5, illustrates the development of the methods and techniques developed in this work.

In Chapter 2, design and fabrication of a low stiffness nanochanneled cantilever is described. This work addresses the primary challenge of current microchanneled cantilever technologies, and introduces the use of a thermally decomposable polymer as the enabling technology for a reduced stiffness design. A numerical model is first developed to identify the critical geometric parameters for design. The decomposition temperature of the sacrificial material necessitates the use of a low temperature top coat layer, PECVD nitride. Experimental measurement of the film's internal stress and of the bending radius of a composite cantilever, indicate residual stress from film deposition as a new design parameter, unique to this method, which must be mitigated. Film process parameters and numerical models are refined to minimize the internal stress of the cantilever, whilst achieving a low stiffness cantilever.

In Chapter 3, two original batch microfabrication process developed to connect a bulk microfluidic channel to a surface nanofluidic channel for a wide variety of microfluidic and lab-on-chip applications. The approach relies on a two-step lithography process using a thermally decomposable polynorbornene resist, Unity, to form the sacrificial channel layer,. A high aspect ratio silicon via is deep reactive ion etched to the subsurface microchannel. Lithography of a high viscosity Unity plug is followed by lithography of a low viscosity Unity sacrificial layer to form the nanofluidic channel. A plasma enhanced chemical vapor deposition (PECVD) nitride layer is deposited to encapsulate the nanochannel and the sacrificial polymer is decomposed by baking. This technique enables fabrication of complete;

off-chip to nanochannel fluidic systems; we emphasize the benefit of sacrificial polymers to form long, 3D nanofluidic channels.

In Chapter 4, design and fabrication of a microfluidic liquid cell capable of high-resolution atomic force microscope (AFM) imaging and force spectroscopy is described. The liquid cell was assembled from three molded poly(dimethylsiloxane) (PDMS) pieces and integrated with commercially purchased probes. The AFM probe was embedded within the assembly such that the cantilever and tip protrude into the microfluidic channel. This channel is defined by the PDMS assembly on the top, a PDMS gasket on all four sides, and the sample substrate on the bottom, forming a liquid-tight seal. Our design features a low volume fluidic channel on the order of 50nL, which is a reduction of over 3-5 orders of magnitude compared to several commercial liquid cells. This device facilitates testing at high shear rates and laminar flow conditions coupled with full AFM functionality in microfluidic aqueous environments, including execution of both force displacement curves and high resolution imaging.

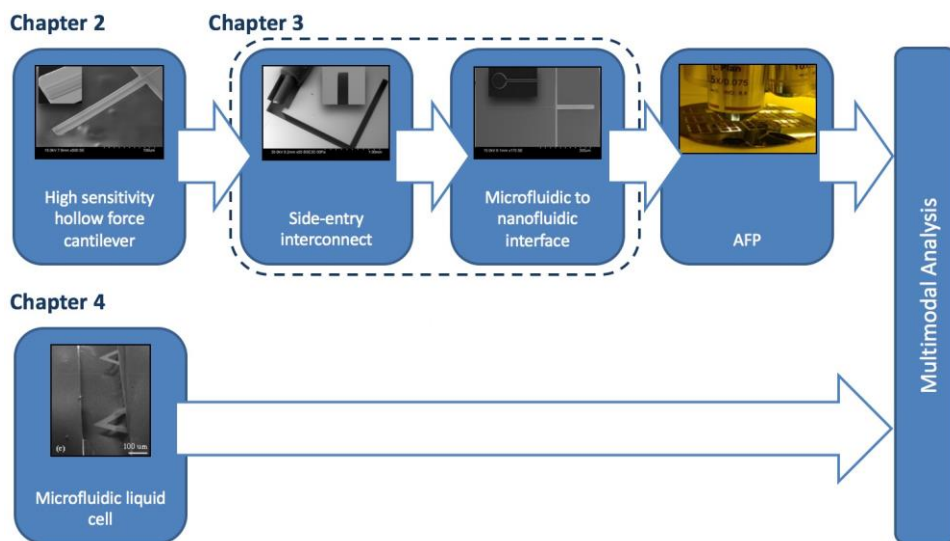


Figure 1-5 The Overall Thesis Flowchart

CHAPTER 2 HIGH SENSITIVITY COMPOSITE MATERIAL FORCE PROBE WITH NANOFUIDIC CHANNEL

2.1 OBJECTIVE

The objective of this work is to design and fabricate a low stiffness nanochanneled cantilever. This work addresses the primary challenge of current microchanneled cantilever technologies, and introduces the use of a thermally decomposable polymer as the enabling technology for a reduced moment of inertia design. A numerical stiffness model is first developed to identify the critical geometric parameters for design. The decomposition temperature of the sacrificial material necessitates the use of a low temperature top coat layer, PECVD nitride. Experimental measurement of the film's internal stress and of the bending radius of a composite cantilever, indicate residual stress from film deposition as a new design parameter, unique to this method, which must be mitigated. Film process parameters and numerical models are refined to minimize the internal stress of the cantilever, whilst achieving a low stiffness cantilever.

2.2 FUNDAMENTALS OF AFM PROBE FORCE SENSITIVITY

In performing force spectroscopy, the force sensitivity is a function of the particular specimen's indentation, d , throughout the experiment as well as the applied probe force, F . The optimal cantilever stiffness corresponds to a specimen indentation, d , to cantilever deformation, δ , ratio of one, given by $\zeta = d/\delta \approx 1$. Hence, a 1 nm deflection would correspond to 1 nm indentation. Likewise, to minimize the error in force measurement, and

given the direct proportionality of the two displacements, the optimum is a 1 to 1 relationship. This is likewise the case for the stiffness $\frac{d}{\delta} = \frac{k_c}{k_s} \approx 1$, for which the cantilever stiffness k_c is proportionate to the specimen stiffness, k_s , Figure 2-1. The sensitivity of a probe is thus the proportion of the probe's mechanical stiffness to the samples. Therefore, a properly selected probe may be used to apply a force commensurate to a specimen's mechanical properties and achieve high sensitivity force measurement.

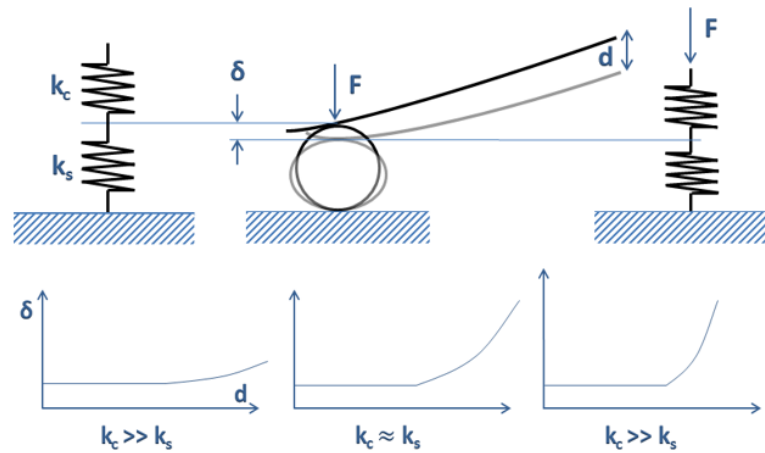


Figure 2-1 Schematic of Cell Mechanics Assay. The applied force to the specimen is chosen to lie within a range bound by a minimum force, so as to overcome vibration noise [29], [30], and a maximum force, so as to avoid irreversible deformation of the specimen [31].

2.2.1 LOWER LIMIT OF PROBE SENSITIVITY

The lower limit corresponds to the minimum force required to overcome vibration noise from the environment. For measurement of small forces, the uncertainty of the force measurement, ΔF , due to noise may be large relative to the measured force signal, given by the 'signal-to-noise ratio' $\rho = \frac{F}{\Delta f}$. Since, cantilever stiffness, k , is related to the force by Hooke's law $F = k\delta$, the force uncertainty is related to the displacement uncertainty, Δd , by $\Delta f = k \Delta d$.

$$(Eq. 1) \quad k_c = \frac{\Delta f}{\Delta d} = \frac{F}{\rho(\Delta d)}$$

Displacement uncertainty due to thermal fluctuation in a free cantilever is estimated by [32]

$$(Eq. 2) \quad \Delta d = \sqrt{\frac{k_B T}{k}}$$

In contact mode, however, the tip is engaged with a non-zero probe force. The fluctuation is reduced to a single direction, away from the constraining sample. Assuming no adhesion, which can be achieved in solution, deflection uncertainty is thus [33]

$$(Eq. 3) \quad \Delta d = \frac{k_B T}{2F}$$

Intuitively, this can be understood by the potential energy diagram Figure 2-2.

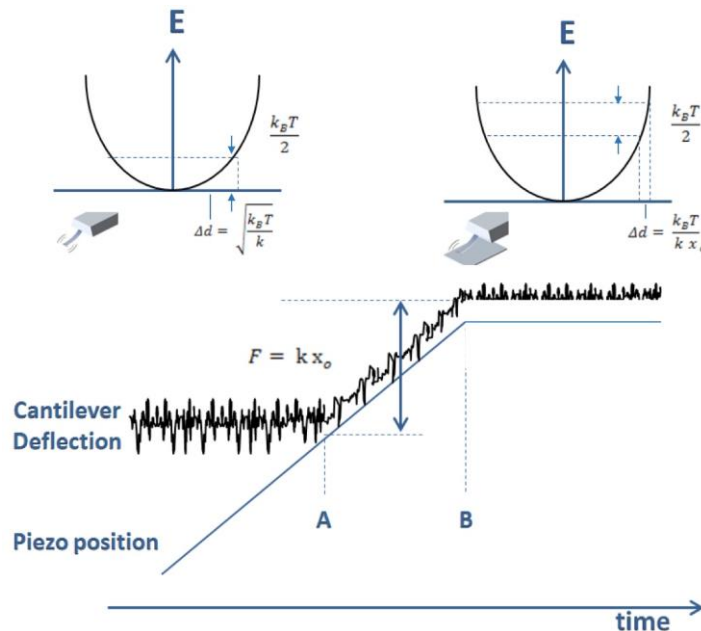


Figure 2-2 Illustration of Thermal Fluctuation Noise Amplitude: Fluctuation in terms of potential energy as a cantilever is brought into contact with the specimen.

For a particular force spec assay, the minimum spring stiffness is thus according to (Eq. 4), by substituting (Eq. 1) into (Eq. 3) to obtain:

$$(Eq. 4) \quad k_{min} = \frac{2(F_{max})^2}{k_B T \rho_{min}},$$

where the Boltzmann's constant $k_b = 1.38E - 23$ J/K.

2.3 IMPORTANCE OF CANTILEVER STIFFNESS

For compressive assays, the spring constant of a cell specimen is related to its Young's modulus according to Hertzian Model for contact mechanics [34] $k_{optimal} = \frac{4}{3}E^* \sqrt{R^* a}$, where

$$E^* = \left(\frac{1-v_1^2}{2E_1} + \frac{1-v_2^2}{2E_2} \right)^{-1}, \quad R^* = \left(\frac{1}{R_1} + \frac{1}{R_2} \right)^{-1} \text{ and } a = \left(\frac{3}{4} F \frac{R^*}{E^*} \right)^{1/3}.$$

A probe designed to target applications involving forces on the order of 100 pN, having a signal-to-noise ratio of at least 5 would require a cantilever with stiffness of at least 49 pN/nm. The optimal spring constant would be roughly 22 pN/nm [35]. Existing hollow cantilever designs, however, are stymied by high cantilever stiffness as a result of the large area moment of inertia associated with the incorporation of an additional channel forming layer, Table 3.

2.4 PARAMETRIC ANALYSIS OF CANTILEVER STIFFNESS

For parametric design of a low stiffness- high resolution channeled cantilever, a numerical model is required. Development of the composite model of a channeled cantilever begins with the basic stiffness model of a single side clamped rectangular cantilever.

2.4.1 EULER-BERNOULLI BEAM THEORY FOR A RECTANGULAR CANTILEVER

The Euler-Bernoulli beam theory reveals the parameters determining beam stiffness. Cantilever stiffness, k , given by

$$(Eq. 5) \quad k = \frac{3EI}{l^3},$$

where E is the Young's modulus, I is the area moment of inertia, and l is the cantilever length. Substituting the area moment of inertia of rectangular cantilever according to Euler-Bernoulli beam theory gives

$$(Eq. 6) \quad k = \frac{Ewt^3}{4l^3}$$

While the standard cantilever stiffness scales with the thickness to the third power, the width to the first power and inversely with the length to the third power. It may be concluded that beam thickness and length contribute to the stiffness more than width or the material modulus. Furthermore, thickness and length play complementary roles. Thus, soft cantilevers are typically realized by increasing cantilever length, reducing thickness or fabricating with softer materials.

2.4.2 NUMERICAL MODEL FOR PARAMETRIC ANALYSIS VIA BEAM THEORY FOR A HOLLOWED CANTILEVER

Applying this same logic to a hollowed cantilever, the stiffness model of (Eq. 5) may be adapted to account for the parameters of the additional device layer. That is, the area moment of inertia is now a function of both films rather than the one. Figure 2-3 illustrates the channeled cantilever and identifies the parameters contributing to the bending moment.

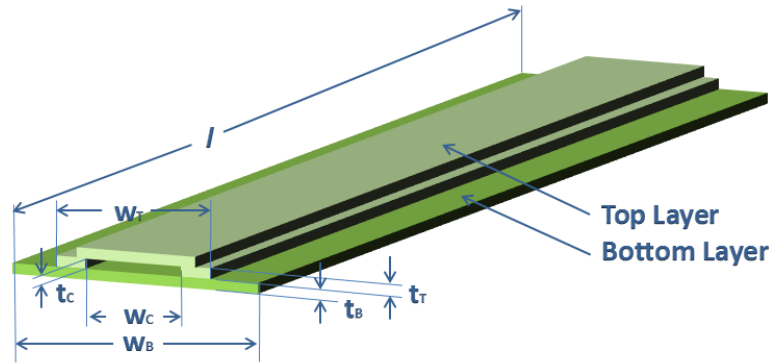


Figure 2-3 Cartoon of Hollowed Cantilever: The bottom layer (dark green) is denoted with the subscript “B”. The top layer (light green) is denoted with the subscript “T”, The channel dimensions are denoted with the subscript “C” and the cantilever length is “l”.

The numerical analysis begins by first identifying this inertial component for a generic cantilever with top and bottom device layers having widths denoted as w_t and w_b and thicknesses denoted t_t and t_b . The channel dimensions are denoted w_c , and t_c . Euler–Bernoulli beam theory is then used to determine where bending occurs about the x-axis, $I_x = \iint_A y^2 dA$. Since the cross section is complex, a composite analysis was performed on sections according

to Figure 2-4. Here, component 1 makes up the bottom layer, and components 2 through 4 approximate the top layer.

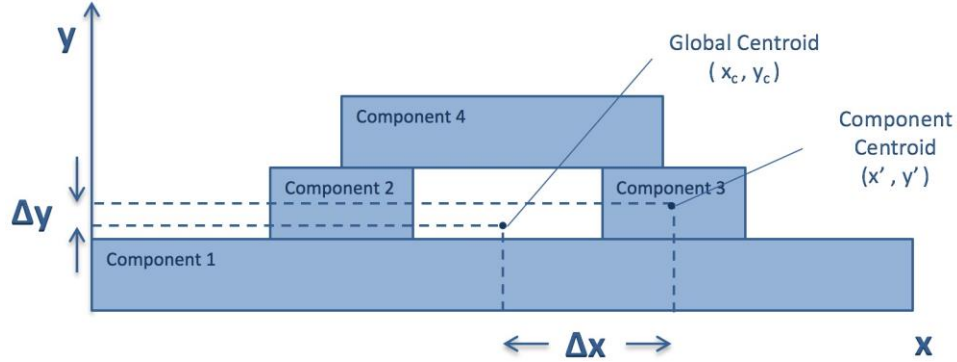


Figure 2-4 Inertial Component Partitions for Euler-Bernoulli Analysis

The sum of the individual inertias are determined relative to the global centroid $(x_c, y_c) = \frac{\sum x'_i A_i}{\sum A_i}$ by the parallel axis theorem $I_{C,i,x} = I_{P,i,x} + A_i(\Delta y)^2$ and summed $I_C = \sum I_{C,i} = I_{C,1} + I_{C,2} + I_{C,3} + I_{C,4}$. The result is

$$\begin{aligned}
 (Eq. 7) \quad I = & (t_B^4 w_B^2 + 8t_B^3 t_T^2 w_B + 4t_B^3 t_T w_B w_T + 12t_B^2 t_T^3 w_B + \\
 & 24t_B^2 t_T^2 t_C w_B + 4t_B t_T^3 w_B w_T + \\
 & 12t_B^2 t_T t_C w_B w_C + 8t_B t_T^4 w_B + \\
 & 24t_B t_T^3 t_C w_B + 4t_B t_T^3 w_B w_T + \\
 & 24t_B t_T^2 t_C^2 w_B + 12t_B t_T^2 t_C w_B w_C + 4t_T^6 + \\
 & 4t_T^5 w_T + t_T^4 w_T^2 + 24t_T^3 t_C^2 w_T - \\
 & 24t_T^3 t_C^2 w_u + 12t_T^2 t_C^2 w_T w_C - \\
 & 12t_T^2 t_C^2 w_C^2) / [12(2t_T^2 + w_T t_T + t_B w_B)].
 \end{aligned}$$

2.5 ANALYTICAL MODEL FOR VERIFICATION

The model was then validated with $n=3$ test cases, Figure 2-5, in a 3D FEA model using COMSOL. Each of the three FEA models have a matching fixed base and point force load at the cantilever end. The first test case is a typical rectangular cantilever, the second, a hollowed cantilever, and the third is a hollowed cantilever with reduced width top layer.

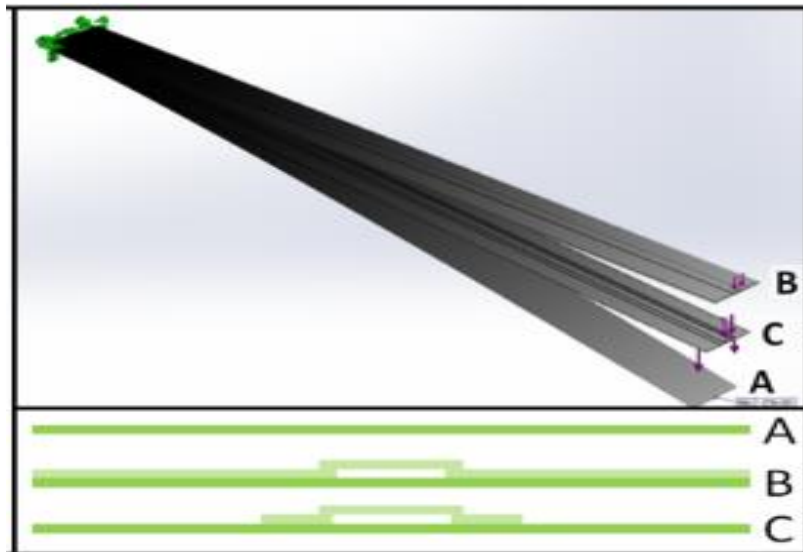


Figure 2-5 COMSOL FEA Validation of Hollowed Cantilever Model: For three test cases, an FEA model was developed. (a) A typical rectangular cantilever, (b) a hollowed cantilever, and (c) a hollowed cantilever with reduced width top layer.

The model mesh was incrementally decreased until a max of 3% mesh convergence. A quantitative agreement was realized to 3 significant digits in stiffness (N/m) between the numerical and FEA models.

2.5.1 PARAMETRIC EVALUATION OF NUMERICAL MODEL

Following the logic of Section 2.4.1, the parameters within the beam stiffness equation of (Eq. 7) can be substituted into (Eq. 5), and the parameters extracted and sorted according to their order relative to the denominator, Table 4.

Table 4 Parametric Contributions to Cantilever Stiffness

Contribution Rank	Parameter	Order
1	t_T	4 th
2	l^* & t_B	3 rd
3	t_C & w_C	2 nd
4	E, w_B, w_T	1 st

*It is noted that the length l resides in the denominator

The top layer thickness, t_T , plays the most significant role with l and t_B again representing a 3rd order contribution as with the rectangular cantilever. It can be concluded that the thickness of the top layer alone may significantly reduce the cantilever stiffness. As each of these parameters are not isolated to their own terms and also their signs vary, a better understanding of their combined effect is attained by graphing the bending moment as in Figure 2-6. The blue line illustrates the bending moment for a rectangular cantilever with no channel as the thickness is varied. Parameters for a commercial off the shelf (COTS) product (Bruker MSCT) was entered into the model; this is indicated by the blue diamond. A red zone bound by red lines represents the range that may be achieved for a hollow cantilever fabricated via traditional methods. Parameters for previously described probes were entered into the model according to Potthoff et al (2012).

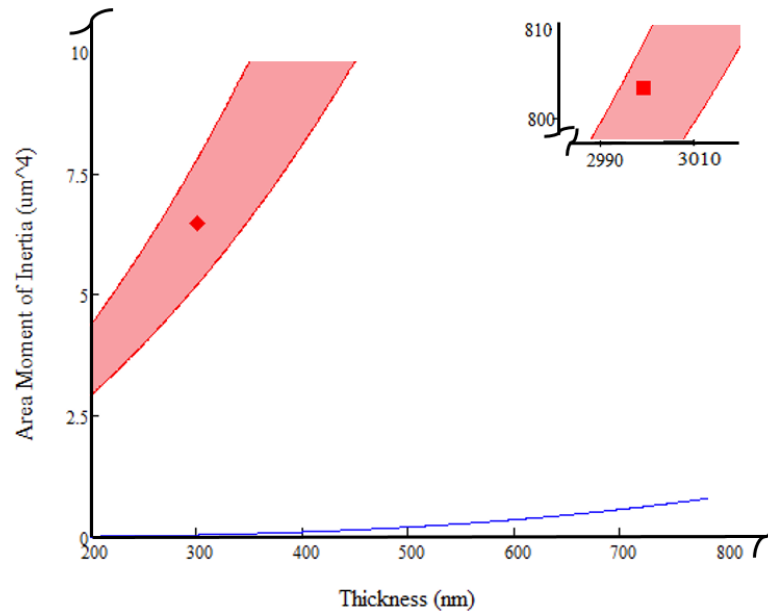


Figure 2-6 Area Moment of Inertia (μm^4): A function of base layer thickness (blue) Rectangular cantilever, (blue diamond) Bruker MSCT rectangular probe, (red zone) range for hollow cantilevers fabricated via traditional methods, (red diamond) Potthoff *et al* (2012),

The bending moment of the hollowed cantilever are 31.07 times that of the commercial rectangular probe. Optimization of the design via a parametric analysis may allow a reduction of bending moment from that published in literature to a value closer to the commercial products for this application.

2.5.2 PARAMETRIC DESIGN FOR LOW STIFFNESS HOLLOWED CANTILEVER

Decreasing the top coat thickness of the cantilever is the most effective approach to softening the cantilever, according to Table 4. At about 150 nm thickness, however, mechanical properties of Si_xN_x begin to diverge from that of the bulk properties sharply [36]. Fabricating cantilevers near this range would result in very large and unpredictable variations in cantilever stiffness within the batch, as a result of non-uniform deposition patterns. Therefore, the

practical lower limit for this parameter is 300 nm. To accommodate for the additional bending stiffness, the probe length may be increased by Δl according to (Eq. 8).

$$(Eq. 8) \quad (l + \Delta l)^3 = 31.07 \cdot l^3$$

Giving a new total length of $l' = \sqrt[3]{31.07} \cdot (l)$. A 150 μm probe such as described by Potthoff *et al* (2012) would thus need to be scaled to 471.2 μm long to counteract the increased stiffness to that of a probe without a channel.

Increasing the length would be an attractive technique; however, the system becomes less sensitive to displacement as the cantilever is lengthened [37]–[39]. An increased channel length also exacerbates the challenges in etching the sacrificial channel. Furthermore, the effects of thermal drift associated with the difference in thermal expansion coefficients between the metallization layer and the dielectric cantilever are intensified in response to gradient and time variant temperatures [40].

The cantilever thickness is the second most significant parameter. Again, the thickness is limited by the mechanical properties. Figure 2-7 illustrates the progressive effect of reducing the individual parameters. It can be seen that reducing the channel height alone, significantly reduces the bending moment, downward from 1 μm to 650 nm, Figure 2-7a, and then to 300 nm, Figure 2-7b. Further refinement is made by drawing in the width of the channel down to 2 μm , Figure 2-7c, and finally to a lower limit with the top layer width at 8 μm . It should be noted that even smaller cross sectional areas may be achieved using e-beam lithography [41]. The orange diamond of Figure 2-7 indicates the selected values for these studies, with consideration given to the capabilities and quality control of the available lithographic and film deposition equipment. These values are outlined in 0.

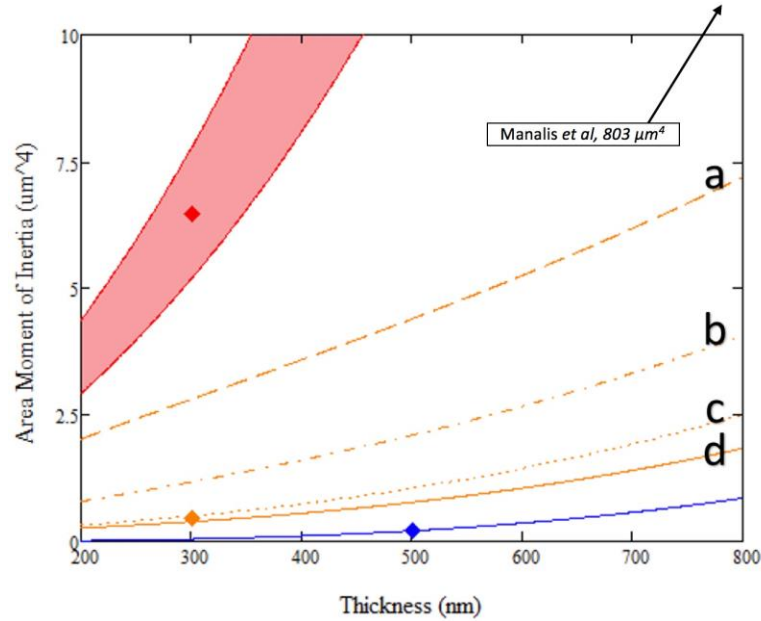


Figure 2-7 Area Moment of Inertia (μm^4): A function of base layer thickness: (blue) Rectangular cantilever, (blue diamond) Bruker MSCT rectangular probe, (red zone) range for hollow cantilevers fabricated via traditional methods, (red diamond) Potthoff *et al* (2012), (a) top layer thickness at $650 \mu\text{m}$, (b) top layer thickness at $300 \mu\text{m}$, (c) narrowing of channel down to $2 \mu\text{m}$ (d) narrowing of top layer to $8 \mu\text{m}$, (orange diamond) a feasible target bending moment for this work.

Decreasing the cantilever width is a semi-effective way of decreasing stiffness; however, it must be greater than or equal to the laser diameter to avoid noise from the portions of light that spill over and reflect off the substrate or specimen and onto the photo sensing diode. The lower limit is thus approximately $20 \mu\text{m}$.

The solution to reducing cantilever stiffness is therefore realized through a combination of parametric optimizations. Within the numerical model, we find that a low stiffness probe is theoretically feasible by reduction of the probe's bending moment, Table 5.

Table 5 Bending Moment Comparison

	w_B (μm)	t_B (nm)	w_C (μm)	t_C (nm)	w_T (μm)	t_T (nm)	I (μm^4)	Relative to COTS
COTS (Bruker MSCT)	20	550	n/a	n/a	n/a	n/a	0.208	1X
Dorig <i>et al</i> (2010)	25	300	24.4	1	24.4	300	0.917	31X
Objective	20	300	3	300	8	300	6.47	2X

The cantilever stiffness by (Eq. 5) is calculated to be 22 pN/nm for a 320 μm long probe, which is on par with that of the commercial off the shelf (COTS) probs.

2.6 TECHNIQUES IN MICRO AND NANOCANNEL FABRICATION

Microchannels are commonly fabricated by soft lithography, or the casting of elastomers, thermoplastics, hydrogels and thermosets, and offers good fabrication ease at low cost. Patterned paper and caramel have even been used [42], [43]. However, the incorporation of microfluidics into silicon based MEMS devices has opened a world of opportunities through integration with other MEMS technologies, such as electro-mechanical sensors and actuators. These microchannels are formed by bulk micromachining into silicon and silica substrates. In comparison with other soft lithography techniques, these materials offer better resistance to organic solvents and oxidizers, greater ease in metal deposition, higher thermal conductivity, more stable electroosmotic mobility, higher mechanical strength, higher aspect ratio geometry, higher geometric resolution and constraint, higher temperature resilience, lower permeability, lower absorption of hydrophobic molecules, a stable surface charge, the ability to adsorb biomolecules and a smaller overall device size.

More recently, MEMS fabrication has afforded nanoliter channels to be formed and has enabled biomolecular sensing of single-molecules [18], [45] and separation of DNA [46]. An excellent review of fabrication techniques for probes specifically is given by Ghatkesar *et al*, [47]. A variety of methods of forming nanofluidic channels has been demonstrated [48], including etching and bonding [41], [45], integration of carbon nanotubes [49] and performing a series of oxidation and reactive ion etches [50]. A general review of nano-scale fluidic channel fabrication techniques is given by Xie *et al*, 2013. Three primary techniques are described including nanowire/nanotube, nanoparticle crystal, nanoporous materials, ion selective polymers. However, these approaches are costly and complicated, [48].

A attractive new method of creating nanofluidic channels is by lithographic patterning of a thermally decomposable polynorbornene sacrificial polymer, followed by PECVD nitride deposition and polymer decomposition [41]. The unique decomposition and diffusion mechanism of this material [51], [52] enables the formation of long channels and 3D structures, not producible with traditional sacrificial materials (SC-Si, poly-Si and silica) due to mass transport limitations with regard to reactant delivery and product extraction. Furthermore, the flexibility of pattern design with e-beam or UV lithography, and the ability to form the channels without harmful etching agents is particularly attractive for creating devices for bioapplications in which surface chemistry is extremely delicate.

2.7 SACRIFICIAL THERMALLY DECOMPOSABLE POLYMER APPROACH

Unity is a thermally decomposable photopolymer developed at Georgia Tech by the Paul Kohl lab and currently supplied by Promerus® LLC. At an elevated temperature, referred to as the

decomposition temperature, the resist decomposes into gas molecules and free radicals small enough to permeate one or more of diffusing through one or more embodiment materials such as the PECVD silicon nitride overcoat layer [53], [54]. This property offers many opportunities in lab-on-chip applications, especially as a sacrificial layer for microfluidic channels. Though heat is the choice energy used within these studies, it should be noted that other forms of energy may be used including UV radiation and optical energy [54]. The traditional method of forming microfluidic channels by chemical etching of a sacrificial material (i.e. oxide) is a well-established technique. However, the process requires sufficient delivery of reactant and product chemicals to and from the etch interface, thus rendering the method challenging and even impossible for channels with high length to cross sectional area ratios (Figure 2-8). Furthermore, chemical etchants for dielectrics do not have perfect selectivity; this means that for highly controllable and uniform channel cross sections, Unity sacrificial layers offers superior advantages in channel microfabrication.

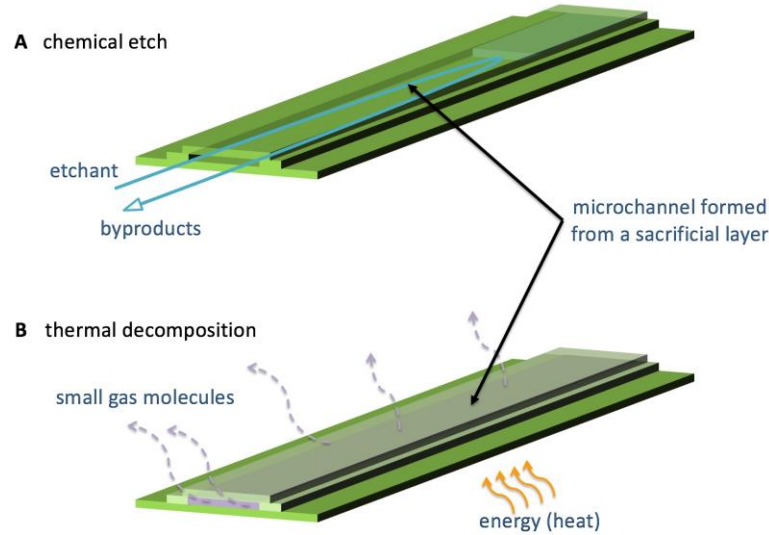


Figure 2-8 Comparison of Sacrificial Layer Methods for Nanofluidic Channels: (a) Silicon based sacrificial layer (such SC-Si, poly-Si and silica) cannot be used to form long narrow channels because of limited delivery of reactant and product chemicals to and from the etch interface. (b) Polynorbornene sacrificial layers hypothetically allow for infinite channel length because the small gas byproducts (acetone and CO₂) can permeate through one or more dielectric channel layers in a thermal decomposition process that does not compromise the channel film quality. Overcoat layers are made semi-transparent to show removal mechanism within.

2.7.1 CHALLENGES IN POLYMER BASED SACRIFICIAL CHANNELS

The caveat of the resist is its low decomposition temperature, as it limits all channel overcoat temperatures. There are both high and low temperature versions of norbornene based Unity products [55]. High temperature Unity decomposes at roughly 400 °C; however, the glass transition temperature is roughly 250 °C (fully cured). This is not suitable for high temperature deposition methods such as LPCVD and thermal oxide which have process temperatures typically above 830 °C. PECVD oxide and nitride may be processed temperatures between 100 °C and 400 °C. Pin holes and poor RI qualities are realized below 300 °C. At a temperature above the glass transition temperature, decomposition begins when a thermally

generated acid (H^+) is activated, breakdown of polymer begins, leaving the byproducts acetone and CO_2 to diffuse through the overcoat layer (Figure 3-1).

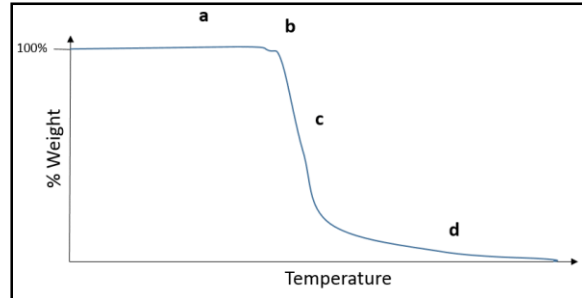


Figure 2-9 Illustration of Thermogravimetric Analysis of Unity Decomposition as a Function of Temperature: (a) glass transition temperature, (b) thermally activated acid is generated, (c) polymer breakdown by acid, (d) complete decomposition of polymer.

The illustrative thermogravimetric analysis is a recreation of a similar figure for low temperature Unity [53]. Two considerations must be taken when selecting the decomposition temperature: first, a low decomposition temperature for which acid is generated, but at a low rate, will result in a residue within the channel that can negatively affect the flow; second, a high decomposition temperature for which acid is generated quickly, will result in a high rate of byproduct that can burst the over coat film if the rate of generation is faster than it can permeate through the film and orifices [55]. With this in mind, the exact ramp rate and dwell temperature that is used is highly dependent on the volume of the Unity forming the channel as well as the thickness and type of overcoat layer. Experimentation must be performed for each case to determine the appropriate processing conditions.

2.8 DESIGN AND FABRICATION

2.8.1 CHIP ARCHITECTURE

The chip level architecture is illustrated in Figure 2-10. The characteristic rectangular AFM probe has been substituted with a 4 mm by 4 mm chip to allow for a glass capillary interconnect to be installed; further detail on this will be described in a later chapter. The cantilever is 20 μ m wide, and three variants probe lengths were employed to account for radial variation in device layer uniformity across a 4" wafer. A key note is that a vertical 'well', connecting the microfluidic channel to the nano-fluidic channel, requires that the interface be set back from the edge of the chip, a result of KOH wet etch release of the chips, and the 54.7 degree plane that results. As such, the total length of the microfluidic channel is increased by 200 μ m or more, unless a Bosch etch release method is used.

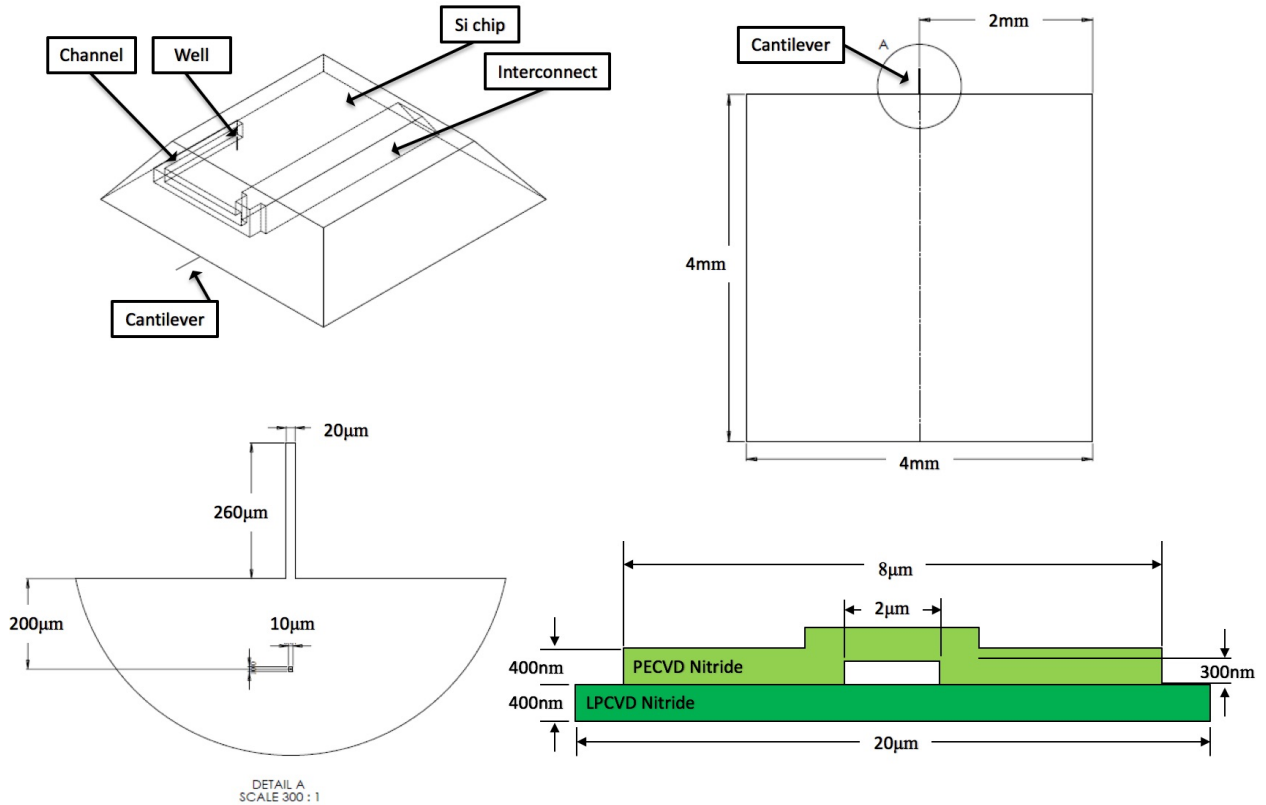


Figure 2-10 Layout of Cantilever and Chip Architecture: Orthographic view of silicon chip with respective top down view of chip dimensions and section detail of composite nitride cantilever. Detailed dimensions are given in Appendix B and Appendix C

2.8.2 FABRICATION PROCESS

The fabrication process was carried in the cleanroom facilities at the Institute for Electronics and Nanotechnology (IEN) at Georgia institute of Technology. The structure was fabricated on a single crystal silicon wafer (500 µm thick, prime grade, DSP, < 1 0 0 >), Figure 2-11. Using a Tystar nitride furnace, one micron thermal oxide mask layer is grown. The 400nm low stress LPCVD nitride device layer is grown ($\text{NH}_3/\text{SiH}_4 = 0.5$, 750 °C) using a Tystar nitride furnace [56]. Lithography and plasma etch is performed on both the top and the bottom of the bonded wafers forming the cantilevers on the top and the cantilever release pattern on the bottom, using a Karl Suss MA6 TSA mask aligner and an Oxford HRM plasma etcher. A low

viscosity Unity® 4678E (4 cP):Toluene mixture (10:1) was spun on using a Karl Suss SB8 spinner, and allowed 5 min for incursion into the well, followed by selective photopolymerization. The surface is then oxygen plasma cleaned (Oxford Endpoint RIE: 300 mTorr, 300 W, 100 sccm O₂, 100 sccm Ar, 30 s) and a second, thinner Unity® 4678E (2 cP) layer is patterned, forming the fluidic channel. The 300nm PECVD nitride device layer is thermally grown (Oxford ICP PECVD). The Unity sacrificial layer is then thermally decomposed (Lindberg Furnace), followed by a gold reflective layer on the top surface (Denton Explorer). A chrome adhesion layer was employed.

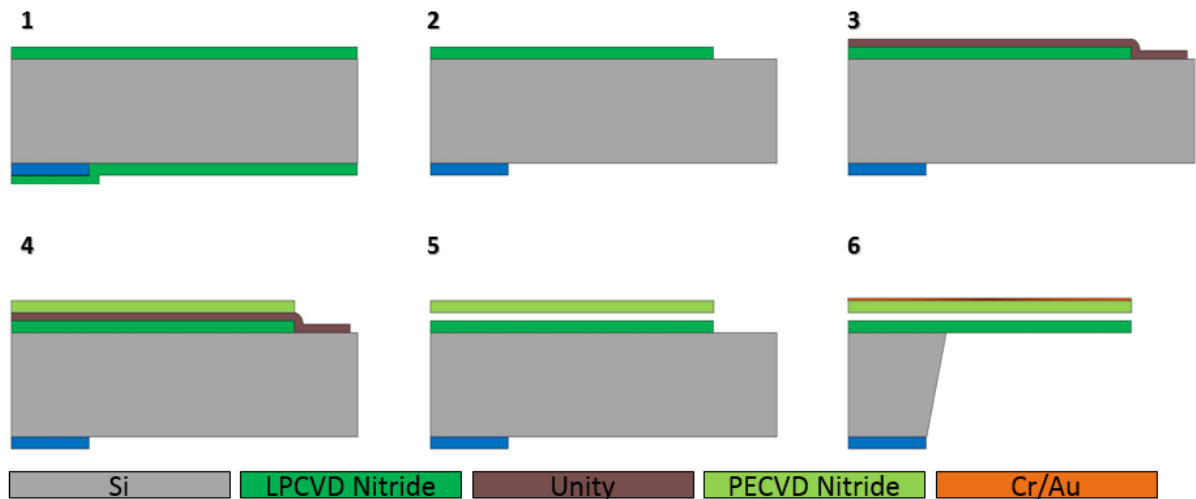


Figure 2-11 Low Stiffness Cantilever Fabrication Process

The process chemistry, equipment and physical parameters are specified in Table 6.

Table 6 Layer processing parameters

	Silicon Substrate		Oxide & Nitride		Oxide & Nitride	
Tool	STS ICP		Oxford Endpoint RIE	Vision RIE 3	Plasma Therm ICP	Lindburg Furnace 4
Process	Silicon Etch		Anisotropic Dielectric Etch	Nitride Etch	Dielectric Etch	Unity Decomposition & Nitride Anneal
Pressure (mTorr)	0.1		33	40	5	--
He Leakup (mTorr)	< 20		--	--	--	--
Dwell Time (s)	Etch = 10s	Pass = 7s	--	--	--	*
Temperature (C)	--	--	--	--	--	--
Chemistry 1, Rate (sccm)	C4F8, 0	C4F8, 100	Ar, 25	CHF3, 45	Ar, 5	N, 4k
Chemistry 2, Rate (sccm)	SF6, 130	SF6, 0	CHF3, 25	O2, 5	C4F8, 15	--
Chemistry 3, Rate (sccm)	O2, 13	O2, 0	--	--	CO2, 28	--
RF (W)	11	0	200	250	40	--
ICP (W)	600	600	--	--	800	--
Magnet (A)	2	0	--	--	--	--
	Thermal Oxide		Low Stress LPCVD Nitride	PECVD Nitride	Cr	Au
Tool	Tystar Mini 1 Furnace		Tystar LPCVD Nitride Furnace	Oxford ICP PECVD	Denton Explorer E-Beam	Denton Explorer E-Beam
Process	Oxide Deposition		Nitride Deposition	Nitride Deposition	Au Deposition	Cr Deposition
Pressure (mTorr)	atm		158	10	10 ⁻⁷	10 ⁻⁷
He Leakup (mTorr)	--		--	--	--	--
Dwell Time (s)	--		--	--	--	--
Temperature (C)	1100		830	200	--	--
Chemistry 1, Rate (sccm)	DI Bubbler, ~100		DCS, 100	SiH4, 14.5	Cr	Au
Chemistry 2, Rate (sccm)	--		NH3, 17.XX (SP=20) **	N2 Blend, 12	--	--
Chemistry 3, Rate (sccm)	--		--	--	--	--
RF (W)	--		--	1	--	--
ICP (W)	--		--	550	--	--
Rate (Å/s)	--		--	--	1	1

* Unity decomposition and anneal recipe: RT to 250 °C @ 2 °C/min, 250 °C to 440 °C @ 1 °C/min, dwell 3hr, 440 °C to 1000 °C @ 2 °C/min, dwell 2hr, 1kC to 250 °C @ 2 °C/min, 250 °C to RT @ 5 °C/min,

**The Sub-unity significant digits are unknown due to monitor malfunction (SP = set point)

2.9 RESULTS AND DISCUSSION

Following chip release by KOH etchant, it was observed that probes exhibited a bending radius causing cantilever deflections at the tip of as much as 150 μm . Additional trials revealed also the occurrence of tensile, and fracturing Figure 2-12.

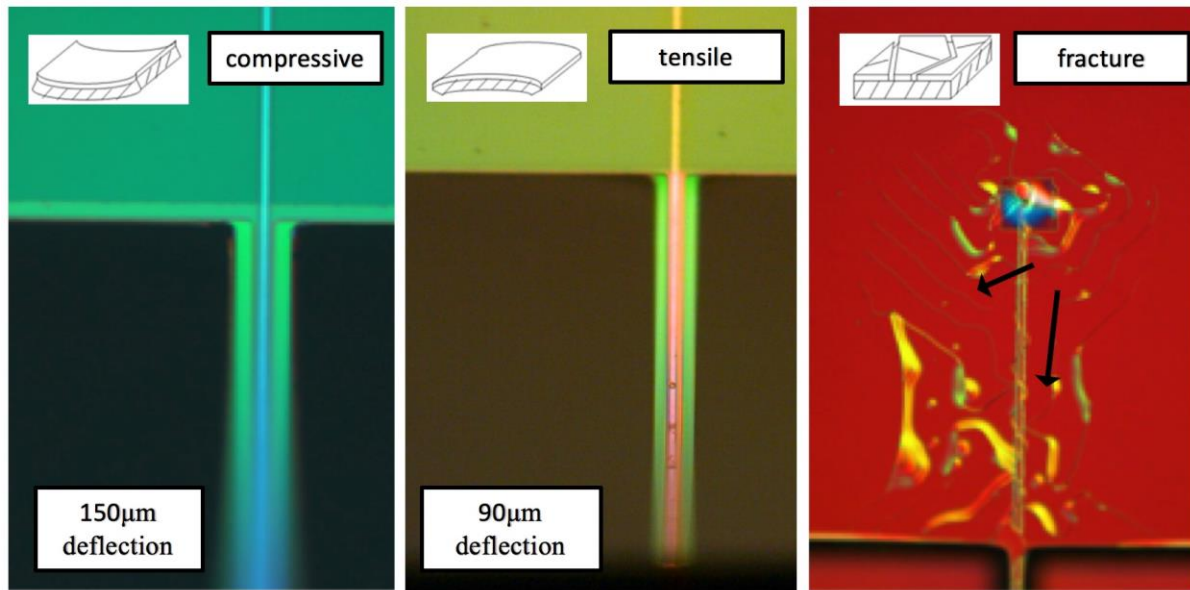


Figure 2-12 Bending Radii Exhibited in Cantilevers from Residual Stress of the Composite Architecture

It was hypothesized that the residual stress of the composite architecture was culpable. In one case, the degree to which the cantilevers deflected varied concentrically and even alternated from compressive, for chips at the wafer center, to tensile, closer to the wafer edge. This finding was compared with the film thicknesses previously recorded for the sample, Figure 2-13, obtained using a Woollam M2000 Ellipsometer. The PECVD nitride thickness profile on the left indicates the within-wafer non-uniformity (WIWNU) for this sample. This exhibits a thickness variation range of more than 40 nm, which is roughly 13% of the device layer thickness of 300 nm. This correlation indicated not only that the film's residual stress

contributed to the severe bending, but also that such a thin device layer could be significantly impacted by moderate variations in film thickness uniformity.

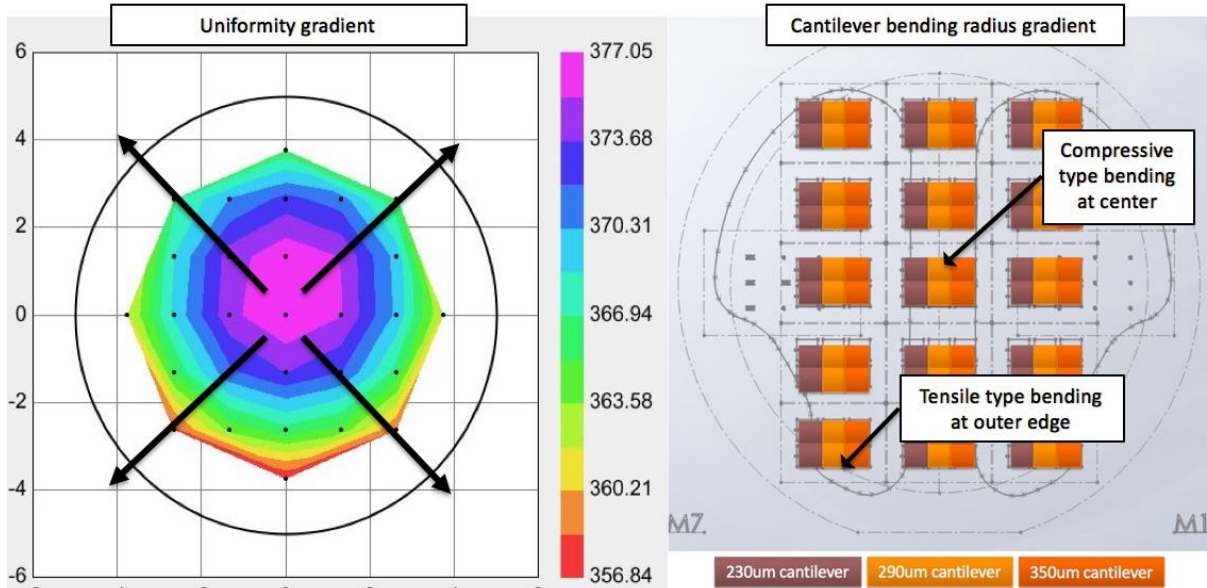


Figure 2-13 PECVD Nitride Thickness Profile (left) vs. Cantilever Bending due to Residual Stress (right)

To eliminate the possibility that the bending phenomenon was a result of thickness variation on the device level (from cantilever base to tip), individual probes were checked for film thickness variation via profilometer Figure 2-14 (right).

To evaluate whether or not the bending phenomenon was a result of thickness variation on the device level (for example thickness variation from base to tip due to loading effects during any etching processes) single layer probes were fabricated from both PECVD and LPCVD nitride films separately as in Figure 2-14. No significant thickness gradient across the length of the

cantilever could be observed. This supports that the undesirable bending observed is dependent on the deposition technique rather than defects caused by etching.

Two separate Si wafers were subsequently coated with nitride films. The first was coated with LPCVD nitride and its stress measured using a BowOptic stress analyzer, Table 7 specimen 3. When a cantilever is patterned and released, we observe that the low residual stress corresponds to a very low deflection Figure 2-14 (left). The second wafer was coated with PECVD nitride at 100 C and its stress was also measured and recorded, Table 7 specimen 4. Here we see that the elevated stress levels associated with PECVD deposition correspond with excessive beam bending, Figure 2-14 (right).

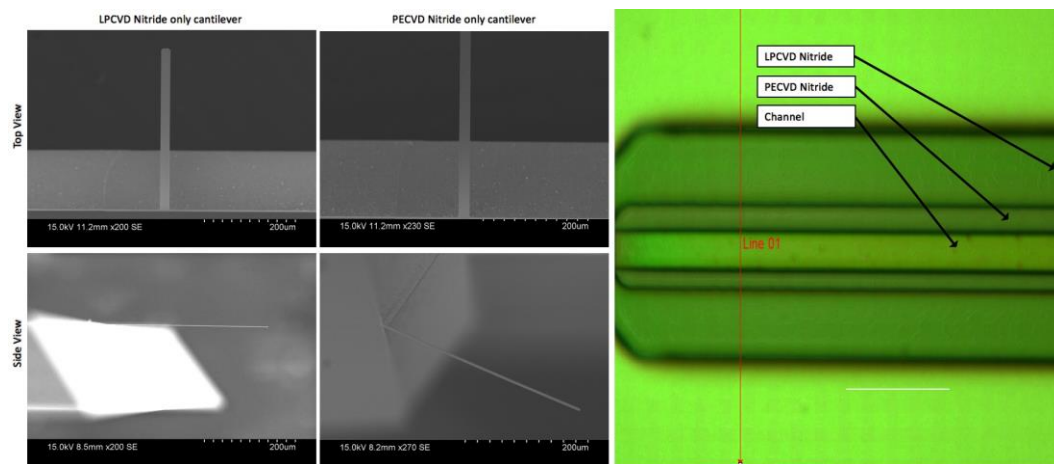


Figure 2-14 Evaluation of Contributing Factors to Cantilever Bending Radius: 300 nm thick LPCVD nitride cantilevers exhibit no initial bending radius in the non-composite architecture (left), while the 300 nm PECVD Nitride exhibits a large deflection (middle). Dektak profilometer indicates no device level thickness variation from base to tip of composite architecture cantilever (right). Scale bars are 100µm, 100µm, and 20µm from left to right.

Note that exact recipes used are referenced within the table. All together this shows that the problem would require mitigation via a thorough dissection of the film stress contributions in

the stack, and further, an understanding of the role of substrate material and processing conditions on the net stress of a cantilever made from composite materials.

2.9.1 RESIDUAL FILM STRESS INDUCED BENDING OF COMPOSITE MATERIAL CANTILEVERS

The cantilever developed here has a composite material architecture, consisting of an LPCVD base layer and a PECVD Nitride top layer. The bending moment described is a result of the thermal mismatch between the two materials. Although both layers are nitride, the low temperature PECVD process will give pin holes and higher hydrogen densities within the film, which creates slightly different coefficients of thermal expansion, but more critically, atomic mismatch at the interface of the two layers. Ion bombardment also induces significant film stress with this method; however, densification can be achieved through annealing, where nitrogen and hydrogen atoms are made to diffuse out and grain boundaries expand.

A low-stress LPCVD nitride recipe in which the gas ratio of dichlorosilane (DCS) to ammonia (NH₃) is 6:1, can be used to fabricate a cantilever with residual stresses less than (+) 100 MPa (tensile) resulting in a mostly straight cantilever. The low temperature (PECVD at 200 °C) nitride that must be deposited on atop, however, typically has higher compressive residual stresses upwards of -200 MPa. These thermal mismatch values are with respect to the silicon substrate, they can only elude to the deflection that would occur by stacking them together.

2.9.2 MITIGATION OF RESIDUAL STRESS FOR A CANTILEVER OF A COMPOSITE MATERIAL ARCHITECTURE

Excessive cantilever bending can thus be mitigated with appropriate selection of deposition parameters and post processing to reduce the thermal mismatch between a film and the substrate to which it is formed. Literature on the matter has indicated that a thin film should have a residual stress of < 100 MPa to have good mechanical properties [57]. The residual stress within a film is a function of the processing conditions, and also the substrate to which the layer is deposited on. When building structures comprised of stacked composite films, the combined effect may be good or bad depending on the combined effect of the layers. Since the LPCVD deposition recipe can be customized to achieve both tensile and compressive values through slight changes in the gas ratios, it is possible cater the net residual stress (and thus beam deflection) by first determining the range of film stresses that may be tolerated according to a model of composite structures [58].

2.9.3 DETERMINING THE MEAN AND GRADIENT STRESS IN THIN FILMS

The stress model for thin films accounts for the total stress which is the sum of the cumulative effect of all uniaxial mean film stresses (σ_0) from thermal and extrinsic stresses; and intrinsic stresses (σ_1) from non-uniformity through the thickness of the layer during deposition (deposition rate, deposition temperature, pressure in the deposition chamber, incorporation of impurities during growth, grain structure, fabrication process defects). Note, however, that stress relief following cantilever release from the Si substrate can come from not only change in curvature but by change in length.

(Eq. 9)

$$\sigma_{total} \approx \sigma_0 + \sigma_1 \left(\frac{2y}{h} \right)$$

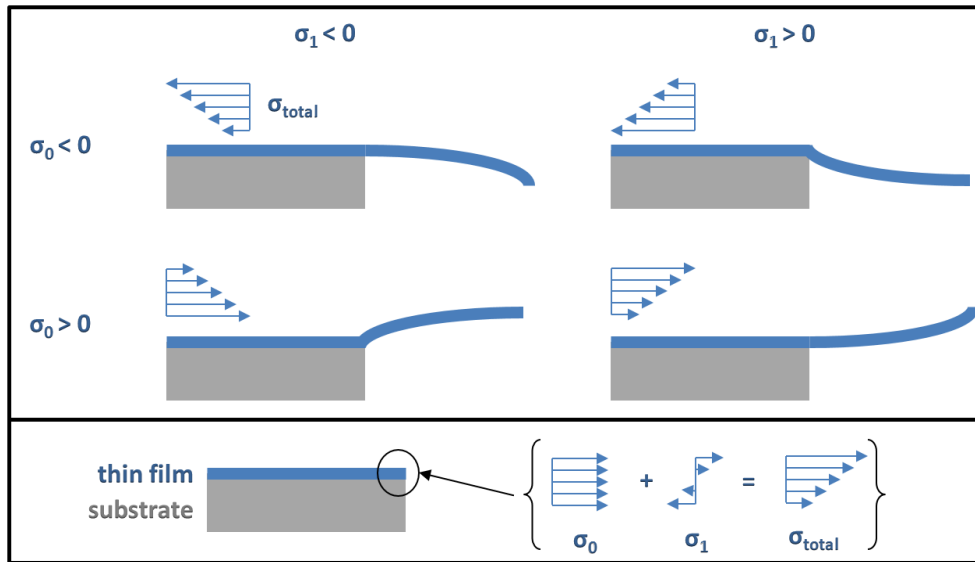


Figure 2-15 Total Film Residual Stress: (top) 4 states of thin film deflection as it depends on the total film stress which comprises (bottom) the constant mean stresses and the linear gradient stresses [58].

Considering that there is no doping involved in this process sequence, and that deposition conditions are assumed to be constant throughout the deposition process; intrinsic (gradient) stresses have therefore been ignored. The film stress (σ_f) due to thermal mismatch can then be simplified to:

$$(Eq. 10) \quad \sigma_{f,mismatch} = \frac{E_s}{(1-\nu_s)} (\alpha_f - \alpha_s) \Delta T$$

where, the subscript f refers to the film and s refers to the substrate, α is the thermal expansion coefficient, E is Young's modulus, and ν is the poisson ratio. Therefore, the design of the stack can be made considering the that the difference in thermal expansion coefficients between subsequential layers in the stack.

2.9.4 DESIGN FOR LOW NET RESIDUAL STRESS IN COMPOSITE CANTILEVERS BY
 COMPLEMENTARY STRESS POLARITY

The analysis of stress was performed using a BowOptic analyzer with which the radius of curvature of the wafers was measured before and after film deposition, Figure 2-16. Film thicknesses profiles were measured using a 29 point map of a 4” wafer to within 1cm of the wafer edge as in Figure 2-13. The Stoney equation was employed using the average film thickness across the wafer as measured using a Woollam M2000 Ellipsometer.

(Eq. 11)
$$\sigma_f = \frac{E_s d_s}{6(1-\nu_s) d_f} \left(\frac{1}{R_{post}} - \frac{1}{R_{pre}} \right)$$

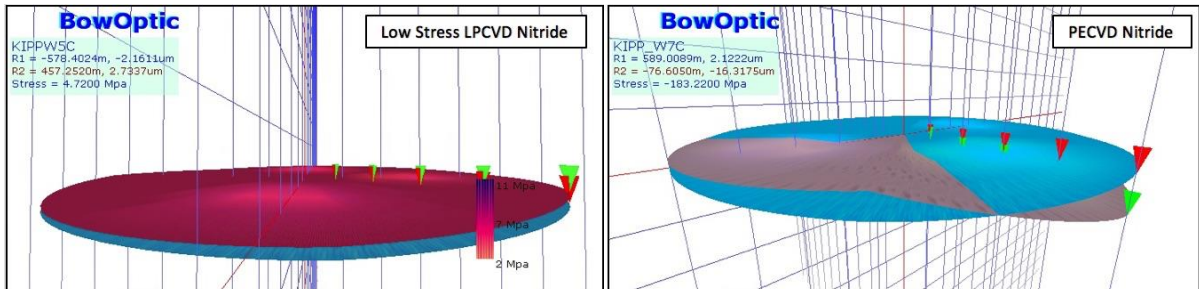


Figure 2-16 Film Residual Stress for both low stress LPCVD (left) and PECVD Nitride (right).

Stacked layers were additionally measured, Table 7, processing parameters are listed in Appendix D.

Table 7 Stress measurement according to layer***

Error! Not a valid link.* The stress values for the stacked layers indicate the combined effect of all processing conditions.

** Ratios refer to gas ratio of dichlorosilane (DCS) to ammonia (NH3)

*** Processing parameters are detailed in Appendix D.

A comparison of specimen #3 and #5, in which the films are deposited separately, with that of specimen #7, in which the film layers were stacked, illustrates that the compressive LPCVD and tensile PECVD can work to complement each other, . A side view of a released cantilever for this case illustrates this complementary effect Figure 2-17. However, we find that the solution would not be as simple as selecting equal and opposite residual stress values to obtain a net zero stress. Reducing the DCS:NH₃ ratio, in which a more compressive LPCVD is deposited, induces an interfacial stress sufficient to cause film stress fracturing at stress concentration points, specifically, the channel edges. This is exhibited in Figure 2-17 (right).

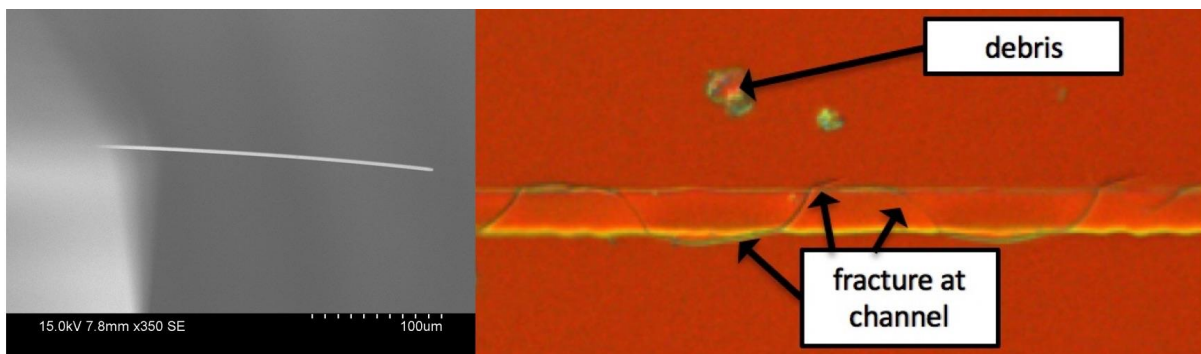


Figure 2-17 Residual Stress Induced Fracturing: (left) Device features such as the channel are stress concentration points for fracturing. (right) No interfacial stress fracturing on released cantilever.

2.9.5 DESIGN FOR LOW NET RESIDUAL STRESS IN COMPOSITE CANTILEVERS BY MINIMIZING EFFECTS OF HIGH STRESS LAYERS

The problem can be quite complex, as it depends heavily on the substrate for which these device layers are being deposited on. Furthermore, a residual stress of some level will certainly exist within a composite structure. We see that the bending radius is a function of the total bending moment of the stack

$$(Eq. 12) \quad R = \frac{EI}{M_{total}}$$

where R is the bending radius, E is the elastic modulus, I is the bending moment, and M_{total} is the sum of the bending moments of the individual layers

$$(Eq. 13) \quad M_{total} = \sum_{i=1}^n [\sigma_i \cdot (A_i \cdot d_{y_{GC}})]$$

where A_i is the cross sectional area of a film, $d_{y_{GC}}$ is the distance from the global centroid, σ_i is the films stress. The weighted value is thus

$$w = A_i \cdot d_{y_{GC}}$$

A thicker layer increases its cross sectional area and shifts the global centroid closer to its component centroid. According to this logic, the overall bending radius can be reduced by increasing the thickness of the LPCVD layer, because allowing its lower internal stress to dominate. Though an attractive solution, we find two major caveats. First, the act of thickening the film increases the probe stiffness significantly. Second, the neutral axis is shifted from the material interface, which is where the majority of the molecular restructuring takes place. The neutral axis (blue) is illustrated in Figure 2-18 for a cantilever with equal film thickness under bending load. This is a potentially significant issue when the the probe is under loading.

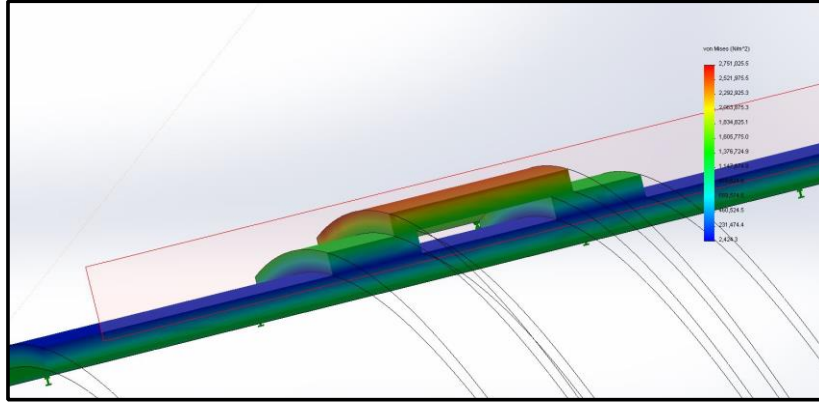


Figure 2-18 Sectional View of Solidworks Model: This illustrates the location of neutral plane for equal thickness device layers

As the figure illustrates, equal thickness layers have a neutral axis roughly at their interface. It may be concluded that increasing the thickness of LPCVD device layer can reduce the net stress by shifting the neutral axis toward its centroid; thereby allowing the thickness mismatch between the two device layers to compensate for the thermal mismatch.

2.9.6 MITIGATION OF RESIDUAL STRESS BY HIGH TEMPERATURE ANNEALING

High temperature annealing is an effective method for reducing film stress. Specimen 6 of Table 7, shows a significant reduction in film stress by performing a 900 C anneal on a PECVD film deposited at 200 C. Patterning and releasing the cantilevers shows that the 59.89 MPa film stress will result in deflections less than 10 μm , Figure 2-19a. This is a significant improvement compared with the non-densified film in Figure 2-14. Applying this technique following the LPCVD nitride deposition results in a composite material stack with a slightly better net residual stress of 48.13 MPa, Table 7.

Though an attractive solution, many processes prohibit high temperature processing due to deterioration of device layers. Furthermore, some devices contain metals, which may contaminate the annealing chamber and the device itself. Therefore, when applying this anneal technique to the gold diffusion eutectic bonded wafer stack, we see gold contamination of the device layer with re-deposited metal elements on the surface. This results in an even higher residual stress causing the cantilever to curl back on itself, Figure 2-19b. Furthermore, crystalline deposits are seeded. It was therefore necessary to modify the process flow, replacing the gold eutectic bond with a non metal bond approach. A direct Si-Si bond mechanism was chosen. More critically we find that combining the thermal decomposition and annealing process, Figure 2-20, we eliminate the opportunity for contamination. With this approach, we've shown that it is possible to fabricate a low residual stress hollow cantilever made from a composite material nitride stack, Figure 2-19c and d.

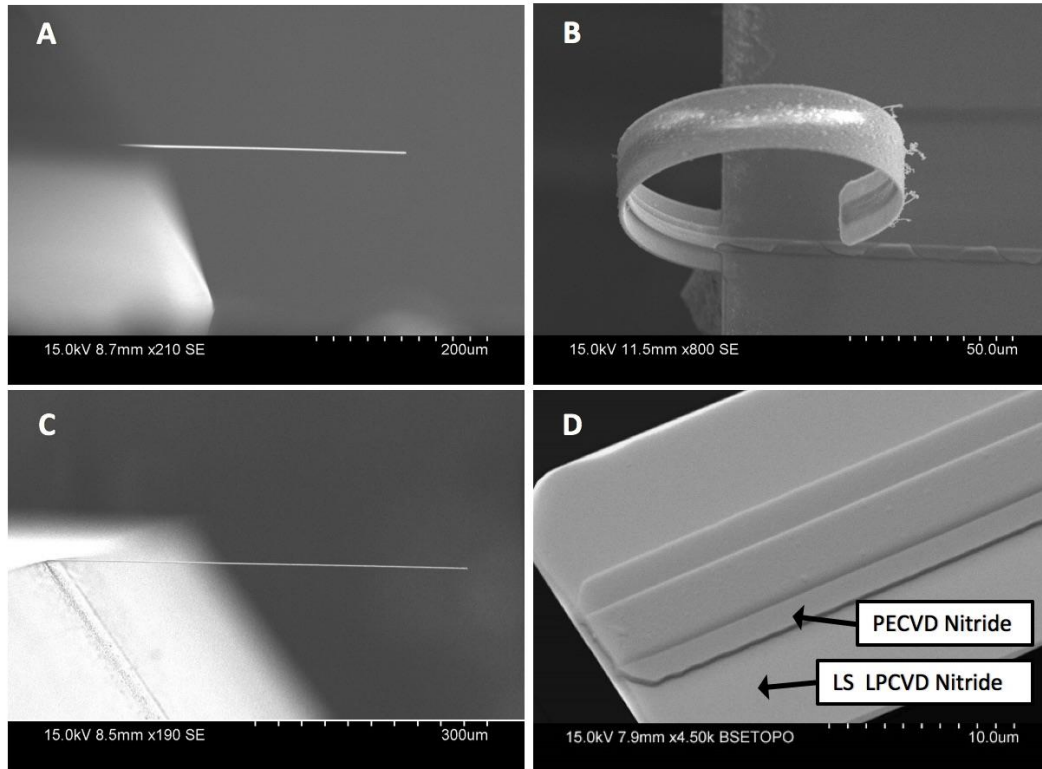


Figure 2-19 Mitigation of Residual Stress by High Temperature Anneal: (a) annealed PECVD nitride cantilever, (b) annealed composite cantilever with metal contamination, (c) annealed composite cantilever side view, and (d) annealed composite cantilever top view.

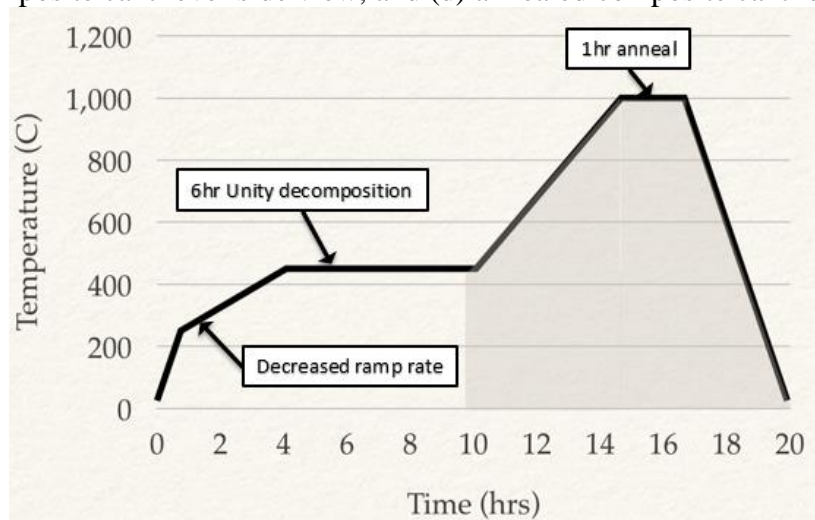


Figure 2-20 Combined Thermal Decomposition and Anneal in Series

2.9.7 WITHIN-WAFER NON-UNIFORMITY

As cantilever characteristics are highly sensitive to film thicknesses, the thin film uniformity across the wafer is of utmost importance. This section investigates this effect and proposes solutions for mitigating this variation.

Within wafer non-uniformity can result in extreme cantilever variation and even little to no yield of cantilevers with the acceptable mechanical properties. Non-uniformity in the case of PECVD is a result of gas flow dynamics at the wafer edge and is predictably limited to the outer few millimeters. In this work, uniformity is defined as

$$(Eq. 14) \quad U = \frac{d_{max} - d_{min}}{2 \times \bar{d}},$$

where d_{max} , d_{min} , and \bar{d} are the maximum, minimum and average thickness of the film over the wafer measured by a Woolam Ellipsometer for a 29 point map at 3 angles, 65,70, and 75 degrees with a 10 mm edge exclusion. Nitride films were deposited on 100 mm diameter silicon wafers precleaned by a piranha solution at 120 °C. PECVD Nitride films were deposited at 13.56 MHz, Nitrogen blend (N₂) at 12 sccm, Silane (SiH₄) at 10 sccm, RF at 1 W, ICP at 550 W, temperature of 200 °C, and pressure 10 mTorr using an Oxford ICP PECVD, having O₂ plasma cleaned the chamber for 40 min prior, followed by a 5 min season. The ICP-PECVD was chosen over PECVD because the higher density plasma leads to greater dissociation for the precursor gas for lower hydrogen content in films at moderate temperatures [59]. Although an anneal would later be performed on the film, improved step coverage may be realized early on, reducing susceptibility to cracking and at feature edges in the interim.

The model previously described for cantilever stiffness shows that a range of just 40 nm for a 400 nm thick PECVD layer (10% uniformity) can result in a stiffness variation of over 22p N/nm for a 230 μm cantilever. To obtain a reasonable yield of probes with relevant stiffness's, a uniformity of less than 3% is needed, which is the typical process performance standard [60]. To yield a high quality film with improved uniformity, *Xu et al 2013* suggest that an appropriate gas ratio will reduce surplus Si or N conditions [61].

Sequential trials were performed in which ICP-PECVD nitride films were deposited for 26 min in each trial. The nitrogen containing gas (N₂ blend) was held constant at 12 sccm, and the silane incrementally increased, Figure 2-21. This approach mimics that of *Xu et al 2013*. A nominal thickness non-uniformity is achieved at a silane flow rate of 14.5 sccm, in which the non-uniformity is a low 1.64%, Figure 2-22. While the trend mirrors that shown in Xu's work, the significantly higher variation in result found within a more moderate incremental change in silane flow rate is attributed to the higher plasma density associated with ICP-PECVD in this case. It should be noted that residual stress has been shown to have strong dependence on deposition rate at less than 10 nm/min [59].

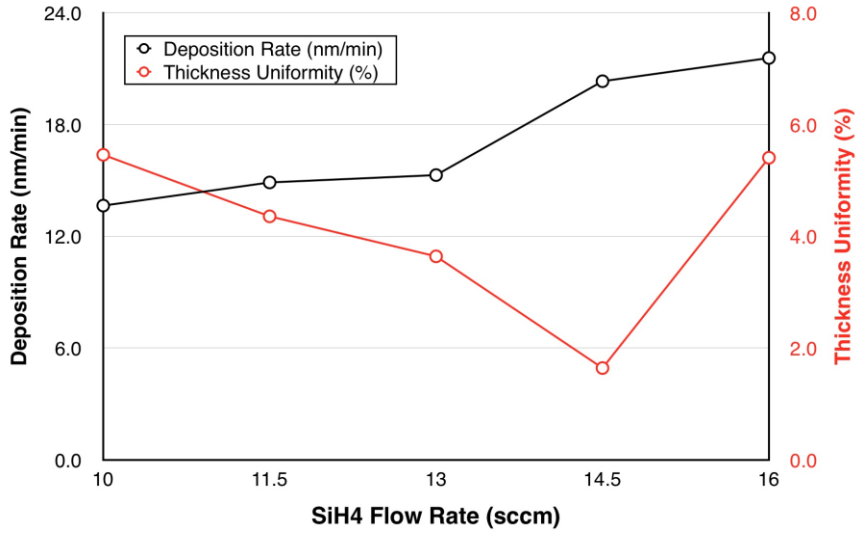


Figure 2-21 Deposition Rates and Thickness Uniformities for PECVD nitride film deposited with varying silane flow rates

Low stress LPCVD Nitride films were deposited at 830 °C, dichlorosilane (DCS) at 100 sccm, ammonia (NH₃) at 17.XX sccm, and pressure of 158 mTorr (Tystar Nitride Furnace). The thickness uniformity was measured for both films, Figure 2-20(a) and (b). Uniformity over two specimens for each film type was measured. Uniformity for both PECVD (at 5.46%) and LPCVD (at 7.57%) were well above that long accepted as the typical process performance at 5%.

The LPCVD nitride film uniformity was improved to 2.44% by placing a second and third dummy wafer upstream of the samples, Figure 2-22(b). This improves flow dynamics over the wafers to resemble that of batch processed wafers of 20 or more, thereby realizing wafer uniformity values likened to that of batch processes as well.

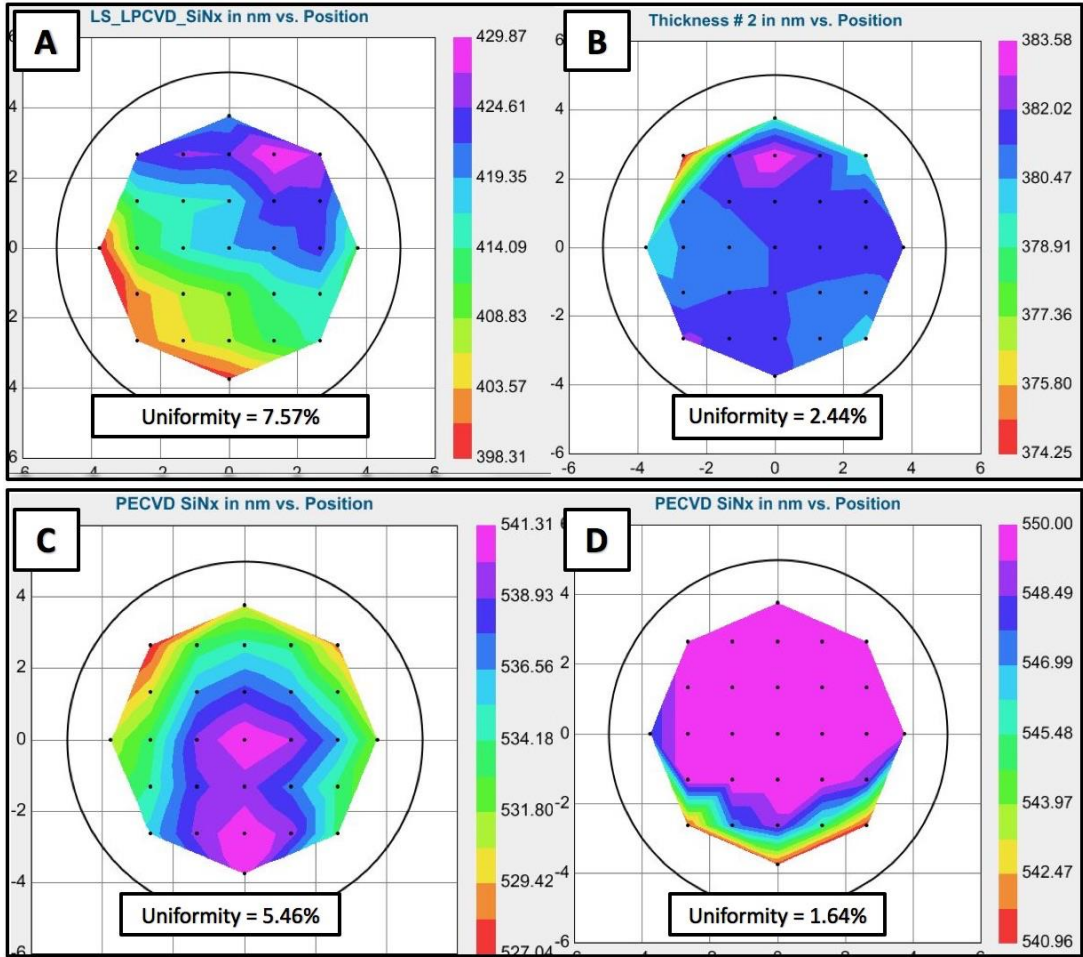


Figure 2-22 LPCVD and PECVD Nitride Film Uniformity

2.10 CHARACTERIZATION OF LOW STIFFNESS AND COMPOSITE MEMS

CANTILEVER

A set of low stiffness cantilevers with micro-channels were fabricated and the stiffness of each of three different cantilevers, varying only in length (230 μm , 290 μm , 350 μm) were determined from a force deflection curve on an Asylum MFP-3D AFM, Figure 2-23.

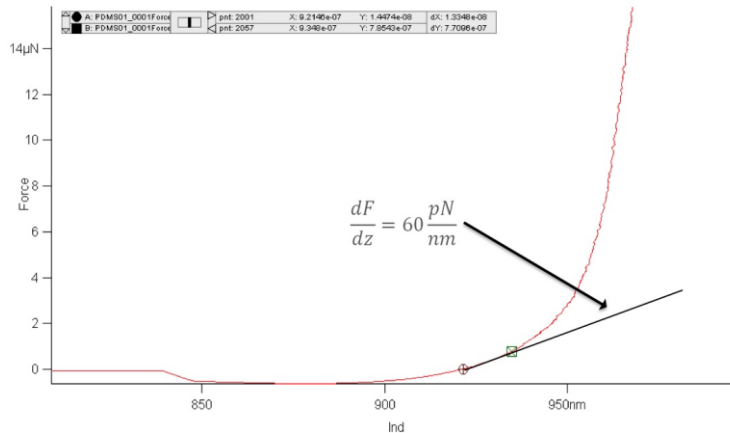


Figure 2-23 Force-deflection Curve

The measured cantilever stiffness with widths $w_B = 20 \mu\text{m}$, $w_C = 3 \mu\text{m}$, $w_T = 8 \mu\text{m}$ and thicknesses $t_B = 400 \text{ nm}$, $t_C = 300 \text{ nm}$, $t_T = 300 \text{ nm}$ are according to Table 8. Experimental results correspond with the numerical estimation, the highest relative error being 4.9%, in the case of the 230 μm long cantilever. Error is attributed to variations in the actual cantilever dimensions, considering both tolerances in fabrication technique as well as variability of material properties on the micro and nano scale, specifically the Ti/Au reflective

layer. Table 8 shows a quantitative comparison of the numerical model with the average (or nominal) empirical (or stated) results.

Table 8 Comparison of Theoretical and Actual Spring Constants

Probe	Spring Constant (pN/nm)	
	Numerical Model	Empirical
230 μm	116.24	110.53
290 μm	51.24	53.4
350 μm	32.99	33.2
Dorig <i>et al</i> (2010)	--	3,000
Potthoff <i>et al</i> (2012)	--	1,900 – 2,700

An SEM of the hollowed cantilever indicates a low deflection of less than 5 μm , Figure 2-24. A 10 nm gold conductive layer coats the probe for improved image capture resolution within the SEM (Hitachi variable pressure SEM).

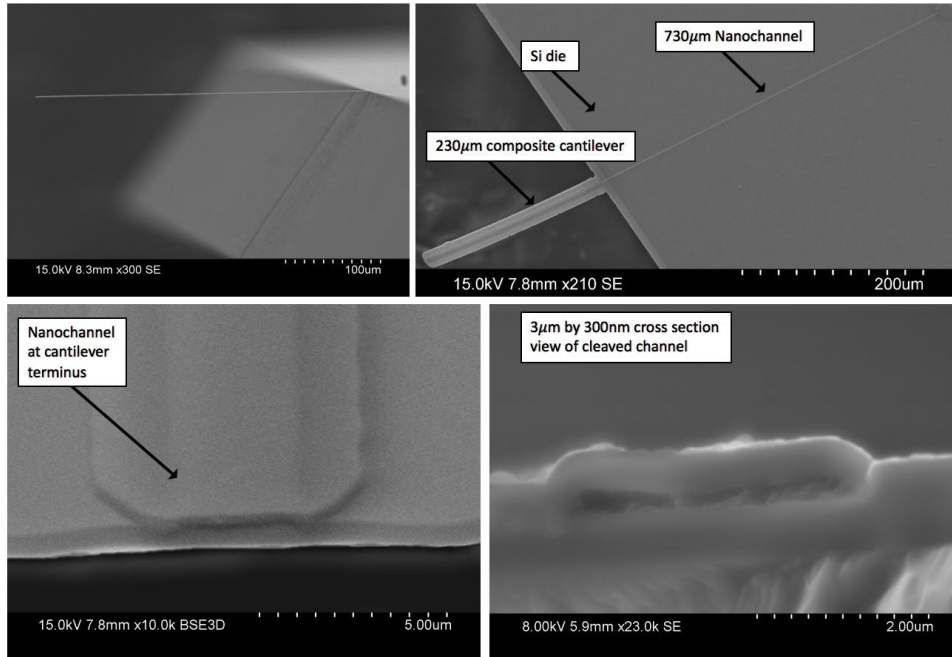


Figure 2-24 Composite Material Hollow Cantilever

2.11 CONCLUSIONS

The first high sensitivity, low stiffness nanofluidic channel is developed by leveraging the capabilities of thermally decomposable polymer to form longer channels with small cross sectional moments of inertia. Numerical and FEA models were developed for the hollow channeled microcantilever. The numerical model was used to perform a parametric analysis that would identify the key parameters contributing to the markedly stiff probes described in the literature. A low stiffness hollow cantilever could be realized by reducing the top layer thickness and the channel dimensions. To achieve this, a thermally decomposable polymer is used as the sacrificial layer. A major challenge with this technique is that the overcoat layer must be deposited using a low temperature process. The PECVD nitride overcoat can be deposited at temperatures as low as 100 °C. However, the film quality is poor, having residual stresses as high as 157.22 MPa. This is contrasted with the high quality film of the base layer,

deposited using a low stress LPCVD method, which has a residual stress less than 100 MPa compressive and can be tailored to have tensile stress. The thermal mismatch of these materials induces a bending radius and tip deflections on the order of 100's of microns. It was hypothesized that the net residual stress of the composite material cantilever can be reduced by setting the residual stress of each film to have complementary polarity, for example a tensile base layer and compressive overcoat. However, we find that this approach is not sufficient, as the interfacial stress is sufficient to cause stress fracturing at the features. It shown numerically that a layer's weight or contribution to the bending moment could be enhanced by increasing its thickness. By this logic, the base layer with its lower residual stress could be made to dominate. However, this approach increases the cantilever thickness to the third power according to the model. The third approach is to perform an anneal, provided the high temperatures required for this step are conducive with the overall process flow. It has been shown that annealing at temperatures as low as 800 °C will densify the PECVD nitride, thus decreasing its residual stress. Here, a 900 °C anneal was performed, altering the overall process to allow for high temperature processing. A low stress hollowed cantilever is realized. Stiffness's of three different cantilever lengths were measured and shown to align with the numerical model.

CHAPTER 3 MICRO- TO NANO-FLUIDIC INTERFACE VIA A THERMALLY DECOMPOSABLE SACRIFICIAL POLYMER

3.1 OBJECTIVE

The development of microfluidic technology has been mostly governed by the capacity of fabrication techniques and materials, more exactly, at the interface of macro-micro and micro-nano structures [62]. We present two original batch processes to connect a bulk microfluidic channel to a surface nanofluidic channel for a wide variety of microfluidic and lab-on-chip applications [63]. The first approach relies on a two-step lithography process using a thermally decomposable polynorbornene resist, Unity, to form the sacrificial channel layer. A high aspect ratio silicon via is deep reactive ion etched to the subsurface microchannel. Lithography of a high viscosity Unity plug is followed by lithography of a low viscosity Unity sacrificial layer to form the nanofluidic channel. A plasma enhanced chemical vapor deposition (PECVD) nitride layer is deposited to encapsulate the nanochannel and the sacrificial polymer is decomposed by baking. The second approach eliminates the need for a two-step approach by way of an oxide etch stop to span the well. While the first method offers higher fidelity well features, the aforementioned approach produces significantly higher uniformity and thus yield. Finally, a side-entry direct-to-chip capillary interconnect for analogue fluidic pressure control for fluidic characterization. These techniques enable fabrication of complete; off-chip to nanochannel fluidic systems; we emphasize the benefit of sacrificial polymers to form long, 3D nanofluidic channels.

3.2 OVERARCHING APPROACH

Two approaches were fabricated and experimentally evaluated. The first is a two-part Unity approach in which a thick (high viscosity) Unity is first applied to wafer forming a plug, then a second application of thin (low viscosity) Unity is applied to form the channel, relying on the plug to physically support it. The second approach involves the use of an oxide etch stop technique in which an oxide layer is left at the surface and allowed to support the thin (low viscosity) Unity that is applied to form the channel. The oxide is later selectively removed by wet etch.

A device requiring a side-entry gas or liquid fluidic inlet via a capillary interconnect necessarily requires a hermetically sealed bond such as Si-Si fusion, eutectic or anodic, Figure 3-1. A less hermetic seal may be achieved via epoxy based adhesion of the two chips. In either case, the compressive forces required to form the bond would crush any extruding surface channels, Figure 3-1a. As such, these surface channels must be formed after the bond steps requiring now that a plug (Figure 3-1b) is formed to span the well (Figure 3-1c) that was formed to connect the surface channel to the subsurface trench (Figure 3-1d) in which the capillary is inserted (Figure 3-1e).

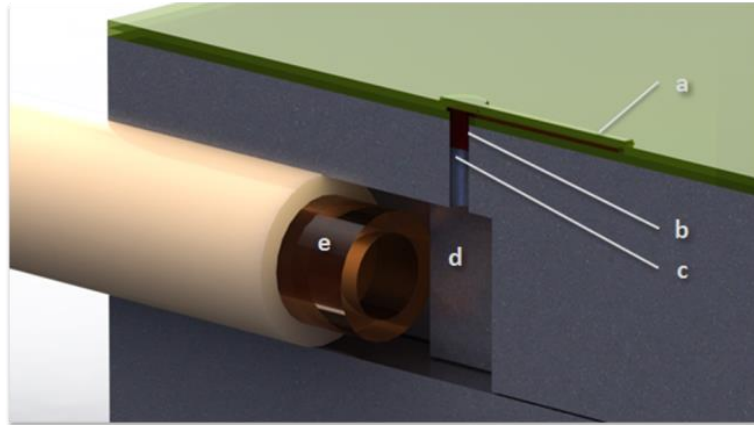


Figure 3-1 Cross Section Diagram Illustrating Micro to Nano-fluidic Interface: (a) nanofluidic channel, (b) sacrificial polymer layer, (c) connecting well, (d) bulk micromachined microfluidic channel and (e) capillary interconnect (glass capillary with polymer sleeve).

3.3 TWO PART UNITY FABRICATION METHOD

A well and trench are formed by deep reactive ion etching (DRIE) into a double side polished (DSP), $\langle 100 \rangle$ oriented silicon wafer masked with thermal oxide (SiO_2). Following oxide removal, the trench side of the wafer is then Si-Si fusion bonded to an identical Silicon wafer to form the trench by which the glass capillary will be inserted, Figure 3-2a. At this point, a silicon nitride (Si_3N_4) layer may be grown by low pressure chemical vapor deposition (LPCVD) to form a device layer, improve the hermeticity of the bond interface or protect the inside from subsequent liquid silicon etch release steps. Note that an additional and much larger well is remotely situated and serves to facilitate both the escape of expanding gases during all processes involving heating as well as enable sufficient incursion of reactant gases during nitride growth, not depicted. A thermally decomposable negative tone resist (Unity 4678E) is used to form the surface nanochannel. Since the viscosity of such resist is on the order of cP, the viscosity is likely insufficient for spanning the well, a two step process is

performed. First, a more viscous (order of 10's – 100's cP) film is spun and exposed to create the sacrificial plug, Figure 3-2b. The plug is then appropriately planarized such that the over-layer may be structurally robust Figure 3-2c. The second (lower viscosity) polymer layer is then spun and exposed to form the channel profile Figure 3-2d. The nano-fluidic channel formation is then completed by deposition and patterning of the top nitride layer, Figure 3-2e, followed by decomposition of the Unity and insertion of a PEEK sleeved glass capillary, Figure 3-2f. In lieu of a higher quality over-layer deposition methods, the nitride layer is deposited at low temperature (100°C) via plasma enhanced chemical vapor deposition (PECVD), in order to evade premature decomposition of the sacrificial layer, which occurs at sub 425°C temperatures. To reduce the PECVD induced film stress and improve pinhole density [64], an anneal is performed at 1100°C for 1 hour, directly after decomposition.

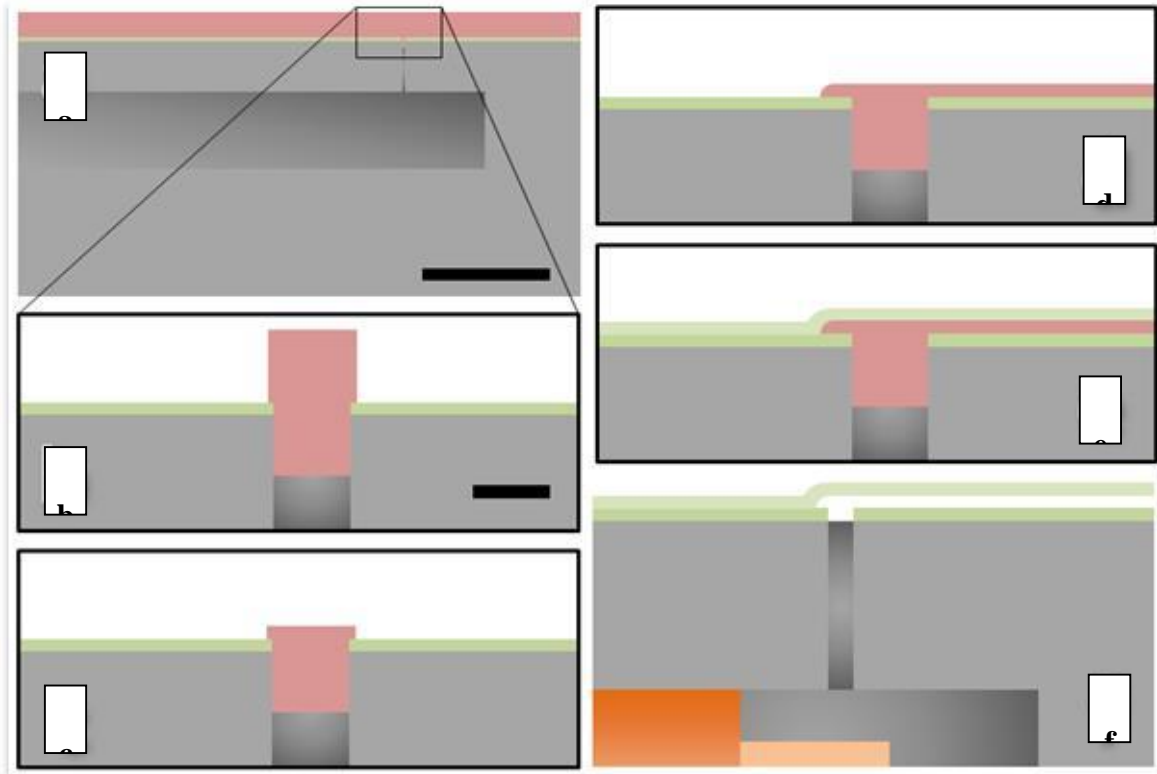


Figure 3-2 Two-Part Unity Method for Micro to Nano-Fluidic Interface: Fabrication via a thermally decomposable sacrificial polymer. (a) processed chip with bulk microfluidic features is enclosed by a bonding process and connected to the surface by a Bosch etched well. The sacrificial plug is formed by applying a thermally decomposable polymer which is made to infiltrate the well, (b) followed by selective exposure to UV radiation and (c) planarization. (d) a second, low viscosity, polymer layer is applied to form the channels, (e) followed by a low temperature PECVD nitride top coat and (f) a decomposition bake and capillary insertion, creating a continuous fluidic channel. Scale bars for (a) and (b) are 500 μm and 10 μm , respectively.

3.3.1 PLUG FORMATION

The viscosity of the resist layer is directly dependent on the ratio of its polymer (polynorbornene) and solvent (2-heptanone) concentrations, with a higher ratio of polymer to solvent equating to higher viscosity and the photoactive compound (PAC) plays a negligible role at < 1wt%. Selecting the appropriate solution and associated viscosity depends on the entire spectrum of lithography conditions. In general, solutions on the low end of the viscosity

spectrum were found to have better well infiltration and reflow characteristics as well as thicknesses closer to that of the channel thickness; however, the higher solvent concentrations meant significant shrinkage, bubble seeding at feature edges, and usually discontinuous film coverage over the well. Studies have previously characterized, and in some cases modeled, topographical resist spin coating for trenches, vias, and cavities, comparing various process, material, and geometric parameters [65], [66]. To date, no study has characterized topographical patterning of Unity resists over wells; however, key characteristics bridge resist types. If two resist solutions have the same shear viscosity, the higher concentrated one (lower molecular weight) will give a more planer film [67]. Furthermore, it was shown that increasing solvent volatility hurts planarization [67]. Commercial products designed for topographical coating, therefore, aim at reducing these effects. In this work, the topographical cavity is a wafer deep ($500\ \mu\text{m}$) deep and $10\ \mu\text{m}$ diameter well. Moreover, the well opens into a vast trench. This topography does not fit the described models having only limited depths on the order of tens of microns. The hypothesis is that by forcing a polymer rich resist into the well, a support structure could be formed while shrinkage during solvent bake-out steps could be minimized. We would first identify a method of infiltrating the cavity, then a method for planarizing the overly thick resist.

Prewetting

Prewetting of the well serves two functions and can be done using either Hexamethyldisilazane (HMDS) or a low viscosity solution of the resist that will later be formed over it. Both HMDS and low viscosity Unity are able to easily infiltrate the well. This conditions the silicon inner wall surface energy to be hydrophobic, encouraging capillary flow into the well for following

applications. HMDS in particular is designed to serve as an adhesion promotor. For each of the following approaches to infiltrating the well, prewetting with HMDS was first performed, in which HMDS is applied on a spinner at 4000 rpm and then baked at 100 °C for 1 min.

Limitations in Unity Processing

The resist profile over a well could be controlled by careful selection of resist viscosity. However, as resist viscosity is a function of solvent concentration, bake time and temperatures play a large transient role throughout the PAB, exposure, PEB, and cure steps. Furthermore, various observations, such as bubble formation, bursting, push-out and shrinkage were made that impose limits on these parameters, thus increasing the complexity of this problem. Solvent vapor bubbles were observed at feature edges. During prebake, feature edges (90deg angles in this case) act as seeding sites in which solvent vapor near vertical walls would conglomerate, forming undesirable bubbles Figure 3-3a. The likeliness of bubble formation decreased with lower solvent concentrations, suggesting bubble formation is gaseous solvent diffusion rate dependent. Therefore, a lower temperature prebake should allow gas diffusion to occur faster relative to the vaporization rate, avoiding gas accumulation; such was the case. For low viscosity resist with 2-heptanone solvent, a maximum of 85 °C would be applied on the 5 min PAB; thereafter, higher temperatures could be applied without bubble formation. Pressure buildup within the cavity will obtrude a poorly adhered plug Figure 3-3b or eject through an incompletely cured plug Figure 3-3c. The effect appears highly proportional to the cavity volume, but may be remedied by ramping bake temperatures or implementing longer, lower temperature bakes. Alternatively, the cavity may be completely filled with resist; however,

vertical shrinkage, during bake out, is exacerbated, owing to contact at the base of the cavity and balance of forces. Shrink depth appeared to be proportional to the depth Figure 3-3d.

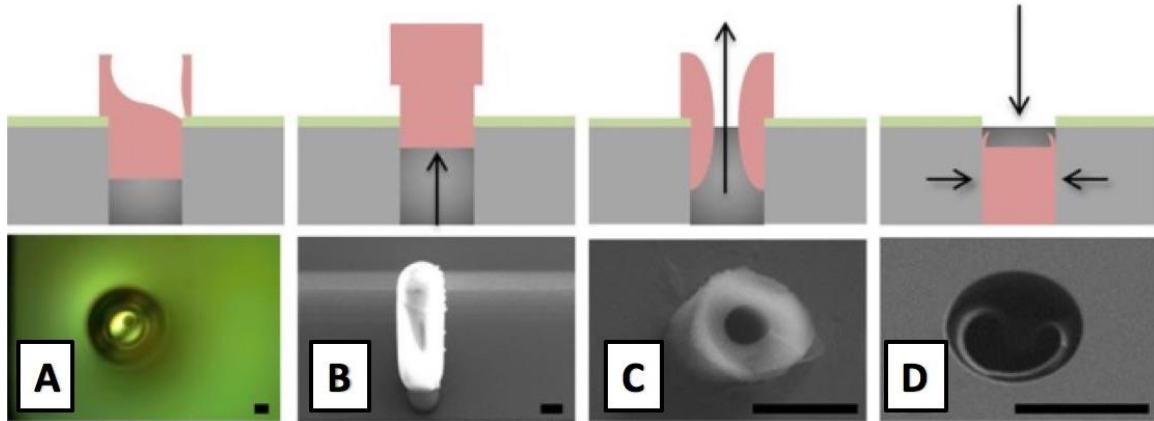


Figure 3-3 Processing Limits for Unity Plug: (a) bubble formation seeded by feature edges, (b) obtusion of the plug from expanding trapped air, (c) ejection of expanding trapped air and (d) shrinkage into the well from overly high solvent content. Scale bars are 10 μm .

Well Infiltration Methods

Several methods were evaluated for infiltrating circular wells. Test structures were formed in silicon wafers. Patterns of circles having variable diameters of 5, 7.5, 10, 14, 18, 70, 100, and 130 μm . A deepRIE etch was then performed turning these circles into 200 μm deep wells, an aspect ratio of 20 to 1.

Consecutive applications approach

Following the prewetting procedure described previously, the 2cP Unity was spun on the wafer containing the test structures, and post application baked according to the procedure outlined for the nanochannels in previous chapters. A consecutive application method was employed in which the same low viscosity solution that results in a discontinuity would be applied 2 or more times resulting in a buildup of material until a continuous film is formed over the well.

This method is reliable; however, complete filling of the cavity is always associated, along with the over shrinkage affect described, Figure 3-3(d). This is a result of the high concentration of solvent in the solution and the mass loss during bake out. While this technique is a feasible solution for shallow wells, it is less so for deep wells, especially those opening into a cavern like structure of much higher volume as required for micro to nanofluidic structures.

Positive pressure approach

For this approach, a thick (220 cP) Unity resist is first applied by spin coating onto a 100 mm silicon wafer. Prior to any post bake, the wafer is placed within a custom chamber developed for these trials, Figure 3-4. House nitrogen is applied to 50psi, forcing the resist into the well.

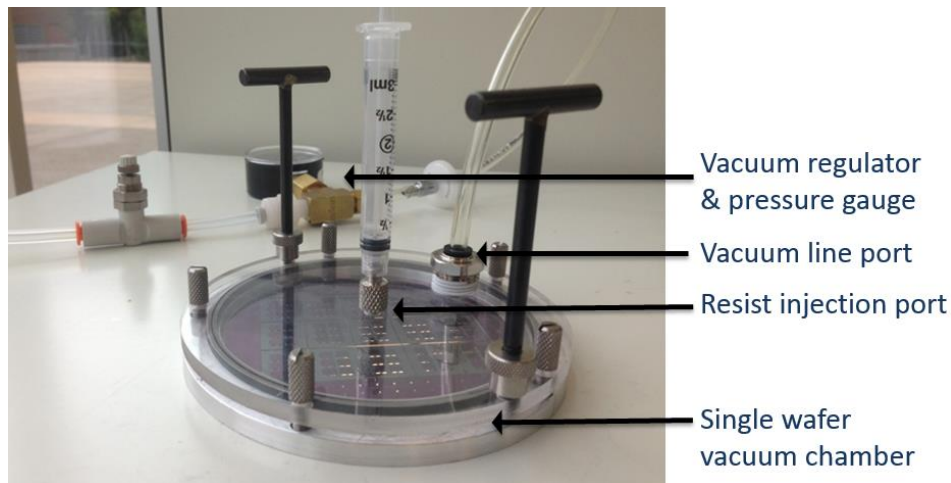


Figure 3-4 Custom Vacuum/Pressure Chamber for application and infiltration of Unity into the well.

Though the method easily achieves well infiltration for a wide range of viscosities, the gas ejection phenomenon, described in Figure 3-3(c), were prevalent. This could theoretically be

mitigated by performing the PAB while under pressure. This was tested, allowing additional time for the bottom plate of the chamber to reach temperature. The time constant for heating the aluminum base plate was 20 seconds, which was the additional time added to the PAB procedure. While the 220 cP resist was observed to have been able to densify and form a solid plug after exposure and development, this could not be repeated on the device wafer. Obtrusion of the plug (Figure 3-3d) was consistently observed across the wafer. It was thought that eliminating the gas within the chamber would mitigate the problem.

Application under vacuum approach

With this approach, the wafer is placed within the chamber prior to resist application and spinning. The chamber pressure is reduced below atmosphere and then the resist is applied. The theorized mechanism here, is that reducing the gas molecules within the cavity would eliminate the expansion seen to obtrude the plug during introduction of heat in following steps. Furthermore, infiltration could be achieved as the wafer is returned to atmospheric pressure. The chamber was modified to include the resist injection port shown in Figure 3-4. The issue, however was that the partial pressure of the Unity solvent is close to 1 atmosphere, such that the vacuum environment released the solvent, effectively solidifying the resist before it could be removed and spun to the desired thickness. While feasible, this method requires fine pressure control so as to avoid bringing the pressure near the vapor pressure of the 2-heptanone. Furthermore, vacuum chambers allowing for application of resist are uncommon to cleanroom environments. The final approach involves careful selection of the resist viscosity and processing parameters to achieve infiltration. This technique is described in the following section.

Viscosity Based Approach

The most controllable method involves selecting the lowest viscosity of resist that is conducive for spanning the hole while only partially infiltrating the well. The span of the resist must maintain at the spin speed and during solvent bake-out. The desired solution was identified by diluting the thickest COTS product (5.5 kcP) in increments until a balance could be found between shrinkage and reflow into the well. An HMDS pre-wetted silicon chip with sets of wells having diameters of 5, 7.5, 10, 14, 18, 70, 100 and 130 μm was spun at spin speeds ranging from 1500 to 4000 rpm with resists ranging from 5.5 kcP down to 4 cP. Resist viscosity and diameter dependency is realized. Four characteristic regions can be described. The first is the case when viscosity is low relative to the hole diameter. In this case, the complete discontinuity occurs. Resist may fill the well or simply coat the sides, but there is no resist spanning the well. On the other hand, if the resist is very thick relative to the whole diameter, the resist will span the well and no topographical evidence is observed. As resist viscosity is decreased however, a region of is observed for which dimples become visible. The dimples likely correspond to resist incursion into the well, the well may or may not be filled completely. The fourth is a small region for which the topographical profile is highly unpredictable.

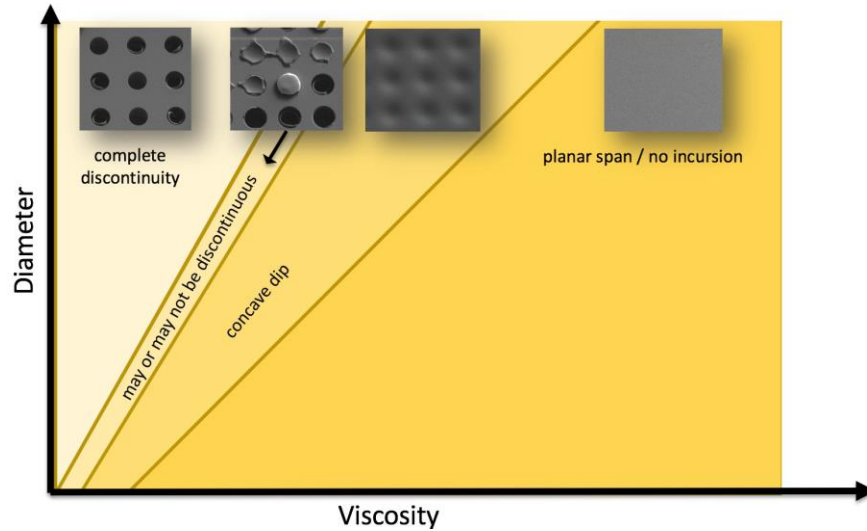


Figure 3-5 Resist Topography Dependence on Resist Viscosity and Hole Diameter

The objective is to use a very low viscosity so as to encroach on the region for which resist incursion into the well occurs, but discontinuity does not. Honing in on this region, detailed observations of the exposed plug profiles with a laser confocal microscope revealed a trend, Figure 3-6, one of which indicates a simple approach to forming a low profile plug for a variety of hole sizes, irrelevant of exact viscosity. This eludes the time consuming effort of iterating through many solutions of varying viscosities. The four regions are characterized by the ratio of the resist thickness to hole diameter ratio (t/d). A t/d ratio below ~ 0.8 results in a discontinuity, region “i” of Figure 3-6b. Between 0.8 and 1.2, a concave dip may be realized, though the dip depth is inconsistent and may even be discontinuous, region “ii” of Figure 3-6b. A highly repeatable trend was observed in a region between 1.2 and 1.8 in which the depth of the dip was consistent and proportional to the t/d ratio, region “iii” of Figure 3-6b. Beyond 1.8, the profile is planar, region “iv” of Figure 3-6b. This region encompasses both high viscosity cases in which there is no well infiltration as well as very low viscosity cases in which

complete infiltration occurs and reflow levels the dip. In either of these cases, the plug height is well above that which is of interest within this study. The third region (iii), indicates that the thinnest spin that should be performed should be roughly 120% of the hole diameter for this single application approach, and a dip of ~ 0.4 will be realized.

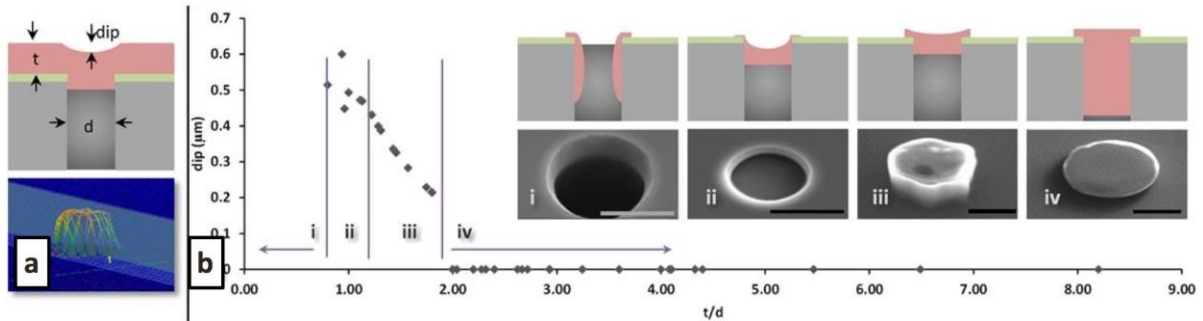


Figure 3-6 Plug Profile Dependence on Spin Thickness and Well Diameter: (a) plug profile can be catered according to its dependence on the ratio of spin thickness ‘t’ to well diameter ‘d’ and characterized by laser confocal microscopy. (b) Four distinct regions are realized: (i) below 0.8, a film discontinuity is certain, (ii) between 0.8 and 1.2, a concave dip tends to form, but with irregular depths, (iii) between 1.2 and 1.8, a concave dip tends to form with regular depths and (iv) for a t/d ratio above 1.8, resist film is found to be planar. Scale bars 10 μm .

3.3.2 FILM STRESS CONCENTRATION REDUCTION BY PLUG PLANARIZATION

The infiltration and exposure step may result in a plug with a height several orders taller than the desired channel layer. An excessive plug height combined with the directional nature of PECVD processes results in an unstable or nonexistent sidewall at the plug edge

Figure 3-7a. Planarizing methods were evaluated including plasma etching, mechanical polishing as well as pre- and post-UV exposure, chemical polishing with developer. For removing more than a micron but less than 3 or 4, plasma etching showed the best removal rate and consistency; however, surface roughness begins to take a toll beyond this

Figure 3-7b. Mechanical polishing provided good fidelity planarization but low yield on account of some plugs dropping into the well. Pre-UV exposure chemical polishing was done both by applying the developer solvent (2-heptanone) during spinning both by bottle stream and by mist at both low (500 rpm) and high (5000 rpm). Low spin speeds resulted in solubilization of the plug material. High spin speeds resulted in non-uniformity including 100+ microns tall striations.

While the mechanical polishing approach proved possible, the technique was excessively labor intensive on challenging to perform correctly. The buffered solution could not be performed without significant non-uniformity across the wafer. This resulted in outer wells with excessive material removed from the well while the inner plugs remained at near full height. An attempt to remedy the non-uniformity issue was made by employing the spin tool. The spin technique, though seemingly the simplest and most promising, could not be used to achieve planarization at spin speeds ranging from 100 rpm up to 1000 rpm (which is the limit that the tool will allow for with the lid open). The result, regardless of the spin speed, was a severely striated pattern of resist. This was also the case for mist applied solvent.

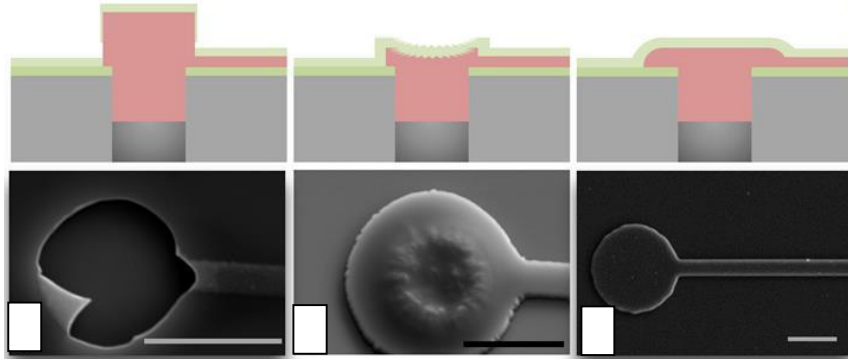


Figure 3-7 Topcoat Structural Stability Dependence on Plug Profile: (a) structural instability from depositing PECVD nitride on tall features is associated with the directionality of the deposition process and can be mitigated by (b) oxygen plasma planarization though not without severe roughening for etches greater than 2-3 μm though the best outcome (c) is observed for viscosity optimization combined with edge smoothing by reflow and/or solvent soaking. Scale bars 10 μm .

3.3.3 INTEGRATION OF A TWO PART UNITY APPROACH WITH COMPLETE CHIP FABRICATION PROCESS

This method is implemented using a wafer compatible processes for the purpose of high throughput batch fabrication, Figure 3-8. Three microns of thermal oxide mask layer is grown on a single crystal Silicon wafer (500 μm thick, prime grade, DSP, $\langle 1\ 0\ 0 \rangle$) using a Tystar nitride furnace.

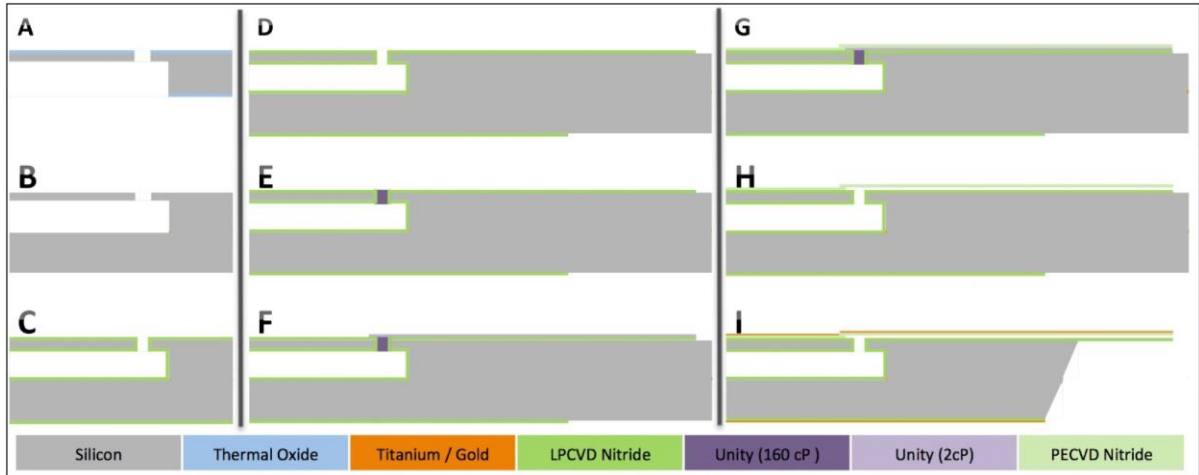


Figure 3-8 Two-Step Unity Microfabrication Process Flow for an AFP: Integrating the Two-Part Microfluidic to Nanofluidic Interface Method: (a) Thermal oxide growth and patterning, (b) gold diffusion eutectic bond, (c) LPCVD nitride growth and incursion, (d) cantilever patterning on top and release pattern on bottom, (e) incursion of high viscosity sacrificial Unity support structure into well, (f) patterning of Unity sacrificial channel, (g) deposition, patterning and annealing of PECVD nitride layer forming channel, (h) Unity polymer decomposition, (i) deposition of gold reflective and fluid sealing layers.

Lithography and Deep RIE is performed on both the top and the bottom of the wafer forming the trench and the well (Karl Suss MA6 TSA mask aligner and Oxford HRM plasma etcher: Bosch). The oxide mask layer is removed using a BOE 6:1 wet etch process, leaving a low roughness silicon surface suitable for bonding. A gold bonding layer is deposited on the bottom (trench side) by CVD (Denton Explorer E-Beam: 10 nm Ti, then 100 nm Au, 1 Å/s). A gold diffusion eutectic bond [68] to an identical (except 400 nm thick) wafer: first the wafers are laser scanned for concavity orientation using a Bowoptic stress analyzer; they are then oriented to have matching concavity to reduce residual bonding stress; they are brought into contact and pre-bonded (Karl Suss SB8E bonder: 10×10^{-4} mbar, 410 °C, 200N/cm², 1hr); and finally it is annealed (Tystar furnace: 2500 sccm N₂, 1100 °C, 3hrs). The 300 nm low stress LPCVD nitride device layer is grown (NH₃/SiH₄ = 0.5, 750 °C) using a Tystar nitride furnace

[56]. For the device to withstand the KOH etch release step at the end, nitride is required to incur into the channel, coating it. The well alone is not sufficient, so an $400\mu\text{m} \times 800\mu\text{m}$ “vent” is added at the center of the shared trench.

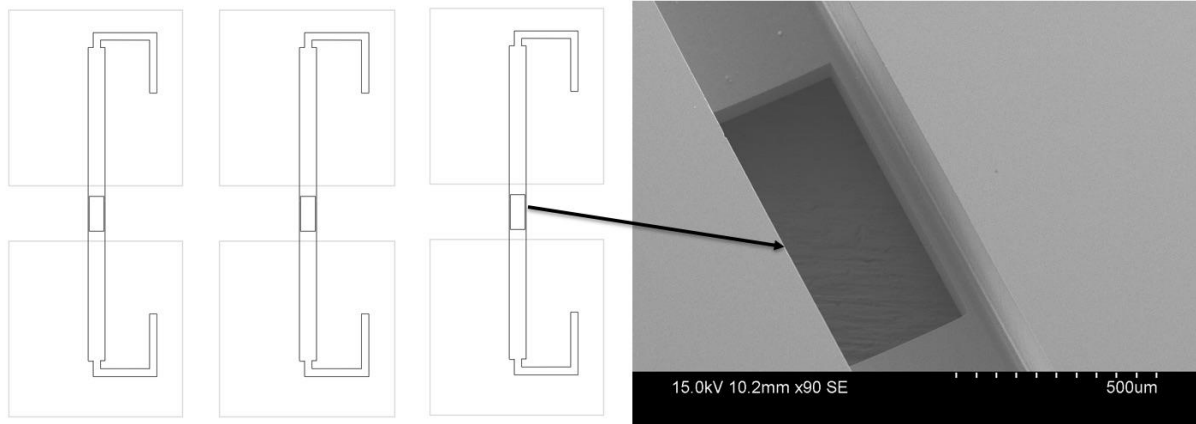


Figure 3-9 Vent Structure: A cluster of six dies. Each die shares a trench with another until the die is fully released. The vent serves as a topside gas vent during wafer bonding. A vent structure also serves to allow reactants to enter the trench during silicon nitride within the trench.

Lithography and plasma etch is performed on both the top and the bottom of the bonded wafers forming the cantilevers on the top and the cantilever release pattern on the bottom, using a Karl Suss MA6 TSA mask aligner and an Oxford HRM plasma etcher. A high viscosity Unity® 4678E (3000 cP):Toluene mixture (10:1) is spun on using a Karl Suss SB8 spinner, and allowed 5 min for incursion into the well, followed by selective photopolymerization. The surface is then oxygen plasma cleaned (Oxford Endpoint RIE: 300 mTorr, 300 W, 100 sccm O₂, 100 sccm Ar, 30 s) and a second, thinner Unity® 4678E (2 cP) layer is patterned, forming the fluidic channel. The 300 nm PECVD nitride device layer is thermally grown (Oxford ICP PECVD: 8 mTorr, 1 W RF, 500 W ICP, 13 sccm SiH₄, 12 sccm N₂ blend, 300 °C) followed by an anneal to remove the stress associated with low temperature deposition and high H+

concentration (Tystar furnace: 2500 sccm N₂, 1100 °C, 3hrs). The Unity sacrificial layer is then thermally decomposed (Lindberg Furnace: N₂ Purged to < 5 ppm O₂, 70 °C, ramped to 425 °C at 1 °C/min, 2 hr soak, ramped to 70 °C at 1 °C/min), followed by an identical gold reflective layer on the bottom and a gold hermetic enhancing layer on the top (Denton Explorer E-Beam: 10 nm Ti, then 100 nm Au, 1Å/s). This also serves to counteract bending stress from the gold reflective layer.

3.3.4 FABRICATION CHALLENGES

There are some aspects of the fabrication which can highly influence the characteristics and yield of the final device. Two distinct challenges are associated with the two-part unity fabrication method. The first is achieving a successful and hermetic bond. The second is obtaining uniform results in the micro to nanofluidic interface. These require further consideration due to their complex nature. Some of these fabrication challenges and their solutions are discussed below.

3.3.5 SELECTION OF WAFER BOND CHEMISTRY

Bonding methods aimed at obtaining a strong bond and hermetic seal were tested. The challenge is identifying a bond chemistry that is compatible with subsequent processing steps. For example, most bond processes require a mechanical pressure to initiate the bond; if the bond is performed after formation of the nanofluidic channels atop, the channels would be crushed. Process temperatures must also be considered. A low temperature bond technique can de-adhere if the the wafer couple is later processed at a higher temperature. Furthermore, if a metal element is used to form the bond, the wafer set may not later be processed in furnaces

used for CMOS processing. Another challenge is the existence of features at the bond interface. Features at the interface will typically have poor surface roughness from the processing used to form them. Additionally, air molecules within the cavity can be trapped and expand to form bubbles near the feature. Oxygen molecules can act as a reactant for some bond metals, thereby reducing the bond quality. Pulling a vacuum within the bonding chamber prior to applying pressure can reduce the occurrence of these phenomena; however, two wafers are typically placed on the loading arm of the bonding equipment as a pair, often already prebonded around a feature. Considering this, a vent feature may be added within the top wafer to allow air molecules to escape until vacuum is achieved. Finally, bonding chucks used within the research environment are typically used on small chips rather than wafers. A 100 mm wafer pair on the other hand is highly susceptible to the imperfect curvature of the chuck, and will easily crack under small pressures. First we describe the methods used to evaluate the bond quality and quantify the yield. Then we describe the approaches and chemistries considered to mitigate process challenges and achieve a hermetic seal.

Methods

The efficacy of the bond technique lies both in the yield and the quality of the seal. Bond yield is typically determined either non-destructively via IR transmission through the wafer pair or destructively via shear or tensile force separation. The nondestructive IR technique involves infrared transmission through the wafer stack. An infrared camera detects bond irregularities, including trapped bubbles and simply nonadhesion associated with poor contact, incorrect processing parameters, or contamination, Figure 3-10. A semi-quantitative characterization is achieved comparing the percentage of void areas to the whole wafer area.

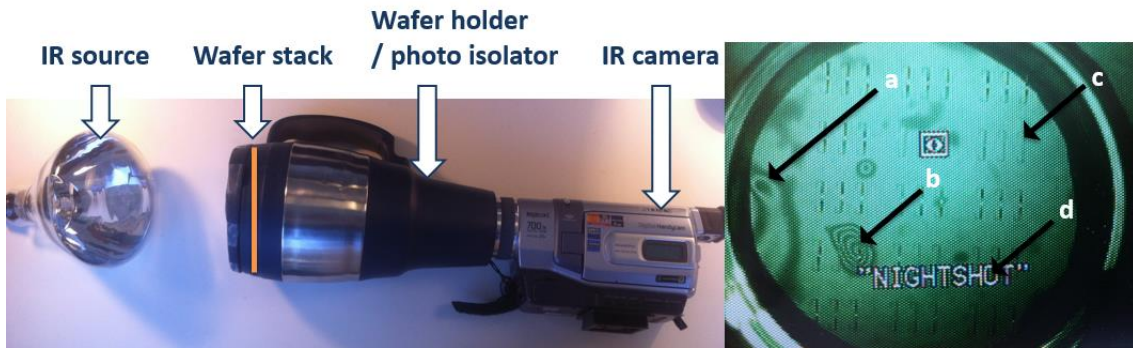


Figure 3-10 Schematic of Bond Quality Evaluation via Nondestructive Infrared Transmission: (a) poor contact, (b) bubble, (c) device features, and (d) camera artifact on a double stack of 4 inch bonded wafers.

While the interface where voids can safely be deemed as unbound (Figure 3-10a,b), seemingly bound areas can also have nearly zero bond energy. Therefore, destructive tests were also employed. With this technique, a 100 μ m razorblade is pressed at the wafer interface inducing a localized tensile force. As bond quality is not the primary focus of this study, force and angle were not quantified, rather specimens were qualified on a pass or fail basis. While these methods provide a good preliminary estimate of the bond quality on a wafer scale, it is very difficult to determine the bond quality at the individual chip. This is critical because a 4 mm square wafer has less than 16 mm² of surface area with which to adhere. Following the LPCVD nitride deposition step, a destructive test may be performed. Nitride incursion at the channel interface reveals how well the bond was performed and also eludes to the quality of the hermetic seal that will be achieved, Figure 3-11.

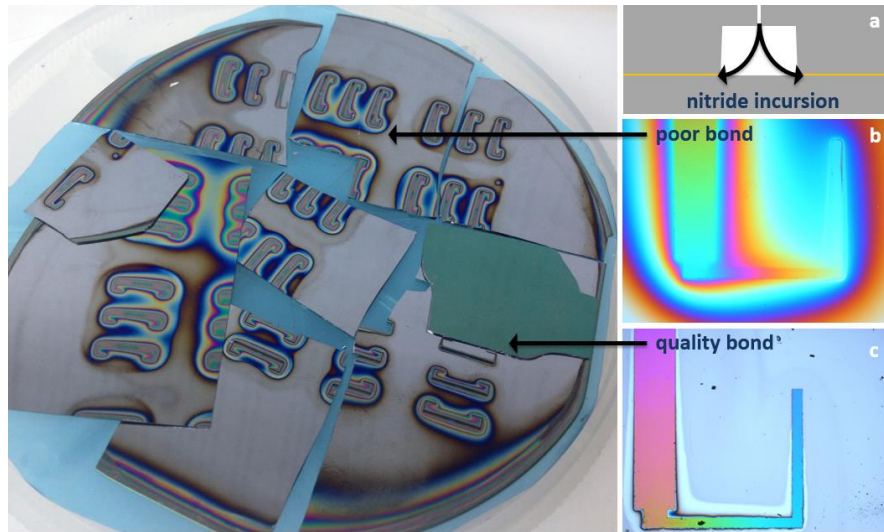


Figure 3-11 Schematic of Bond Quality Evaluation via Destructive Razor Blade Separation (a) Side view illustration of nitride incursion through well and the potential incursion within the wafer interface, (b) with both poor bond quality, (c) and good bond quality existing on the same wafer. Images are bright field; color gradient is an indicator of the nitride thickness.

Bond Chemistries

Bonding on the wafer level proved very challenging having very low yield. Considering the number of steps involved in the overall process, it was essential to get a high quality yield. A poor bond at the wafer edge can easily propagate to the entire wafer during later steps. While very high processing temperatures may serve to improve the bond quality, moderate thermal processing temperatures can stress the interface to no benefit. Likewise, mechanical stress from spin drying and clamping during plasma processing chambers can separate the wafer. Moreover, subsequent surface micromachined features may be in the only area of the wafer that has an unsuccessful bond, resulting in a net zero yield. It is therefore critical to obtain a quality bond across the whole wafer in these early stages of the process flow. Success rate of the approaches described in the following sections is qualitatively summarized in Table 9. If the wafer pair was continued through the remainder of the process flow, net chip yield is indicated. For each,

Table 9 Fidelity of Bond Approach

Bond Pair	Surface Prep	Approx. area without voids (net chip yield)
Au Eutectic	piranha + Ti adhesion layer	90%
Si-SiO ₂ -Al-Sn to Si-Al-Sn	piranha	0%
Si-Si fusion	Fresh wafers (no features)	99%
Si-Si fusion	piranha	0%
Si-Si fusion	RCA + dry activation	70%

Gold Eutectic Diffusion

A gold eutectic diffusion bond technique is a very attractive method [69]. This method is very forgiving of surface roughness and topography associated with features. This technique is easy to implement, facilitating a strong and uniform adhesion as shown in Table 9. Although a very forgiving attractive method for this application, it was later discovered that it would need to be replaced with a nonmetallic process to allow for annealing of the PECVD nitride device layer as previously explained, for the purpose of not contaminating the annealing furnace. Furthermore, the minimum anneal temperature of 800 °C required for the nitride film is well above the Au-Si eutectic temperature of 363C. The additional time and much higher temperature cause Au to continue to diffuse through the bottom wafer. The Au-Si chemistry at the interface has been shown to become inhomogeneous and bond strength is deteriorated[70]. It is noted that an SiO₂ layer may be inserted as an effective diffusion barrier below the Au/Ti stack, and lesser so Ni and Pt.

Aluminum Bond with Tin Intermediate Layer

Before shifting to an entirely non-metallic bonding mechanism. A recently described Al-Sn bond mechanism was considered [71]. The method uses a layer of Sn as a solid-molten flux

for wetting the Al surface. Tin melts at 230 °C which serves to wet the interface and conduct heat evenly to the Al. A low temperature bond is formed at just 280 °C. Aside from being able to bond at low temperature, the wetting mechanism in which Sn flows naturally into voids, enables bonding without applied pressure to the wafers. This technique would allow for bonding after the surface channels are formed, averting the contamination issue. Furthermore, The bond mechanism has been shown to produce high bond energies and quality hermetic sealing for MEMS accelerometer overmolding [72].

Two wafer sets would be paired, one pair with features at the interface and one without. Equal thicknesses of aluminum and then tin were deposited onto one side of each of four wafers to 500 nm via e-beam CVD (Denton Explorer). The wafers were oriented together and place in an oven for 1 hr under vacuum to reduce tin oxidation (Heraeus Vacuum Oven). The bond mechanism appeared to strongly adhere the featureless pair. A cross section of the bonded pair with features, however, resulted in a phenomenon known as spheroidizing. This phenomenon is evident at feature edges and is attributed to molten Sn squeezing into feature cavity. Because Sn and Al do not form a compound, the Sn alone beads into a sphere. The exact mechanism and cause is not fully known, it is hypothesized that the non-uniform bonding temperature distribution, Al-Si reaction uniformity, or Al surface oxide residuals is culpable.

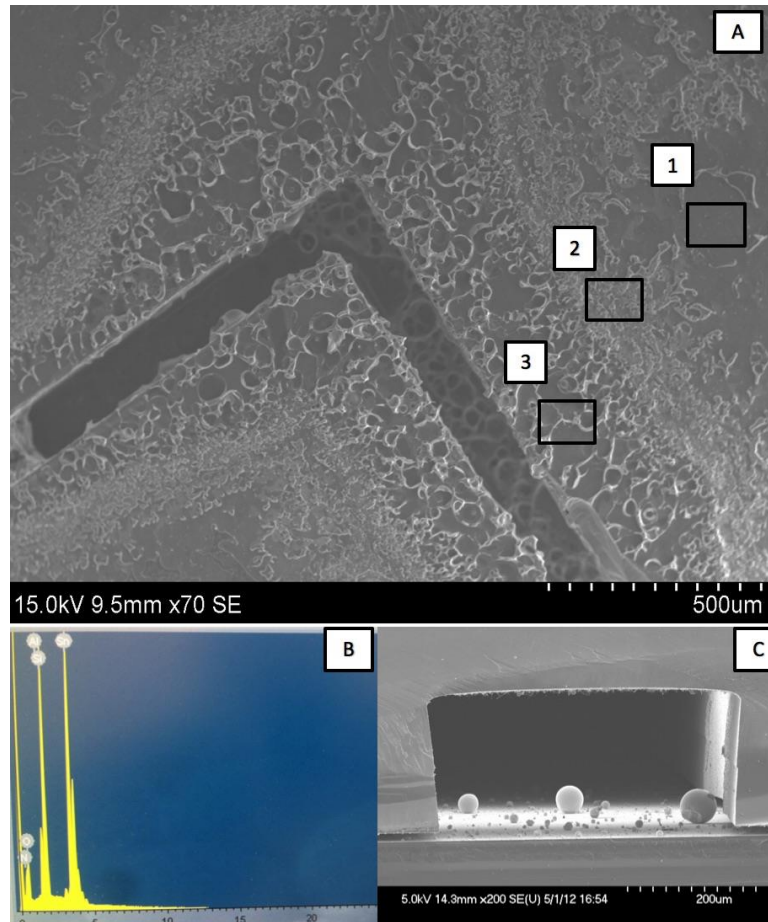


Figure 3-12 Aluminum and Tin Bond: analyzed by XDS indicates molten metal flux (XDS data for indicated regions of insert A are listed in Table 10). (c) A diced section view illustrates the phenomenon of spheroidizing Sn that is observed at the features.

As bonding mechanics is not the primary objective of this investigation, a thorough examination on this mechanism is left to future studies. It is noted however, that Al, Sn, and Si ratios measured by X-ray spectroscopy (XDS), showed nearly complete depletion of Sn from the further region (region 1), and higher concentrations close to the feature edge, with the spheres measuring almost entirely Sn. A look at the aluminum reveals, rather interestingly, that molten aluminum has flowed toward the feature along with the Sn; however, it does not bead. This may indicate that the flow is governed by the pressure gradient rather than a heat

gradient. Dissection of featureless wafer pairs may reveal the same toward the wafers circumference; however, this is left for future studies.

Table 10 XDS data for 3 regions illustrated in Figure 3-12 (wt%)

Region	Si	Al	Sn	N	O
1	80.86	2.74	--	3.58	12.82
2	25.8	29.67	28.12	4.53	11.88
3	8.19	4.31	83.49	1.06	2.95
spheres	--	2.74	97.26	--	--

The gap left due to this phenomenon was found to be unacceptable; the bond mechanism was thus abandoned for more well established and characterized mechanisms.

Silicon-Silicon Fusion Bond

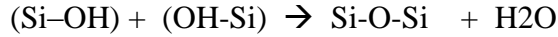
A Si-Si fusion bond is a viable nonmetallic solution that provides a bond strength that parallels bulk silicon properties. The method, however, is highly susceptible to surface roughness, surface chemistry, organic debris, and surface contamination such as hydrocarbons. These additional challenges require extreme quality control of equipment and monitoring for contamination. It is quite important to precisely understand the origins and mechanisms of voids to prevent them from the wafer bonding procedure. Voids in the interface have been classified previously as 1) aggregated trapped voids 2) thermal voids from thermal decomposition of surface contaminants such as hydrocarbons, and 3) reactant voids consisting of H₂O and H₂ that have been desorbed from hydrides at higher temperatures [73]. Recent works go on to describe a fourth cause which is the excess of byproducts from plasma exposure [74]. A fresh out of the box wafer bond was performed first as a control. Wafers showed a high bond strength, inseparable by razor blade. A set of six wafers were processed with the bulk micromachined trenches. Following removal of the mask layer by BOE, wafers were

paired with a fresh wafer. The processed and fresh wafer pair were measured for bow via a BowOptic stress analyzer and oriented for matching concavity. A prebond was performed on the first set via Karl Suss SB6 bonder at 450 °C and 5×10^{-5} mbar vacuum for 2 hrs ramped both up and down at 2 degree/min. This was to be followed by a high temperature anneal in a nitrogen furnace. However, bonding chucks used within the research environment are typically used on small chips rather than wafers. The 100 mm wafer pair consisting of a 500 μ m fresh wafer paired with a 400 μ m with deep (305 μ m) features, on the other hand, is highly susceptible to imperfections in the flatness of the tools chuck, and will easily crack under small pressures. Two graphite plates that are 4 mm thick each were placed above and below the wafer pair in an effort to normalize the pressure distribution and reduce cracking. However, this method was likewise unreliable. A low temperature prebond solution was desired. A low temperature prebond does not necessarily have zero voids at the interface before proceeding to the strengthening anneal, but the bond energy should be sufficiently high in the areas that are bonded so as to not debond from the vapor pressure from these molecules as the wafer is ramped to the anneal temperature.

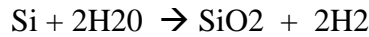
Importance of Surface Chemistry Effects

As can be seen in Figure 3-13a, piranha cleaned wafers with nearly no prebond voids had spontaneously developed large aggregate voids, Figure 3-13b, during the strengthening anneal performed at 1100 °C for 2hrs. The void remained after a second identical anneal. The size of the void and the inability of the bonded interface to propagate to the wafer edge implies the defect is a thermal void from contamination. The poor bond quality was mitigated through progressively more rigorous wafer cleaning and surface activation techniques. Surface

contamination would be resolved by employing brand new and dedicated beakers and carriers in performing an RCA clean. Furthermore, the HF etch, which is the final solution in the 3rd stage of RCA clean, would leave the surface less hydrophilic compared to the H₂SO₄ + H₂O₂ (piranha) solution. Silanol groups on a Si surfaces can condensate at room temperature forming Si-O-Si and water.



By definition, a hydrophilic surface contains more water molecules; this produces a higher concentration of reactants (H₂O and H₂) at the interface which form the voids at low temperatures. The size of the voids observed supports that the bond energy is sufficiently low that the reactant can aggregate.



At annealing temperatures, the H₂O would be consumed through the reaction and H₂ would readily diffuse. Literature suggests that a surface activation may be performed to reduce silane groups on the surface either by an O₂ plasma or warm nitric acid bath[74].

Table 11 Surface Preparation and Chemical Activation Methods

Method	Procedure	Description
Piranha	5:1 H ₂ SO ₄ (Sulfuric acid) + H ₂ O ₂ (peroxide) at 120°C	organic clean
RCA	SC1: 1:1:5 solution of NH ₄ OH (ammonium hydroxide) + H ₂ O ₂ (hydrogen peroxide) + H ₂ O (water) at 80 °C	organics and particles clean
	HF (hydrofluoric acid)	oxide removal
	SC2: 1:1:6 solution of HCl + H ₂ O ₂ + H ₂ O at 80 °C	ionic clean
Dry Activation	O ₂ plasma (200W, 30sec) Immediately in DI or Ammonium Hydroxide	hydrophilic activation
Wet Activation	Nitric Acid Immediately in DI or Ammonium Hydroxide	hydrophilic activation
AMI	Acetone + ultrasonication, methanol, isopropanol	organics and particles clean

The O₂ plasma technique, though easier to perform, was found to detrimentally increase the surface roughness, as will be discussed in the next section. Interestingly, it has been previously demonstrated that a plasma surface activation of less than 5s provides a lower surface roughness and an optimal silane surface density compared with the typical plasma exposure of 20s or 30s [74]. At room temperature, a prebond could then be achieved having only 2 or 3 voids ranging from 4 mm to 8 mm in size, Figure 3-13c. Following a strengthening anneal, the bond interface propagates, improving the bond yield from an estimated 40% to 70%, Figure 3-13d.

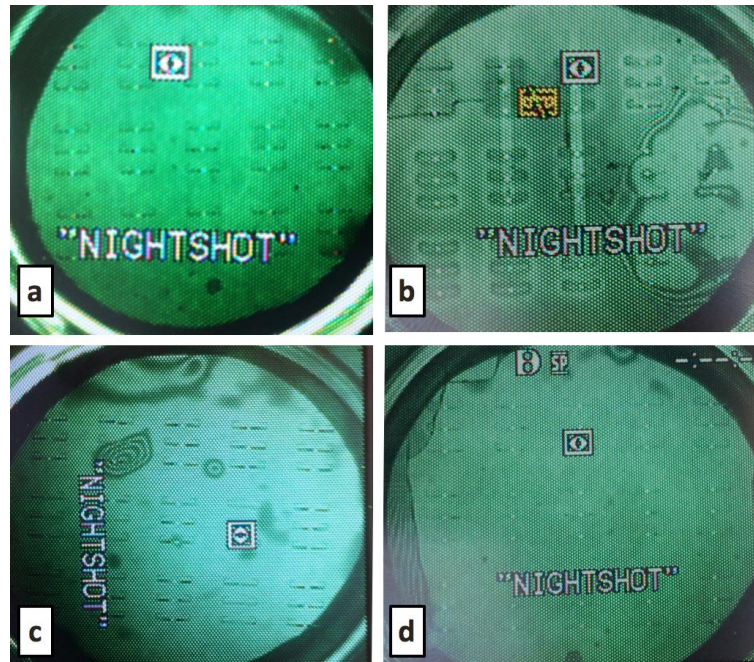


Figure 3-13 Direct Silicon Bond: Piranha pretreatment having now visible voids (a) develops large thermal void (b). An RCA cleaned and plasma activated Si bond having moderate voids throughout (c) is strengthened annealed allowing the bond interface to propagate.

At room temperature, the bonding phenomenon seems to be entirely based on weak van der Waals forces and hydrogen bonds between chemisorbed water molecules located on

opposing wafer surfaces [74]. Furthermore, new voids were realized after the the strengthening anneal. Considering that the fresh wafers bonded with considerable ease, it is assumed that the desorption of hydrocarbon contamination at the silicon wafer surfaces were diffused into the silicon lattice during the initial thermal oxide growth. Following the RCA clean, these subsurface molecules could not be removed. Upon annealing, small hydrocarbon molecules become mobile at the bonding interface and bubbles are nucleated at the interface.

Silicon to Silicon Dioxide Bond

A silicon dioxide layer at the bond interface has been shown to absorb reactants into the lattice or diffuse them across the wafer interface. The fidelity of this mechanism is limited by a minimum oxide thickness threshold. An oxide thickness of 2500 Å is said to be the minimum thickness capable of absorbing the contaminants and the byproducts [75], [76]. Pretreatments to date cannot achieve an oxide thickness greater than 100 Å and the plasma assisted wafer bonding technique give a maximum saturation oxide thickness of 60 Å [74]. The thermal oxide mask layer would then be repurposed so as to facilitate bonding. Poor topography and roughness are prevalent due to prior processing steps. As this is unavoidable, oxide would either need to be stripped and replaced with fresh thermal oxide or by polishing the existing oxide film.

Importance of Surface Roughness and Feature Topography Effects

For surface roughness's below 5 Angstroms, spontaneous adhesion is said to take place without any application of pressure [73]. Average surface roughness below 40 Angstroms is needed for low bond defect [74]. Surface roughness and feature topography issues were resolved through the use of a buffered oxide etchant which leaves the silicon surface with an average surface

roughness of 5.75 nm measured over four (100 μm by 100 μm) areas of the wafer, Figure 3-14, which is within the necessary order of magnitude necessary to perform the bond, [74].

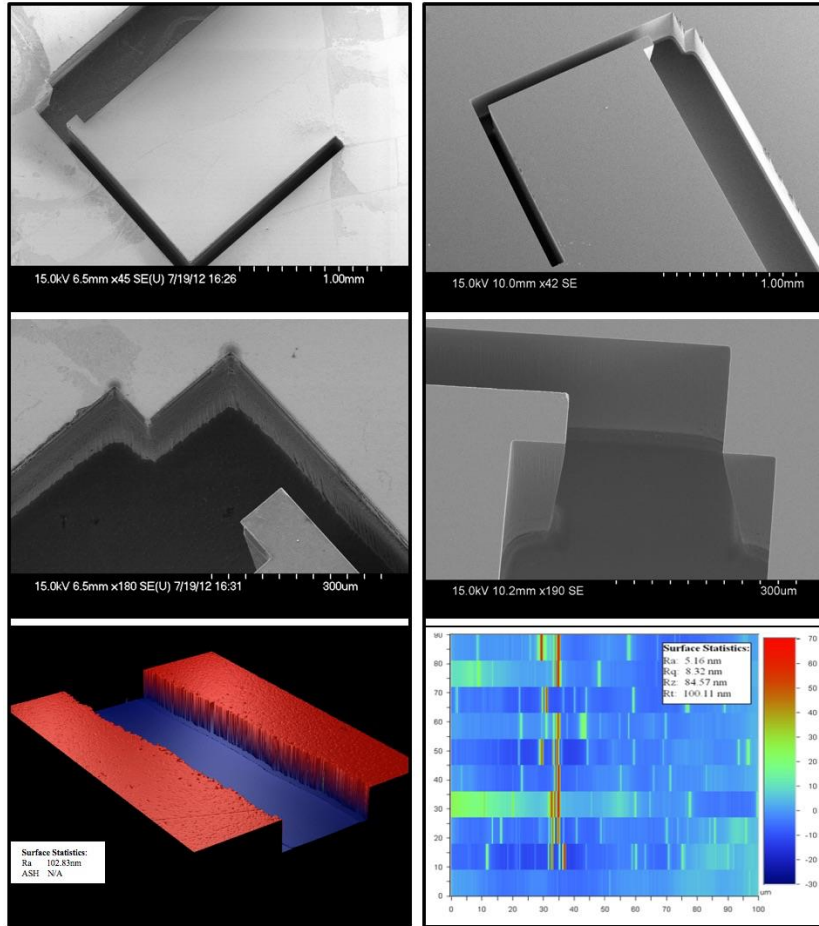


Figure 3-14 Surface Roughness and Feature Profile on Bonding Interface: Surface roughness map on Si surface post before BOE etch indicating average surface roughness of 102.83 nm on a Veeco profilometer (left column) and after with an average surface roughness of 5.16 nm (right column) Dektak profilometer

3.4 OXIDE ETCH STOP FABRICATION METHOD

A trench is first formed by deep reactive ion etching (DRIE) on the bottom side of an Si wafer (400 μm thick, prime grade, DSP, $\langle 1\ 0\ 0 \rangle$) (STS ICP, 305 μm). This is followed by a piranha clean and thermal deposition of an oxide layer (SiO_2) (Tystar mini furnace, 1 μm). A low stress LPCVD nitride is then deposited (Tystar nitride furnace). A low stress nitride layer is then grown forming the cantilever device layer (Tystar nitride furnace, 400 nm). Next, ten microns of AZ4620 is spray coated onto the bottom side of the wafer (Suss Alta spray coater), and the dielectric layers are selectively etched to form the well pattern. The well is then deep reactive ion etched (DRIE) up to the top surface using the oxide layer as an etch stop. A 10 μm diameter circle is patterned in the LPCVD layer via RIE etch (Vision RIE), also using the oxide layer as an etch stop. The low viscosity (2 cP) Unity is then spun on Figure 3-15, and patterned (Karl Suss Mask Aligner), Figure 3-15c. To accommodate the low decomposition temperature of Unity, a low temperature PECVD is deposited atop at 250 $^\circ\text{C}$ (Oxford ICP PECVD, at 250 $^\circ\text{C}$). Decomposition is achieved as described in CHAPTER 2.

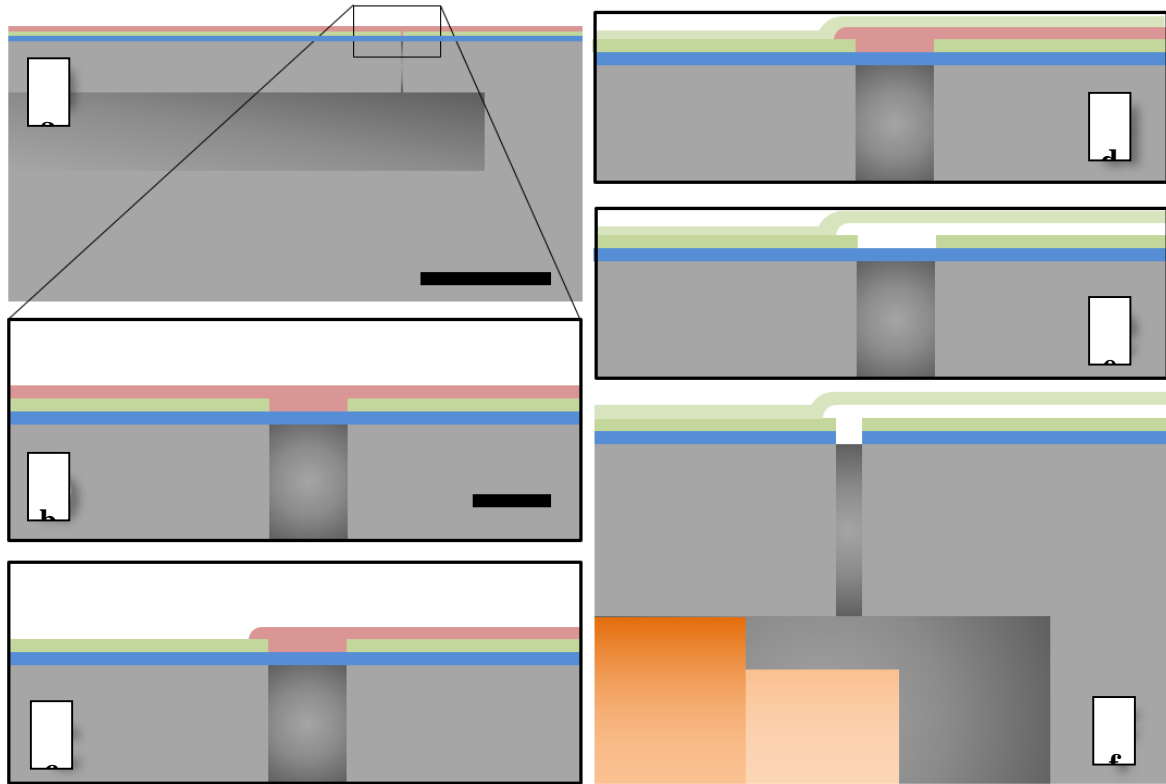


Figure 3-15 Oxide Etch Stop Method for Micro to Nano-Fluidic Interface: Fabrication via a thermally decomposable sacrificial polymer. A processed chip with bulk microfluidic features is enclosed by a bonding process and connected to the surface by a Bosch etched well from the bottom side and is limited by a 1 μm thermal oxide layer. The LPCVD device layer has also been RIE etched down to the thermal oxide layer (a). A close up showing the spun on low viscosity (2 cP) sacrificial Unity layer (b). The Unity is then patterned via exposure to ultraviolet radiation (c), followed by a low temperature PECVD nitride top coat (d), a decomposition bake (e), and capillary insertion (f), creating a continuous fluidic channel. Scale bars for (a) and (b) are 500 μm and 10 μm , respectively.

3.4.1 INTEGRATION OF ETCH STOP APPROACH WITH COMPLETE CHIP FABRICATION PROCESS

This method is a highly controllable and thus a high yield process, incorporating each of the techniques previously discussed, Figure 3-15. Ten microns of AZ4620 is first spray coated onto a Si wafer (400 μm thick, prime grade, DSP, $\langle 1\ 0\ 0 \rangle$) using a Suss Alta spray coater. Trenches are then Deep RIE etched into the silicon substrate (STS ICP, 305 μm). Following resist removal and a piranha clean step, a thermal oxide layer is grown on the top and bottom

surfaces which will later be used as both an etch mask and etch stop (Tystar mini furnace, 1 μm). A low stress nitride film is then grown forming the cantilever device layer (Tystar nitride furnace, 400 nm), Figure 3-16.

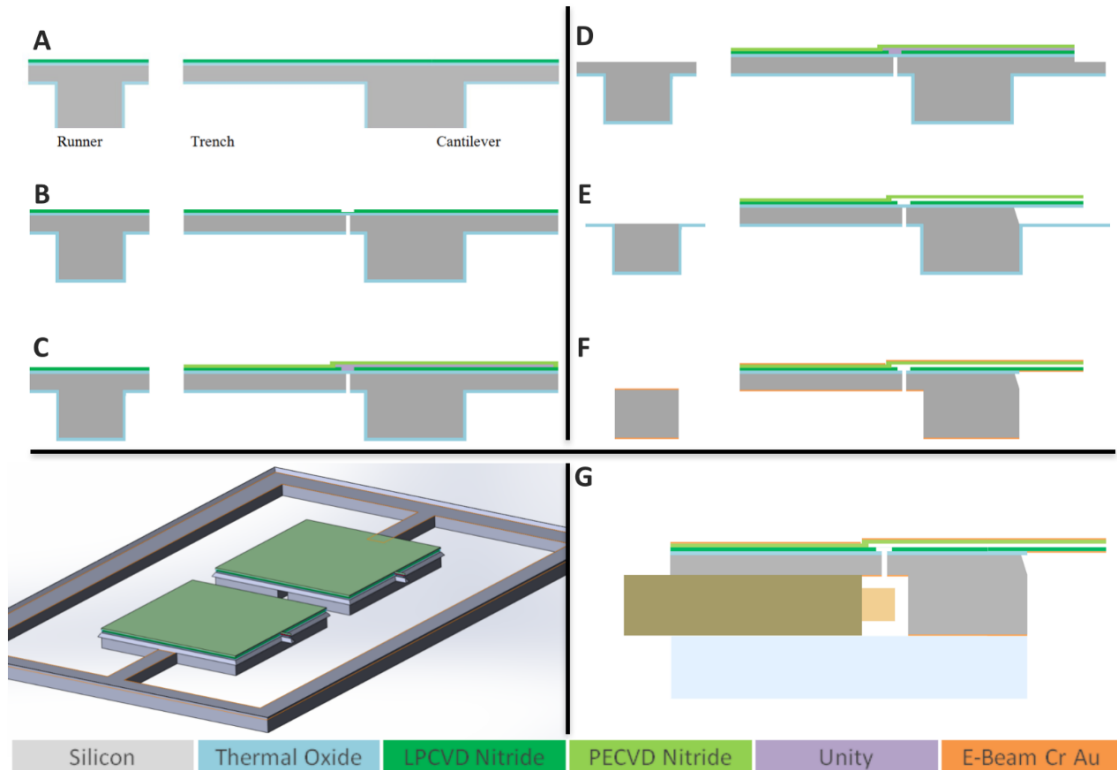


Figure 3-16 Oxide Etch Stop Microfabrication Process Flow for an AFP: Integrating the Oxide Etch Stop Microfluidic to Nanofluidic Interface Method: A $400\mu\text{m}$ $\langle 100 \rangle$ silicon wafer is used (a) $305\mu\text{m}$ Bosch etch of trench, $1\mu\text{m}$ thermal oxide, 400 nm low stress LPCVD nitride, Backside RIE of nitride layer (b) spray coated lithography within the trench, RIE etch of oxide layer, $95\mu\text{m}$ Bosch etch of well, top side RIE etch of nitride layer, (c) 4 cP Unity is spun and patterned, PECVD nitride deposition, (d) lithography of cantilever patterning on top, ICP RIE of nitride and oxide layers, $5\mu\text{m}$ Bosch of Si, (e) KOH wet etch release of cantilever and thermal decomposition of Unity (f) BOE wet etch of oxide layer and Cr/Au e-beam deposition on each side, (g) degating of a probe, insertion of glass capillary, and UV curing of Pyrex back piece. Piranha is used to clear the channel of particles and remaining sacrificial polymer scum.

The nitride layer is then removed from the back side (Oxford endpoint RIE). Photolithography of the well profile is achieved at the base of the trench using a spray coater (AZ4620, Suss Alta

spray coater, 20 μm). The oxide is then selectively etched via RIE (Oxford endpoint RIE). Carefully mounting to an oxide coated carrier wafer using crystal bond 509; the well is then Bosh etched through to the top side thermal oxide layer, using it as an etch stop (STS ICP, 95 μm). Backside alignment is employed to pattern a hole directly above the well into the nitride layer (Karl Suss BSA). The nitride layer is then RIE etched (Vision RIE 2). The sacrificial channel layer is applied in a single step using a 4cP Unity® 4678E (RC8 spin coater and hotplate).

The sacrificial layer must undergo a delicate cure process to ensure that all solvent is baked out while minimizing reflow according to the technique outlined in CHAPTER 2. Complete bake out of solvent is critical for ensuring a solid surface for deposition of the PECVD nitride layer (Oxford ICP PECVD).

The cantilever profiles are patterned and dry etched (Plasma-Therm RIE). The thermal oxide layer is patterned along with the base cantilever pattern within the same etch step. While the Unity sacrificial polymer may be thermal decomposed either before or after the KOH release step, the elevated wet etch temperatures used is better performed with the sacrificial channel removed so as to not damage the channel by thermal mismatch.

The Unity is thermally decomposed in a furnace according to the technique outlined in CHAPTER 2 (Lindberg Nitride furnace). The first phase of cantilever release is performed with a KOH etch. A BOE etch of the thermal oxide fully releases the cantilever and clears the oxide diaphragm at the well-nanfluidic interface. This is then followed by an identical gold reflective layer on the bottom and a gold hermetic enhancing layer on the top (Denton Explorer E-Beam: 10 nm Cr, then 100 nm Au, 1 $\text{\AA}/\text{s}$). This also serves to counteract bending stress from the gold reflective layer. To connect the glass capillary, a single probe is degated with tweezers

and paired with a previously diced transparent Pyrex chip identical in dimension to the die (4 mm X 4 mm X 500 nm). The capillary tube is set in the trench and a thin film of IC potting grade ultraviolet (UV) curable epoxy is spread onto the Pyrex chip with a razor blade. The tube is sandwiched in place and small amount of epoxy is placed on the side as a caulking. This has likewise been demonstrated using PDMS in place of Pyrex. Sulfuric acid is first streamed through the channel to clear it of remaining sacrificial polymer scum, noting that this should not be performed if PDMS is used as the backside substrate rather than Pyrex. The probe is then exposed to UV source at 405 nm allowing the light to penetrate the glass and cure the epoxy.

3.4.2 ELECTIVE CANTILEVER HEAD START TECHNIQUE

Because the cantilever release process using BOE is known to have a nonzero PECVD nitride etch rate, an optional Bosch etch was performed to expose the $\langle 1\ 0\ 1 \rangle$ plane of the silicon along the length of the cantilever, what this does is it allows the silicon bulk below the cantilever to etch simultaneously with the surrounding material, reducing the overall KOH etch time as well as maintain the critical PECVD nitride device layer, rather than exposing the device to this harsh etchant needlessly while the very slowly etched higher order planes are removed such as the $\langle 4\ 1\ 1 \rangle$ planes at the cantilever's convex corners (STS ICP, 5 μ m). The caveat of this is that under etching occurs around the die as well. While this may not be an issue for some applications, cantilevers with precise lengths are lengthened due to under etching at the fulcrum.

3.5 FABRICATION APPROACH DISTINCTIONS

Two fabrication approaches are described for creating nanofluidic channels on a chip surface that is linked to a subsurface microfluidic channel. The first is a two-part Unity approach in which a Unity plug is formed over a well, followed by lithography of a lower viscosity Unity to form the channels. The second method utilizes an oxide etch stop approach, in which the low viscosity channel is formed over a temporary oxide platform that is removed in the final steps to connect the channels. Each method presents distinct benefits and challenges.

Batch and Wafer Level Processing

From blank wafer to degating of the chip, the two-part Unity method uniquely enables higher throughput fabrication as it involves entirely wafer level processing techniques. This is a significant advantage and meets the general expectation for lower cost COTS products. The oxide etch-stop approach, however, requires that the well is etched from the bottom side, therefore the oxide platform is present at the point that the two wafers would be bonded. This 1 μ m film is highly delicate and can break under the processing conditions required to form the bond. This includes pressure delta as the bonding chamber is brought to vacuum as well as the compressive pressure to wafer stack. The dies are therefore necessarily independently and manually bonded after the cantilevers are released and the chip is degated. It should be noted that successful implementation of the aluminum tin bond technique may enable adaptation of the oxide etch stop method to be an entirely wafer level processing approach.

Ease and Repeatability

The oxide etch-stop method, on the other hand, has the distinct benefit of having less steps and being generally more repeatable in lower control environments. With the two-part Unity approach, it is challenging to obtain uniform results in the plug formation step.

Well Resolution

Finally, a better defined well shape and size is possible with the two-part Unity approach. This is because lithography is performed directly on the top surface compared with the need to pattern into a deep trench in which a mask/substrate gap exists and thus significant diffraction of the pattern. In Figure 3-17, it may be seen that a well formed 10 μm diameter well is patterned as designed, when patterning on the top surface as in the two-part approach. However, the gap that exists during the oxide etch stop approach is equal to the depth of the trench plus the resist thickness. In this case, the trench is 305 μm and the resist is 20 μm thick. The light diffraction causes poorly formed patterns between 63 μm -66 μm .

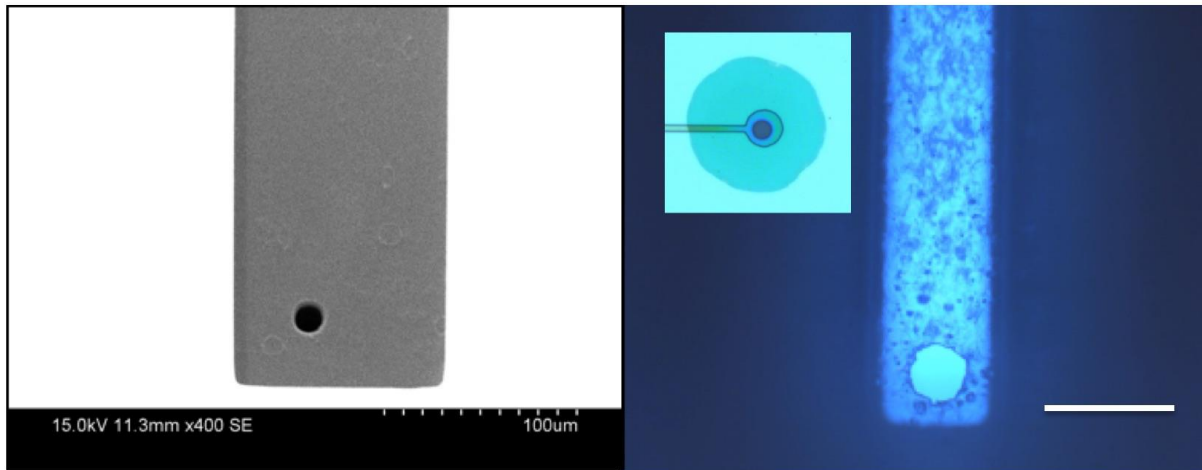


Figure 3-17 Distinction in Well Formation Fidelity Between the Two Approaches: By top down Bosch etch according to two-step Unity approach (left), and by bottom up etch via spray coated resist lithography within the trench (right), and topside view (inset). Both wells are Bosch etched through 95µm Si.

Overall, the oxide etch stop approach is more attractive in terms of fabrication as it is far more repeatable and forgiving, in cases where throughput is not a primary concern. An easier to implement fabrication processes tend toward higher yields, a considerable benefit for facilities with low to no quality control over fabrication equipment. Moreover, the bonding technique using a UV curable epoxy, though not conducive with automated fabrication techniques, is

considerably easier and cheaper to implement compared with the strict surface care that must be taken to achieve Si-Si or Au eutectic bonds.

3.6 INTEGRATED MACRO TO NANO-FLUIDIC

Precision pressure regulation within the nano-channel is achieved through a comprehensive fluidic system, Figure 3-18. A linear translator mounted reservoir is connected through reducing adapters to a 305 μ m diameter glass capillary. The capillary connects to the silicon chip using a polymer sleeve forming the sealed interconnect. Leakage was mitigated by utilizing a polymer sleeve around the capillary which was then thermoformed to fill in air gaps. We tested a variety of material and the heating recipes and found that PEEK provided a complete seal, whereas PTFE and PMMA were prone to leakage under the conditions tested. PEEK sleeves also offered the advantage to be more forgiving during the heating process due to its lower thermal expansion coefficient compared with PTFE and its higher working temperature compared with PMMA. Calibration is performed by setting the reservoir height at roughly the height of the fluidic chip and allowing the fluid to flow until equilibrium is achieved. Positive and negative pressure is regulated within the nanofluidic channel by lowering and raising the reservoir with the linear micro-translator.

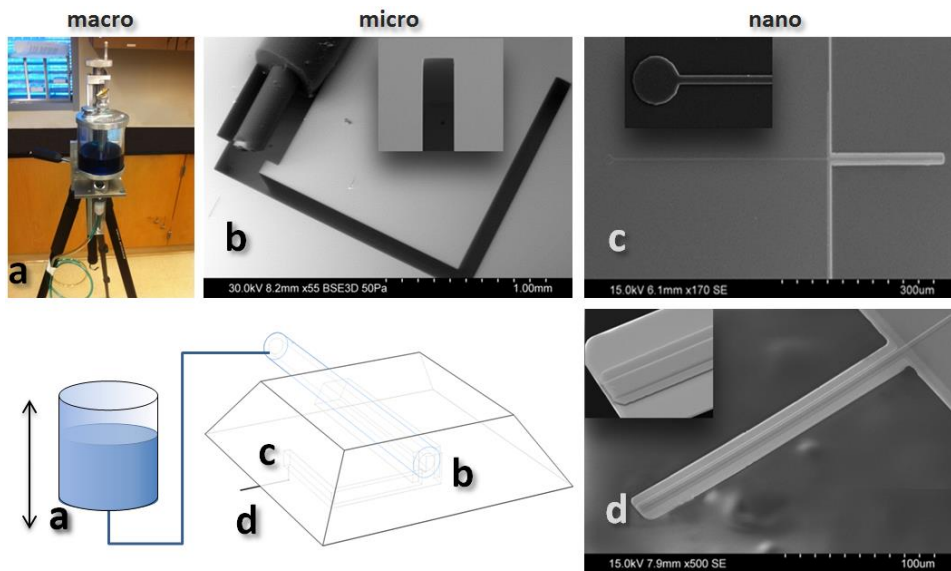


Figure 3-18 Complete Macro- to Nano-Fluidic System: (a) micromanipulator mounted reservoir provides either positive or negative pressure, (b) side mounted capillary with polymer sleeve seal and silicon based micro-fluidic channel, (c) micro- to nano-fluidic interface via a thermally decomposable sacrificial polymer and (d) 1 mm long, 2 μm X 300 nm nano-fluidic channel.

The aspiration of a cell at the AFP terminus requires fine pressure control. To achieve this, the nanofluidic channel must be connected to a system that may be manipulated on the macro level by the operator. The challenge is that such small pressures correspond to very low volume flow. Typical microfluidic systems will use a syringe pump to control fluid flow. This mechanism allows for volume flow rate control, often at very fine levels. For cellular aspiration, however, a very fine volume change can correspond to very large suction pressure at the terminus. A method of finely controlling the pressure would need to be developed. Furthermore, an AFM mounting chuck holds an AFM probe by sandwiching the top and bottom flat planes of the die with a metal clamp. This is not conducive for mounting traditional glass capillaries using top mounted capillary grips such as Nanoports™, which sit normal to

the surface and require a significant footprint on the chip. A side entry solution would be developed for connecting and hermetically sealing a glass capillary to the AFP.

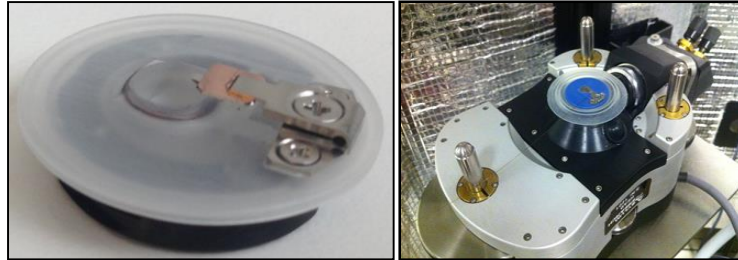


Figure 3-19 AFP Probe Mounted to AFM System Chuck: (left) clamping mechanism that makes out of plane capillary tube connection impossible. (right) in-plane capillary tube connected to AFP within AFM system

First, a highly controllable fluid pressure system would need to be developed. This would connect to a glass capillary. The capillary would then need to be connected directly to the AFP probe. The pressure system should apply fluid pressures on the order of 111 Pa [77]. Pressure transients should be within 5%. Lastly, glass capillary should be fabricated into the probe die directly. The design of this interconnect should be done in such a manner that noise due to mechanical vibrations originating from the pressure system or the environment should not propagate through the capillary to the probe.

3.6.1 PRESSURE CONTROL SYSTEM

Two pressure control systems were evaluated. The first was a compressed nitrogen system with controlled bleed to ambient. Fluid pressure in the capillary is controlled by flow rate of the bleeding gas. The second was a custom designed and built gravity system that uses vertical displacement of a supply reservoir to control pressure (Figure 3-20).

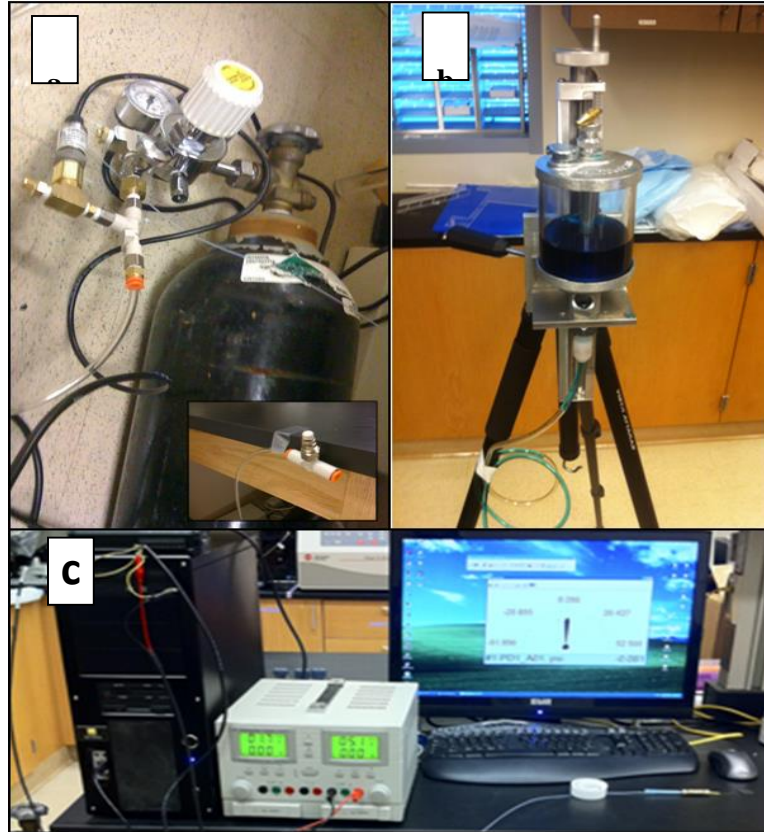


Figure 3-20 Two Pressure Systems Evaluated for Pressure Control: (a) compressed nitrogen system with pressure control by a flow resistance bleed to ambient, (b) gravity based system with micromanipulator for fine analog translation of a reservoir that induces both positive and negative pressures, and (c) in both setups, a pressure transducer relays real time pressure information to a computer.

The pressure control performance of each system was evaluated by connecting an inline pressure transducer to a computer via DAQ. A K562 cell was aspirated at the capillary tip; pressure fluctuation and controllability were evaluated. The nitrogen based system induced a noise floor that could not be mitigated through increased fluid resistance or other means. Furthermore, the gravity based system provided superior steady state control of pressure up to well beyond the needed 111 Pa with as little as 0.02% Pa resolution.

3.6.2 OPTIMIZATION OF THE PRESSURE CONTROL SYSTEM

The gravity based pressure control system was optimized to maximize pressure control resolution as well as reduce the noise floor and the existence of bubbles within the system (Figure 3-21). The reservoir is mounted on an analog micromanipulator. The manipulator, which was retrofitted to 6-axis camera tripod, can be tilted 90 degrees (~60 degrees realistically without air entering the tubing) from the vertical position (Figure 3-21a). This allows for enhanced vertical translation resolution, R , by $R \cdot \cos(\theta)$. A glass syringe is used in the initial setup to provide fluid backflow and force out air bubbles that enter the tubing prior to connecting tubes and adapters during setup. While reservoir to AFP terminus resistance is a function of the tube and channel diameters, length, and drag, it is nearly impossible to achieve the exact desired fluid resistance by controlling these parameters; therefore, it was necessary to add in a flow control valve (the fluidic equivalent of a resistor). This adjustable valve, with glass capillary adapter, provides a method of calibrating the system. The glass capillary is then connected through a side-entry interconnect in the AFP die, which is discussed in detail in the following section.

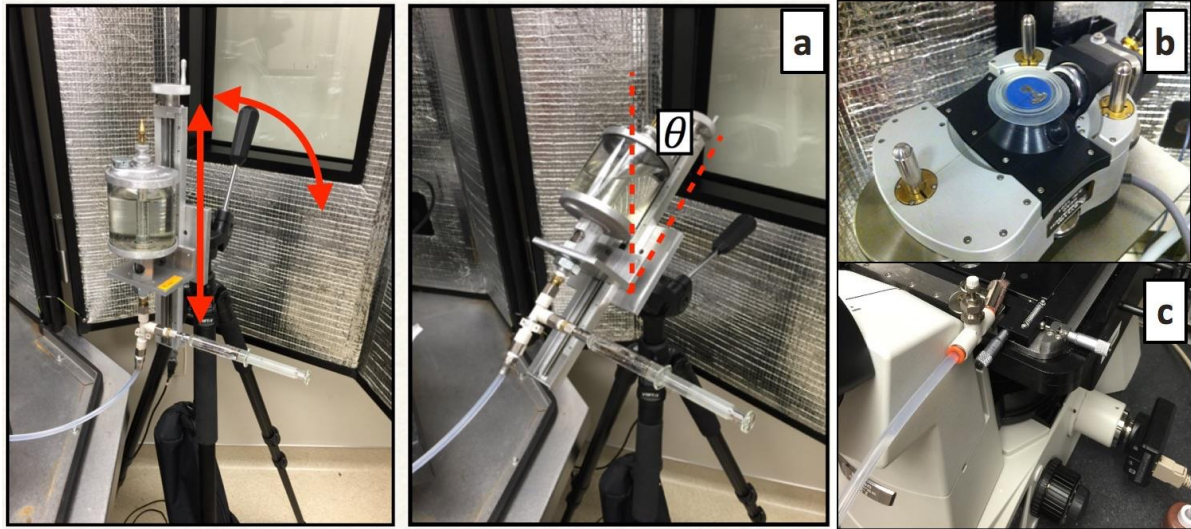


Figure 3-21 Pressure Control System: (a) A reservoir is mounted on an analog micromanipulator. The manipulator is mounted on a 6-axis camera tripod. A glass syringe is used to provide fluid backflow during setup to remove bubbles that exist in the tubing adapters during setup. (b) An adjustable valve, with glass capillary adapter, provides a method of calibrating the channel resistance. (c) Glass capillary connected through a side-entry interconnect in the AFP die, shown here mounted on the AFM system.

3.6.3 SIDE-ENTRY DIRECT TO CHIP INTERCONNECT

Next, a MEMS fabricated in-plane interconnect was developed. A variety of top down [78], [79] and in-plane [80]–[84] methods were considered. Our design is a combination of a leu lock like top down technique [85] and an in-plane trench technique [84] with a bonded wafer construct that encloses a 432 μm wide trench for insertion of the capillary tube. A compressible PTFE sleeve encases the capillary and is heated to fill the gaps. A photocurable epoxy is applied at the insertion orifice as a caulk. The sleeve acts to 1. create a water tight fit, 2. prevent accidental clogging of the fluid channel by the epoxy, and 3. dampen the transmission mechanical vibrations to the probe die. The AFP’s die is nearly double the width of a typical cantilever (4 mm total) to accommodate the capillary, and is compatible with the existing AFM

mounting assembly. The probe die is a 4 mm square, providing sufficient length for securing the tubing.

3.6.4 HERMETIC BOND CHARACTERIZATION

Each method used was tested for fluid leakage and sensitivity to vibration. Test structures were fabricated from 1.5cm square SC silicon chips. A Bosch anisotropic etch was used to form square trenches and a wet etch isotropic elliptical trenches. Samples were then gold sputter coated and eutectic bonded. The PTFE tubing was first inserted into the orifice, followed by the glass capillary and epoxy caulking. A teardrop accelerometer, with $\pm 30g$ peak range and 66.7mV/g sensitivity, was adhesively attached to the chip and about 2.5ft of glass capillary was connected to the pressure system with pressure sensor. Though the vibration could not be clearly quantified due to the dominating mass of the accelerometer itself, both the rectangular and elliptical interconnects demonstrated sealing up to pressures of 50 psi. The measured air leak rate at 690 kPa was 558 Pa, which was within the tolerance of the pressure transducer. Vibration noise to the die was instead assessed by gluing a capillary to a purchased AFM probe with proportionate stiffness and observing cantilever deflection. Rotation of the entire probe within the mount was found to be a concern. This and vibration noise was made negligible through sufficient tightening of mounting clamp and orientation of the capillary and pressure system, as well as avoidance of tampering. A simple approach and pull off from a glass slide in air illustrates the low noise associated with this setup. Strength of the remaining silicon under bending of the capillary was tested. No observable fracture in the silicon could be induced at forces below that of which would tear the capillary out.

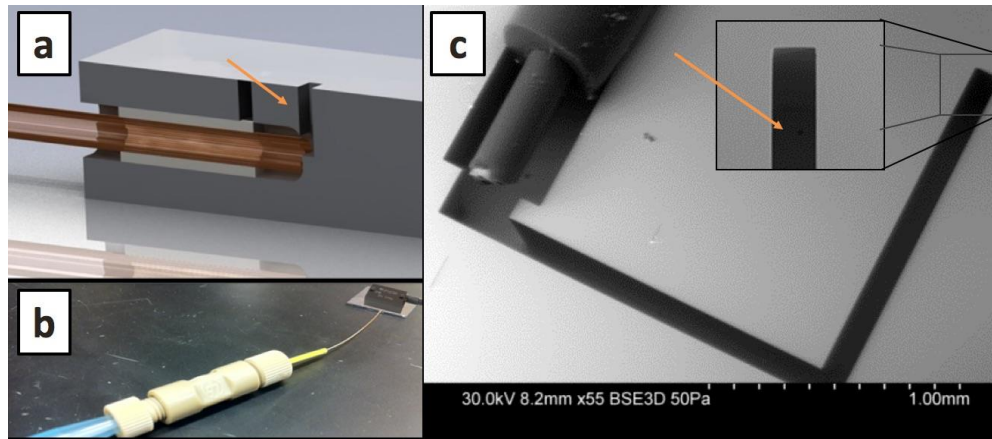


Figure 3-22 Schematic of Fluidic Interconnect: (a) Rendering of interconnect showing glass capillary and PTFE sleeve inserted into the formed trench within the bonded Si-Si wafers. Note the exaggerated well for illustrative purposes. (b) Pressure capacity and vibration noise floor tests of the interconnect integrity and (c) SEM of the assembly with a zoomed in view of the well (orange arrow).

3.6.5 NOISE FLOOR

When forces and distances to be measured correspond to thermal energy, the thermal fluctuation of the AFP becomes significant. Fluctuations in the air or fluid environment induce small force impulses from the diffusion of small particles (Brownian motion). Soft cantilevers are more susceptible to these thermal fluctuations. The amplitude of the fluctuations for a given temperature depends only on the spring constant of the cantilever [86]. The noise floor of the AFP with capillary connected is the deflection variation in the absence of any real signal. A thermal fluctuation curve, Figure 3-23b. This was analyzed using an Asylum MFP-3D atomic force microscope. The noise floor around the cantilever's resonance peak is between 1 and $1.4 \times 10^{-12} \frac{m}{\sqrt{Hz}}$, Figure 3-23.

Minimum Detectable Displacement

The deflection noise floor of the probe in air is the standard deviation of this fluctuation. This may be obtained from the non-contact region of the deflection curve, Figure 3-23a. Note that the distance between the probe and the glass is determined by the change in piezo height. If the cantilever deflects toward the sample, then the separation between the probe and the sample will be less. This can be corrected by subtracting the cantilever deflection from the piezo height. The minimum detectable displacement can be obtained from the deflection curve, as shown in Figure 3-23a. The deflection curve was recorded at 50kHz, chosen to be twice the resonance frequency of the probe as determined by the thermal fluctuation curve, Figure 3-23b. The minimum detectable displacement is 35pm. A resonance peak can be seen as the probe is retracted away and contact is broken following an adhesion event with the glass surface (blue). The data also shows a good hysteresis and good adhesion.

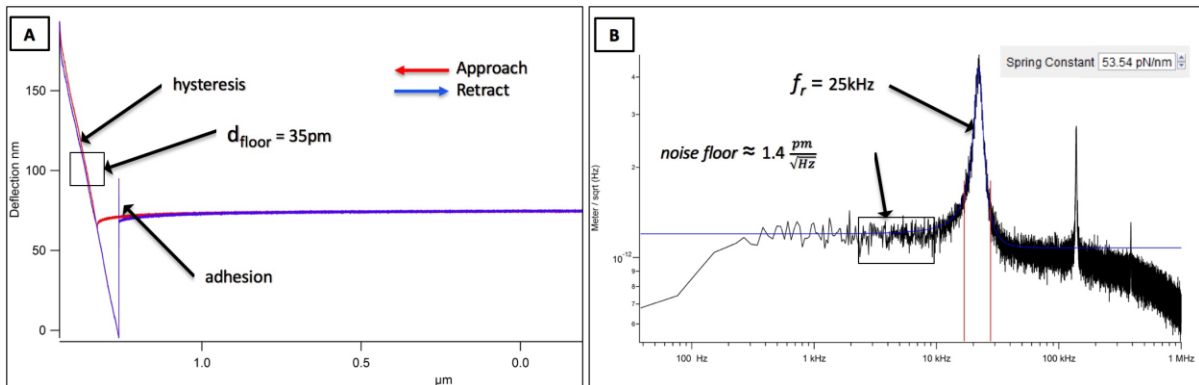


Figure 3-23 AFP Noise Floor: (a) Deflection curve as the AFP approaches a glass surface (red), and retracted (blue) shows minimum detectible displacement of 35pm. (b) Thermal noise measurement using the JPK software of a hollowed cantilever in air, showing measured cantilever resonance peak (black) and the Lorentz fit (blue). The fit indicates a resonant frequency of 25kHz corresponding to a spring constant of 53.54 pN/nm which is used to derive the minimum detectible force of 1.87 pN.

Minimum Detectible Force

The minimum detectible force can be derived using Hook's law and the minimum detectible displacement. One method of determining the spring constant is to use the resonance frequency, as was determined by a Lorentz fit of the thermal fluctuation curve, found in this case to be 53.54 pN/nm. The minimum detectible is thus 1.87 pN.

3.7 FLOW CHARACTERIZATION

The minimum pressure that can be applied to the system depends on the smallest increment by which the reservoir may be adjusted. In our case, a continuous translator with a position measurement of 0.001 inch (Velmex, Unislide), translates to a pressure change of sub 0.249Pa with water according to

$$(Eq. 15) \quad P_{reservoir} - P_{atm} = \int_0^h \rho g \cdot dh$$

Where ρ is the density of water (1000kg/m^3), g is the gravity constant (9.81 m/s^2), and h is the vertical translation of the reservoir. The maximum pressure that can be applied depends on the structural integrity of the channel as determined by the channel dimensions, as well as the PECVD nitride overcoat thickness and film quality. A 3-dimensional finite element analysis was first created within COMSOL, assuming bulk properties for low-temperature PECVD nitride [36]. Though the model may be used to identify stress concentration behavior according to channel geometry, fracture strength data from bulge tests indicates that the fracture strength behavior is primarily influenced by the fabrication process [87]. That is, the process parameters which influence pre-stress, membrane flaws, as well as the substrate material [88].

These must be determined experimentally in conjunction with geometric design. However, edge flaws may be minimized through edge smoothing on both the in-plane dimensions (by mask design) and out of plane dimensions (by resist reflow and surface roughness), using the computational model as a reasonable estimate. Future work will focus on the correlation between deposition and annealing conditions on film quality toward higher pressure maximums. The maximum pressure tested was 498 Pa across the fluidic entire fluidic system open to atmosphere.

De-ionized water was delivered through the system. The flow characteristics are given by the reduced Navier-Stokes equation for the velocity profile in the case of laminar flow of Newtonian fluid within a constant cross section

$$(Eq. 16) \quad \nabla^2 \vec{v} = \frac{1}{\mu} \frac{dp}{dz}$$

where, \vec{v} is the velocity, μ is the fluid viscosity of water, p is the constant pressure gradient, and z is the flow direction. By the time the fluid reaches the cantilever base, it has traveled 680 μm along the nanofluidic portion of the channel system; at this point we assume steady, axis-symmetric and fully developed flow. Following integration, the theoretical average flow rate may thus be described by the Hagen-Poiseuille equation

$$(Eq. 17) \quad v_{avg} = \frac{\Delta P D_H^2}{32\mu L}$$

where ΔP is the constant pressure gradient across the channel, D_H is the hydraulic diameter, and L is the channel length [89]. We use the square root of the wetted area ($\sqrt{A_w}$) rather than

the convolitional hydraulic diameter. We first estimate the pressure across the channel as a function of the applied pressure to the whole system. We use the fluidic equivalent of Kirchhoff's circuit law

$$(Eq. 18) \quad \Delta P = R_{fluid} \Phi = (\sum_{i=1}^n R_i) \Phi$$

where Φ is the volumetric flow rate (m^2/s), R_{fluid} is the fluidic resistance $(Pa \cdot s)/\mu m^3$ for n channels of varying cross sections in series. Calculating the individual channel resistances via the equation

$$(Eq. 19) \quad R^{1 \rightarrow n}_{fluid} = \frac{12\mu L}{wh^3} \left[1 - \frac{h}{w} \left(\frac{192}{\pi^5} \sum_{n=1}^{\infty} \frac{1}{n^5} \tanh\left(\frac{n\pi w}{h}\right) \right) \right]^{-1},$$

where L , w , and h are the channel length, width, and height, respectively, we may then estimate the pressure across the nanofluidic portion of the fluidic system [90]. In this case, the resistance of the nanofluidic portion of the system accounts for more than 99.99% of the total; therefore, we can reasonably assert that the pressure across the nanofluidic channel is equal to that of the applied pressure.

$$(Eq. 20) \quad \Delta P_{channel} = f(\Delta P_{applied}) = \Delta P_{applied} - R^{reservoir \rightarrow well}_{fluid} \cdot \Phi$$

The theoretical average flowrate is 34.3 $\mu m/s$ compared with the observed flow rate of 28.4 $\mu m/s$ Figure 3-24.

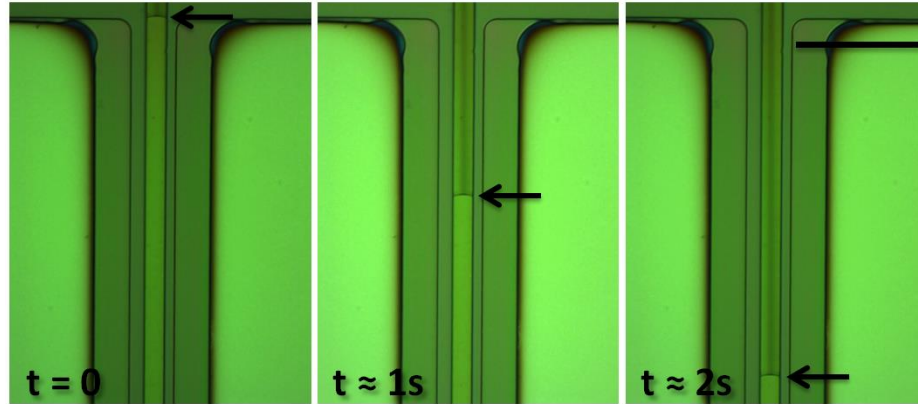


Figure 3-24 Deionized Water Flow Through a 500 nm by 3 μm Channel: Channel formed from low stress LPCVD nitride on the bottom and low temperature PECVD nitride on top, via a Unity sacrificial polymer. Scale bar 20 μm .

It should be noted that the inverse proportionality between fluid velocity and channel length indicate that the flow rate should be 23.3 $\mu\text{m}/\text{s}$ when the leading edge reaches the outlet. Such slowing down is not observed, however. This may be attributed to capillary force induced flow. The contact angle for the LPCVD and PECVD Nitride films were measured independently with a goniometer (Ramé-hart Model 250) following an oxygen plasma surface treatment having contact angles of 27.5deg and 19.6deg respectively. The channel walls after Unity decomposition, however, tend to leave the surface more hydrophobic owing to polynorborene residue on the channel wall. As the surface energy of the inner channel walls could not be directly measured, we repurposed the specimens from Figure 3-7a, with a 2 mm water droplet at the base of the channel. As described in previous works, capillary pressure can dominate when a basin is used as the fluid supply [41]. The observed flow rate was approximately 10 $\mu\text{m}/\text{s}$. Again using the Hagen-Poiseuille equation along with

$$(Eq. 21) \quad \Delta P \cdot A_w = F = \pi D_H \sigma \cdot \cos(\theta)$$

,where A_w is the wetted area, σ is the surface tension of water, and θ is the contact angle, we may estimate the channel to have an effective contact angle of 88.69° between the PECVD and LPCVD surface, which may be evidence of some amount of Unity residue. Previous work provides some evidence that surface treating the channel with sulfuric acid can reduce the residue and increase the flow rate, 7 fold in their case [41]. For the intended application of our cantilevers, the resistance within the channel is desired, as it provides hydrodynamic flow stabilization to the system.

3.8 CONCLUSIONS

In chapter 3, the first high sensitivity low stiffness nanofluidic channel is developed leveraging the capabilities of thermally decomposable polymer to form longer channels with smaller cross sectional areas. To integrate the cantilever into an AFM system and control pressure at the cantilever terminus, two key fabrication challenges needed to be overcome. The first was how to connect the $305\mu\text{m}$ diameter glass capillary from the pressure control system directly into the die of the probe. This allows the probe to be used on any brand AFM, without destructive modification to the probe holder or the need to give up the complex capabilities of current holders on the market. An original side entry technique is demonstrated. The second challenge is how to connect the surface based nanofluidic channel to the subsurface microfluidic channel. For this, two original fabrication methods are demonstrated. The key distinction between the two processes comes down to fabrication ease and repeatability versus fabrication throughput. The oxide etch-stop approach is more attractive in terms of fabrication as it is far more

repeatable and forgiving, which is more ideal for non-industry based cleanrooms of lower equipment quality control and cases where throughput is not of primary concern. The second method employs a set of entirely wafer level processing techniques for higher throughput. This technology demonstrates potential for other lab-on-chip microstructures for which channel cross sectional area is to be leveraged for testing at high shear rates and laminar flow conditions coupled with sensor systems in both aqueous and nonaqueous environments. Future works will focus on the integration of microfluidic networks in a complete sensor microsystem. As surface properties are a major concern, the characterization and the control of physicochemical properties of silicon nitride channels will also be considered.

CHAPTER 4 INTEGRATION OF ATOMIC FORCE MICROSCOPY AND A MICROFLUIDIC LIQUID CELL FOR AQUEOUS IMAGING AND FORCE SPECTROSCOPY

4.1 OBJECTIVE

In this chapter, a microfluidic liquid cell capable of high-resolution atomic force microscope (AFM) imaging and force spectroscopy is described. The liquid cell was assembled from three molded poly(dimethylsiloxane) (PDMS) pieces and integrated with commercially purchased probes. The AFM probe was embedded within the assembly such that the cantilever and tip protrude into the microfluidic channel. This channel is defined by the PDMS assembly on the top, a PDMS gasket on all four sides, and the sample substrate on the bottom, forming a liquid-tight seal. Our design features a low volume fluidic channel on the order of 50nL, which is a reduction of over 3-5 orders of magnitude compared to several commercial liquid cells. This device facilitates testing at high shear rates and laminar flow conditions coupled with full AFM functionality in microfluidic aqueous environments, including execution of both force displacement curves and high resolution imaging.

4.2 MICROFLUIDIC LIQUID CELLS FOR AFM

Atomic force microscope (AFM) [1] is a tool prized by researchers for its ability to image surfaces with nanometer lateral resolution and sub-nanometer height resolution. In addition, high resolution imaging can be performed in physiological environments, which include

liquids and physiological buffers [91]. Imaging in an enclosed physiological environment is typically accomplished with a “liquid cell”, which can be built in house [92]–[94] or obtained commercially. A liquid cell secures the probe and positions the microcantilever tip at the surface to be imaged while maintaining an enclosed and sealed environment containing a small volume of liquid, which can typically be pumped or heated. However, the current state of the art does not allow the use of a small liquid volume and uniform geometry which we expect will produce more precise control of the flow velocity field. Commercially available liquid cells enclose a volume of liquid using an O-ring gasket that measures approximately one centimeter in diameter or larger and typically enclose a volume of 50 microliters to several milliliters.

For many applications of the AFM, this relatively large volume of liquid is a major drawback. For instance, many proteins and other biomaterials are difficult to obtain in large quantities and prolonged imaging assays can only be conducted at very low concentrations of material. As a result, the study of the dynamics of crystal growth by proteins during biomineralization processes [95]–[97] is limited by the capability of today’s AFM liquid cells. Also current liquid cell designs contain significant “dead volume” in which reagent pumped to the sample does not distribute uniformly as a consequence of expanding flow lines from the inlet via through the flow cell [98]. A more well-defined flow field would allow a clear interpretation of real-time in situ AFM measurements of kinetic processes.

4.3 HISTORY OF LIQUID CELLS

Liquid cells for aqueous AFM liquid imaging have been described in the past [99], [100]. In general, the designs: 1) include transparent materials to allow the monitoring of cantilever deflection optically; 2) are able to hold the cantilever die firmly in place; 3) enclose the cantilever in a liquid-tight seal; and 4) allow the cantilever tip access to the surface of a sample during imaging or force spectroscopy. Many liquid cells are machined from quartz or plastic with a metal spring that holds the cantilever die in place. A recessed O-ring seals against the sample surface and defines the liquid microenvironment. A schematic is shown in Figure 4-1a.

4.4 CHALLENGES IN FABRICATION OF MICROFLUIDIC LIQUID CELLS

Shrinking the flow channel is stymied by the need to enclose both the cantilever, which is microscopic, and the substrate die, which is macroscopic having lengths in millimeters on two dimensions. The majority of liquid cell designs have a macroscopic gasket, which surrounds the entire probe including the cantilever and substrate die. The benefit of such a design is that the liquid cell is easily reusable.

4.5 PREVIOUS APPROACHES IN FLUIDIC CHANNEL VOLUME REDUCTION

Two approaches to decreasing the volume of the flow cell have been described. The first integrates the cantilever within a microchannel during the photolithographic fabrication process. The second fabricates the cantilevers and channels separately and then aligns the two

[101], [102]. These reports, however, describe designs for freestanding cantilever sensors and do not accommodate imaging or force spectroscopy—the AFM’s primary use.

4.6 APPROACH TO FLUIDIC CHANNEL VOLUME REDUCTION

In this report, we describe a liquid cell where the cantilever is integrated within a microfluidic volume that may be used for force spectroscopy and imaging [103]. We embed the AFM probe into the flow cell where the cantilever and tip protrude into the microfluidic channel. This channel is defined by the PDMS assembly on the top, a PDMS gasket on all four sides, and the sample substrate on the bottom, forming a liquid-tight seal. This design allows for much smaller enclosed liquid volumes, as shown in schematic in Figure 4-1b. By precisely aligning the cantilever within the microchannel, the volume surrounding the cantilever is reduced by three orders of magnitude or more. In addition, by using PDMS, a material permeable to gas, we can eliminate air bubble formation that is commonly found with commercially available liquid cell. Such bubbles can form quite readily especially for experiments run at physiological temperature and can quickly clog microfluidic flow and impede imaging. A three dimensional schematic of the fluid cell is shown in Figure 4-1c.

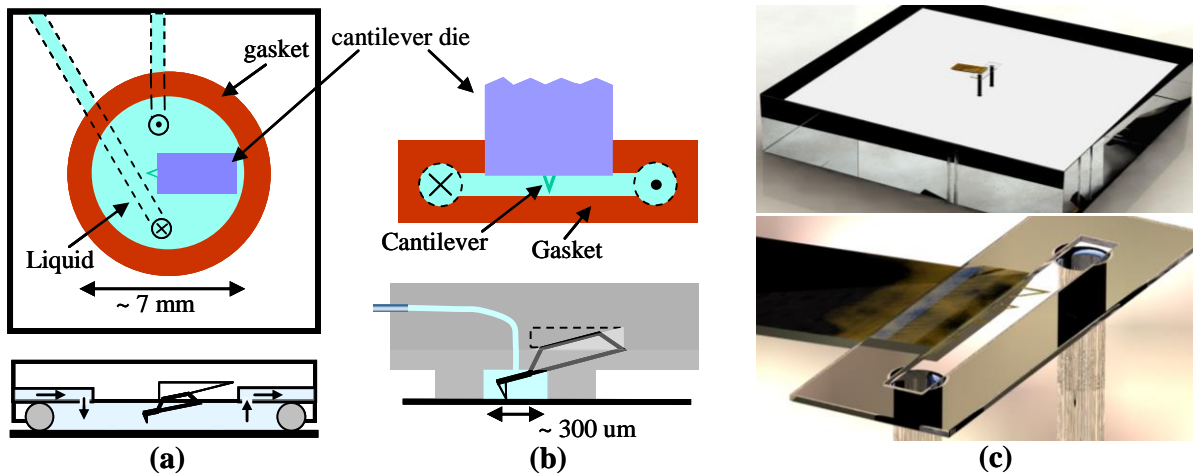


Figure 4-1 Microfluidic Liquid Cell Plan and Side View Schematics for (a) commercial liquid cell and (b) microfluidic liquid cell, presented in this paper. Labeled are cantilever die, gasket, liquid, and a small triangular cantilever off the die. In (c) we show a schematic of the microfluidic fluid cell with a zoom in to show the channel.

4.7 DESIGN AND FABRICATION

We formed the microfluidic liquid cell from three molded poly(dimethylsiloxane) (PDMS) parts, each assembled by aid of a long working-distance microscope (Nikon). The process flow of the design is shown in Figure 4-2a and was designed for use in the Multimode AFM (Veeco Metrology). Part 1 in Figure 4-2 holds the cantilever at the proper angle. Part 1 was formed by pouring uncured PDMS (Sylgard® 184 Silicone elastomer kit, Dow Corning) into a custom designed polycarbonate mold, shown in Figure 4-2b. A 13 degree ramp was milled into the polycarbonate mold. This produces a die shaped recess in the cured PDMS with a precise fit and angle for the AFM probe. The polycarbonate mold also provides a method to define inlet and outlet vias to either side of the cantilever. These vias are defined by 100 micron diameter

Teflon tubing (Upchurch). The tubing was inserted into two holes drilled into the polycarbonate mold on each side of the ramp, as shown in Figure 4-2a(i).

Uncured PDMS was mixed thoroughly with a ratio of 10:1 elastomer to curing agent and degassed under vacuum for 30 minutes to remove air bubbles. The PDMS was injected via a syringe into the mold and then cured in an oven at 60°C for one hour. The thickness of Part 1 was determined by a three dimensional Plexiglas box surrounding the polycarbonate mold to neatly contain the injected PDMS (Figure 4-2b). Four identical parts were made from each mold, which were then cut apart with a razor blade. Each assembled liquid cell has outer dimensions of 3 cm x 4 cm x 1 cm. In order to seamlessly interface pumped liquid into the liquid cell vias, we created metal inserts, pictured in Figure 4-2b, which molded voids matching the outer diameter of the 234 μm outer diameter glass tubing (Upchurch).

The cured Part 1 was then removed from the mold and the interior tubing removed to leave vias. A cantilever chip (NTESP, Veeco Probes) was secured into the recess with a drop of PDMS (Figure 4-2 a(iii)). The chip includes four v-shaped Si₃N₄ cantilevers ranging in length from 85 μm to 320 μm .

A second molded PDMS component (Part 2) was added next as shown in Figure 4-2a (iv). Part 2 surrounds the cantilever die on four sides and provides a uniform platform upon to which the gasket was secured. The thickness of Part 2 was designed to be slightly smaller than the distance from the top of Part 1 to the base of the cantilever, as measured using optical microscopy. Part 2 was adhered to Part 1 with uncured PDMS which seeped into the air gap between the two PDMS pieces and was cured to secure into place.

The third molded PDMS piece was the gasket, which forms the microfluidic channel. The gasket mold was microfabricated using SU-8 (SU-8 2025, DuPont) photolithography¹⁶ which

creates highly accurate definition of PDMS sidewalls and channel height. SU-8 was spun onto a silicon wafer and prebaked. Recommended procedures were used for spinning and development of SU-8, according to the respective layer thickness. Several gasket molds were created with thicknesses spanning 50 to 80 μm . An example of a gasket mold in SU-8 is shown in Figure 4-2c.

To form the gasket, a small amount of uncured PDMS was added by applicator into the mold, squeegeed using a sharply-cut thin rubber square, and baked at 60°C for 60 minutes. The PDMS gasket forms an interior rectangular channel which is 2700 μm x 300 μm and approximately 65 μm thick. The longest cantilever (320 μm) was removed because it was slightly longer than the width of the channel (300 μm). The length of the channel formed by the gasket was chosen to span the width of the cantilever die as well as the inlet and outlet ports. The thickness of the gasket must be designed so that the bottom of the gasket, which contacts the sample surface, is closely aligned to the freestanding cantilever tip. This ensures that minimal gasket compression is required before the tip contacts the sample surface during operation. This thickness is depicted by the double arrow in Figure 4-2a (v).

A suite of gaskets were made with varying thicknesses which allowed us to achieve the precise offset between the probe tip and the gasket. The offset was measured using optical microscopy for each liquid cell. PDMS gaskets were formed with thicknesses ranging from 50 μm to 80 μm in increments of 10 μm and were selected for each liquid cell to be within +/- 5 μm of the probe tip and aligned to the cantilever under a microscope. The gasket was then bonded with a small amount of PDMS for a tight seal. The assembled liquid cell could now be inverted and pressed against a flat surface so that the gasket enclosed the cantilevers, as shown in Figure 4-2a (vi). For well controlled flow, a syringe pump (Harvard Apparatus) was used.

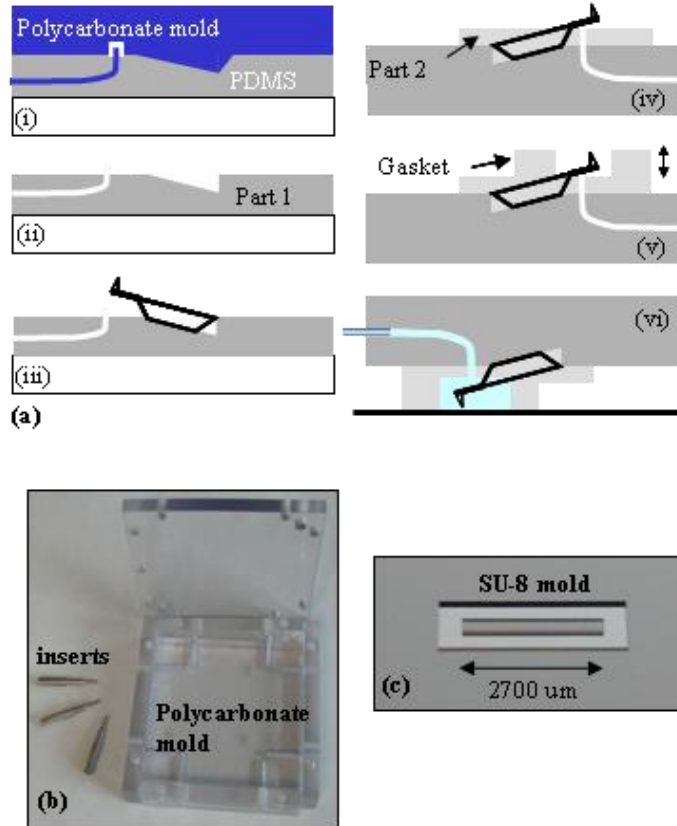


Figure 4-2 Fabrication of Microfluidic Liquid Cell. (a) Process flow for liquid cell fabrication. (b) Square mold for PDMS injection and custom inserts defining tubing interconnects. (c) Mold for a channel defined in SU-8 polymer.

4.8 DEFLECTION SENSITIVITY CHARACTERIZATION OF LIQUID CELL

An optical micrograph of an assembled microfluidic liquid cell engaged with a surface is shown in Figure 4-3a. The triangular cantilever and one inner edge of the PDMS gasket are shown and we highlight the close assembly of the gasket surrounding a 220 μm microcantilever. A scanning electron micrograph is shown in Figure 4-3b and 3c to provide an improved vantage and depth of field of the microfluidic channel surrounding the cantilever.

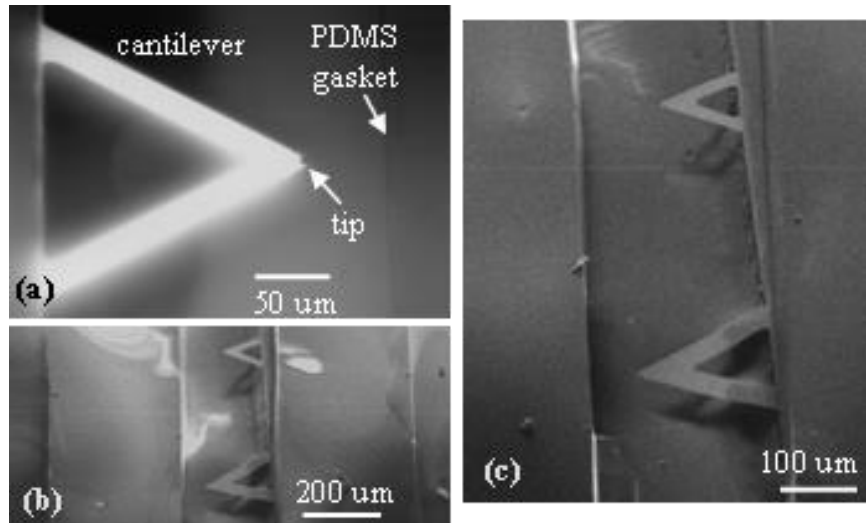


Figure 4-3 Deflection Sensitivity of Cantilever in Liquid Cell. (a) Optical image of freestanding lever submerged in aqueous environment bounded by PDMS gasket which forms a microchannel (b) and (c) SEM image of lever and gasket.

We first characterized AFM operation with the microfluidic liquid cell by completing force-distance curves, which are also used to determine cantilever displacement sensitivity. In a force-distance curve measurement, the cantilever deflection is recorded as the sample surface is raised and lowered slightly such that the tip briefly makes contact with the surface, deflects up, and then is drawn out of contact, as shown schematically in Figure 4-3a. Data from this measurement were collected on a Veeco MultiMode AFM with NanoScope IIIa controller. The recorded trace during retraction is shown in Figure 4-3b. In this experiment, the liquid cell was sealed against a flat glass surface and deionized (DI) water was applied with a syringe. The gasket was compressed by the glass sample with a computer controlled stepper motor until deflection was recorded. The amount of compression of the gasket necessary for the tip to make contact varied from device to device, but in general occurred within 5 microns. The z-axis piezotube actuator was used for accurate and linear motion. A vertical range of 4 microns was used during the force curves. The cantilever was indented 2 microns and then retracted (region (i)) until the cantilever was no longer touching the surface (region (ii)).

4.9 CHARACTERIZATION WITHIN AQUEOUS ENVIRONMENT

Our second demonstration of AFM operation with the microfluidic liquid cell was imaging in an aqueous environment. For this measurement, we used a silicon calibration grating with a one dimensional array of triangular steps having a precise linear and angular dimensions defined by the Silicon $\langle 111 \rangle$ crystal planes (TGG01 Grating, MikroMasch). Images were taken in contact mode and scanned $10\ \mu\text{m}$ by $3\ \mu\text{m}$. For comparison, we show both a commercial liquid cell image in Figure 4-3c as well as the microfluidic liquid cell image in Figure 4-3d. A line scan cross section perpendicular to the grating is also shown in Figure 4-3e, revealing the topography of the triangular steps. For these measurements, the rough surface of the sample prohibited a water-tight seal, and therefore no flow-through measurements were made.

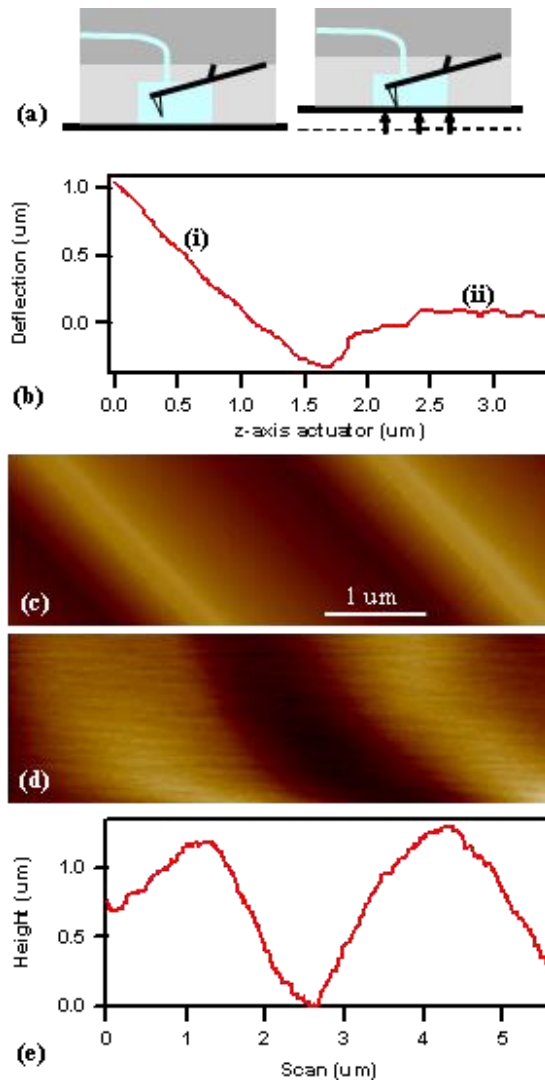


Figure 4-4 Force Curve within a Microfluidic Liquid Cell. (a) Schematic of force-distance curve resulting from the vertical compression of the gasket. (b) Force-distance curve on glass. (c) AFM image of a line grating by standard liquid cell and (d) the microfluidic liquid cell. Note the nonlinearity that occurs

4.10 CHARACTERIZATION OF LAMINAR DYNAMICS

Our final characterization of AFM operation with the microfluidic liquid cell was an analysis of the liquid cell's low Reynolds number laminar flow. This was done through a series of time lapse still frames taken from a video recorded with a 20x objective magnification (Figure 4-3). The video was acquired with a Nikon Ti-E inverted microscope with brightfield transmission

illumination. In this example, the liquid cell was engaged against a flat PDMS sample surface under a slightly compressive force. Although AFM imaging was not performed simultaneously with flow in this example, the applied pressure could be modulated and the cantilever deflection recorded by visual inspection. Pressure driven flow from a syringe was created and small 4 μm microbeads (Bangs Labs) were suspended in the DI water to aid in flow visualization. In the time lapse images at 15 frames per second, beads travel at a speed of 0 to 500 $\mu\text{m/s}$. The upper value corresponds to a volume flow rate of ~ 10 nL/s.

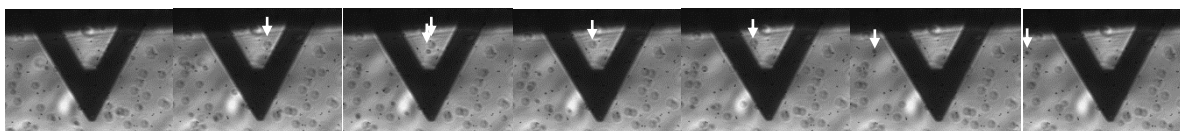


Figure 4-5 Microparticle flow within Fluidic Liquid Cell. Still frames taken from video microscopy visualizing the flow of microparticles flowing lamarily through the microchannel. Each frame represents 1/15th of a second. Two arrow tracks a two particle through the series.

4.11 DISCUSSION

Here we describe the design and fabrication of an AFM liquid cell with microfluidic dimensions, as well as its practical use in typical AFM applications. There are several areas where this device may prove useful and potentially transformative.

Atomic force microscopy has become a vital tool in the study of molecular dynamics of biomineralization [98], [104]. However, quantification of kinetics and thermodynamics of protein adsorption to crystal surfaces requires a constant flow of protein to replenish the depletion layer and overcome mass transport limitations [98], [105]–[107]. Modification to commercial fluid cell designs can provide a simpler geometry that allows calculation of flow conditions[105]. However, no AFM liquid cell designs achieve the minimum flow barriers and

simple flow geometry that are demonstrated with our design. Videos taken of liquid flow reveal a laminar flow that is not obstructed by the probe die, as occurs in traditional designs [98]. Flow lines revealed by the microparticles trace a straight path, though the velocity of particles can be erratic due to interaction with the sidewalls of the channel. Nonetheless, we expect a dramatic improvement in the reliability of calculations of flow conditions for the described fluid cell.

The Reynolds number calculation for flow is estimated from the following equation:

$$(Eq. 22) \quad Re = \frac{\rho v D_c}{\mu}$$

with the following values for water density $\rho \sim 1 \text{ g/cm}^3$, velocity $v \sim 500 \text{ }\mu\text{m/s}$, viscosity $\mu \sim 1 \text{ mPa}\cdot\text{s}$, and

$$(Eq. 23) \quad D_c = \frac{2wh}{w+h} \sim 107 \text{ }\mu\text{m},$$

resulting in a $Re \sim 0.05$. Computational fluid dynamics simulations of a Veeco fluid cell with a similar flow velocity calculate a $Re \sim 15$ [98]. A conservative shear rate of 10Hz was demonstrated; however, higher shear rates are certainly possible. Importantly for applications requiring high shear rates, we can also operate at flow velocities 300 times greater and still achieve similar laminar flow of traditional liquid cells.

The calculated volume enclosed by the channel is $\sim 50 \text{ nL}$. For comparison, the volume of Veeco Multimode liquid cell, the next smallest in volume, is over three orders of magnitude larger. The reduced volume of the flow cell may allow AFM visualization of very precious samples at high concentration, for example in experiments of in situ or ex vivo binding of soluble proteins to surfaces [104], [108]. Therefore, experiments involving the constant flow

of protein can be recorded for 3 orders of magnitude longer imaging times, or alternatively at much higher protein concentrations, than the same experiment conducted on a traditional liquid cell. The real time visualization of crystal growth can also substantially benefit from a microfluidic liquid cell as the efficiency of crystal growth is enhanced by confined liquid environments due to the suppression of natural convection resulting from the drastic decreases of the Grashof number [109].

The force curve data show reasonable linearity in the z-axis. However, scans in x- and y-axis did show significant nonlinearity and hysteresis, especially for large scans. In general, scans in the direction of the channel that were over 10 μm could not be reliably completed. Because our device is embedded in a soft PDMS polymer, motion of the vertical piezo actuator during a force curve may cause both cantilever deflection as well as compression of the PDMS surrounding the embedded probe. Noise may be reduced by selection of a soft cantilever and fabrication of stiff PDMS. Moreover, scans perpendicular to the channel revealed nonlinear effects at distances of less than 4 μm . Therefore, the current design is only suitable for imaging over limited scan sizes. The nonlinearity is primarily a result of the strong mechanical coupling between the gasket, which undergoes significant strain, and the probe die. We believe this problem can be alleviated with a new design that minimizes this coupling. For example, future designs could utilize a substantially softer gasket material or improved form factor. Nonetheless, imaging with the microfluidic liquid cell will likely be limited to dimensions that are a fraction of the channel width.

4.12 CONCLUSIONS

A liquid cell is developed that integrates a microfluidic channel around a cantilever for atomic force microscopy in aqueous environment. The device is used to record force-distance curves as well as to obtain high resolution contact mode images—both critical demonstrations of AFM capability. The volume encapsulated by the fluid cell is below 50nL and we believe further reduction in liquid volume can be achieved. This design succinctly combines batch-fabricated microcantilevers with batch-fabricated microfluidic channels.

CHAPTER 5 CONCLUSIONS

5.1 SUMMARY

This work demonstrates original MEMS fabrication techniques toward a comprehensive multimodal AFM system for single cell analysis. The first high sensitivity, low stiffness nanofluidic channel is developed leveraging the capabilities of thermally decomposable polymer to form longer channels with smaller cross sectional areas. Numerical and FEA models were developed for a channeled micro cantilever. The numerical model was used to perform a parametric analysis that would identify the key parameters contributing to the markedly stiff probes described in the literature. A low stiffness hollow cantilever could be realized by reducing the top layer thickness, the channel dimensions, and longer cantilevers. The technique allows for fabrication to the following parameters which are necessary for achieving the low stiffness.

- Topcoat thickness < 400nm
- Channel thickness < 400nm
- Channel width < 3 μ m
- Cantilever length > 230 μ m

To achieve a small bending modulus, a thermally decomposable polymer is used as the sacrificial layer. A major challenge with this technique is that the overcoat layer must be deposited using a low temperature process. The PECVD nitride overcoat can be deposited at temperatures as low as 100 °C. However, the film quality is poor, having residual stresses as high as 157.22 MPa. This is contrasted with the high quality film of the base layer, deposited

using a low stress LPCVD method, which has a residual stress less than 100 MPa compressive and can be tailored to have tensile stress. The thermal mismatch of these materials induces a bending radius and tip deflections on the order of 100's of microns. It was hypothesized that the net residual stress of the composite material cantilever can be reduced by setting the residual stress of each film to have complementary polarity, for example a tensile base layer and compressive overcoat. However, we find that this approach is not satisfactory, as the interfacial stress is sufficient to cause stress fracturing at the features. It is shown numerically that a layer's contribution to the bending moment could be enhanced by increasing its thickness. By this logic, the base layer with its lower residual stress could be made to dominate. However, this approach increases the cantilever thickness to the third power according to the model. The third approach is to perform an anneal, provided the high temperatures required for this step are conducive with the overall process flow. It has been shown that annealing at temperatures as low as 800 °C will densify the PECVD nitride, thus decreasing its residual stress. Here, a 900 °C anneal was performed, altering the overall process to allow for high temperature processing. A low stress hollowed cantilever is realized. Stiffness values of three different cantilever lengths were measured and shown to align with the numerical model. Mitigation of the beam residual stress caused by low temperature deposition of PECVD nitride can be achieved by

- depositing tensile LPCVD and a compressive PECVD allowing their composite stresses to complement each other.
- manipulating the layer thickness to control the distance of the local centroid the neutral axis and, therefore, its contribution to the bending moment.
- annealing after channel decomposition, which densifies the PECVD.

To integrate the cantilever into an AFM system and control pressure at the cantilever terminus, two key fabrication challenges needed to be overcome. The first was how to connect the 305 μm diameter glass capillary from the pressure control system directly into the die of the probe. This allows the probe to be used on any brand AFM, without destructive modification to the probe holder or the need to give up the complex capabilities of current holders on the market. An original side entry technique is demonstrated. The second challenge is how to connect the surface based nanofluidic channel to the subsurface microfluidic channel. For this, two original fabrication methods are demonstrated. The key distinction between the two processes comes down to fabrication ease and repeatability versus fabrication throughput. The oxide etch-stop approach is more attractive in terms of fabrication as it is far more repeatable and forgiving, which is more ideal for non-industry based cleanrooms of lower equipment quality control and cases where throughput is not of primary concern. The second method employs a set of entirely wafer level processing techniques for higher throughput. This technology demonstrates potential for other lab-on-chip microstructures for which channel cross sectional area is to be leveraged for testing at high shear rates and laminar flow conditions coupled with sensor systems in both aqueous and nonaqueous environments.

A liquid cell was developed that integrates a microfluidic channel around a cantilever for atomic force microscopy in aqueous environment. The device is used to record force-distance curves as well as to obtain high resolution contact mode images—both critical demonstrations of AFM capability. The volume encapsulated by the fluid cell is below 50nL.

and we believe further reduction in liquid volume can be achieved. This design succinctly combines batch-fabricated microcantilevers with batch-fabricated microfluidic channels.

5.2 KEY ACHIEVEMENTS

Ultimately, several new concepts are proposed toward development of an AFM based assay that combines a spectrum of AFM capabilities into a comprehensive multimodal single cell analysis, by simultaneous measurement of mass, compressive modulus, viscoelasticity, tensile modulus, and adhesion simultaneously in a single experiment. This work extends on the current microfabrication technology of fluidic AFM probes with the following original contributions:

- The first high resolution (1.87 pN noise floor), low stiffness ($k = 53.54$ pN/nm) nano-channel cantilever made from thermally decomposable sacrificial polymer. The probe stiffness is 2 orders of magnitude more force sensitive than that published to date, and is comparable to standard COTS probes for the application of cell stiffness measurements.
- A parametric analysis of the hollow cantilever that highlights critical design features to minimize beam stiffness.
- Two original methods of interfacing a bulk microfluidic channel to a surface nanofluidic channel via a thermally decomposable polymer.
- An integrated analogue pressure control system developed using an original side-entry interconnect structure for direct-to-chip connection of glass capillary for fluidic probes as well as other lab on chip applications.

- An original liquid cell was developed that integrates a 50nL microfluidic channel around a cantilever for atomic force microscopy in aqueous environment. This is a reduction of over 3-5 orders of magnitude compared to several commercial liquid cells. This device facilitates testing at high shear rates and laminar flow conditions coupled with full AFM functionality in microfluidic aqueous environments, including execution of both force displacement curves and high resolution imaging.

5.3 FUTURE CHARACTERIZATION

With regard to fabrication, various characterizations will need to be performed to optimize the fabrication process for better performing probes. As cantilever residual stress and bending radius is a function of all films and substrates in the stack, an investigation on the bond technique as it relates to the stressed induced through the stack. Further, the PECVD film density has a known dependency on deposition rate [59], [110]; therefore, a low deposition rate may be used to aid in stress reduction. Additionally, the thickness and quality of the PECVD nitride topcoat over the well may impose limits on the range or pressure that may be applied to the system. Though preliminary estimations were derived from finite element models, an empirical characterization will enhance the design as well as point to, perhaps, a strength of the two-step unity fabrication approach described, as it enables fabrication of smaller and higher fidelity wells which don't require the PECVD nitride layer to span as large an area.

With regard to device performance, fluid within the channel is expected to affect the cantilever stiffness and kinematic behavior. The additional fluid mass will decrease the resonant

frequency and correspondingly increase the stiffness. Further, the fluidic pressure at the terminus is expected to be affected by cantilever bending. At large cantilever deflections relative to the cantilever length, the channel volume may vary such that the terminus pressure may not maintain an under pressure required for aspiration.

The continuing goal of the lab is to perform biological experiments with this device which will demonstrate its potential for a comprehensive multimodal single cell analysis. Future work will thus focus on the integration of microfluidic networks in a complete sensor microsystem. As surface properties are a major concern, the characterization and the control of physicochemical properties of silicon nitride channels should also be considered.

5.4 LIMITATIONS

The fabrication techniques described within this work enable significant performance enhancements; however, the techniques also introduce challenges beyond that which were mitigated and described in this dissertation. Most critically, the use of a Unity as a sacrificial channel imposes a low temperature limitation of less than 250 °C on subsequent processing conditions. Further, the Unity leaves a residue that requires harsh acid to remove. This may require additional surface treatment such as DI flush and beta-mercaptoethanol (BME) surface activation to reduce toxic chemistry in preparation for bio assays. In comparison with the fabrication techniques described in literature in which LPCVD nitride forms the cantilever in a single step, the use PECVD for top coat requires not only that wafers be processed separately in a small batch process, it is an additional step. A benefit however is that the thickness of the top and bottom layers may be different as was shown to be an important factor for reducing

stiffness. Additionally, PECVD processes exist that allow for real time observation of nitride thickness during deposition which enables precise end-point thickness detection, which is not possible with current LPCVD equipment. While the probe fabrication is based on batch techniques, the process of inserting the capillary is not. Practice and skill is required complete this step.

With regard to device design, the demonstrated probe does not contain a tip in the current design; this however, may be reasonably incorporated into the process flow using established techniques. Additionally, the location of the orifice is located at the probe terminus. For normal loading of cells, the orifice would be ideally placed at the bottom surface of the cantilever near the end. Finally, this integrated fluidic system only illustrates a single fluidic cantilever. It would be possible and useful, however, to incorporate multiple cantilevers on the same die.

Though a parametric optimization for mass measurement was not within the scope of this study, we should note the following. A low k cantilever will provide a lower fidelity mass measurement; however, the proposed fabrication techniques within this thesis also produce an overall cantilever weight far less than that of Manalis *et al*, 2007. This reduction in cantilever mass refines the frequency measurement to approach the thermomechanical noise floor. Theoretically, this should allow for higher fidelity and enable mass measurement changes of 1ag [18].

5.5 RECOMMENDED EXPERIMENTS

5.5.1 ASPIRATION AND SERIAL STIFFNESS MEASUREMENT ON SINGLE, NON-ADHERENT CELL USING THE AFP

The primary goal of this study is to demonstrate cell aspiration and perform serial cell force measurements on the same cell in dissimilar environments. Enabled by the ability to manipulate non-adherent cells, the measurement is performed on a cell that is floating within the media and brought to a glass slide surface and the first measurement is taken. A separate cell having different cell stiffness is then aspirated and measured in the same manner. We chose to investigate the K562 cell line. The hypothesis is that the relationship between cell stiffness and adhesion is degrading in nature due to decreased receptor ligand interaction for stiffer cells (Figure 5-1). This interaction may be analogous to a car tires friction and air pressure, for example.

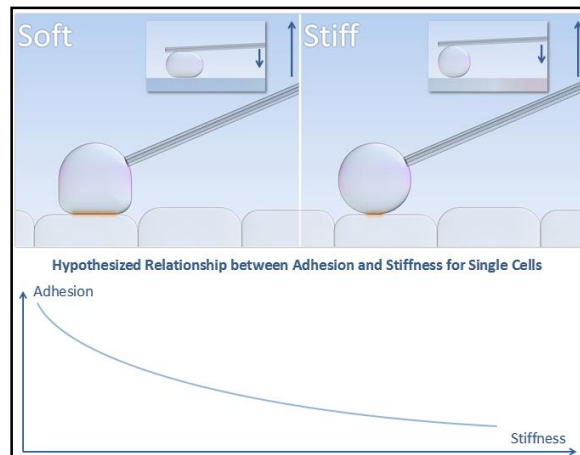


Figure 5-1 Hypothesized Adhesion and Stiffness Relationship for Single Cell as it depends on receptor-ligand contact under compressive force.

5.5.2 SINGLE CELL MEASUREMENT OF VOCs VIA MICROGC UNDER ELICITED CHEMICAL AND PHYSICAL STRESS

All plants are capable of releasing volatile organic compounds (VOC's). Plants emit a wide spectrum of volatile compounds for attraction of pollinators, such as bees and butterflies in response to herbavory [111]. Furthermore, plants will emit VOC's that attract predators in response to biotic and abiotic stress [112]. For example, leaf worms such as the *Spodoptera littoralis*, can induce emission of VOC's from the plant that then attract predators such as moths as a self-defense mechanism [113]. The direct measurement of elicited responses of single cells enables researchers to understand the function and identify the associated genes more quickly. This will allow for faster development of engineered genetic solutions as well as early detection of disease in farmed plants which would normally not be discovered until after irreversible damage has occurred. For the majority of known responses, the exact mechanism remains elusive [113]. With the ability to directly deliver media to and acquire media from a

single cell, as well as easily integrate the AFP with any external fluidic system via a glass capillary, this device would enable the first ever MicroGC analysis of a single cell before and after stimulation. A SPME compatible fluidic system is spliced in line with the glass capillary of the AFP fluidic system.

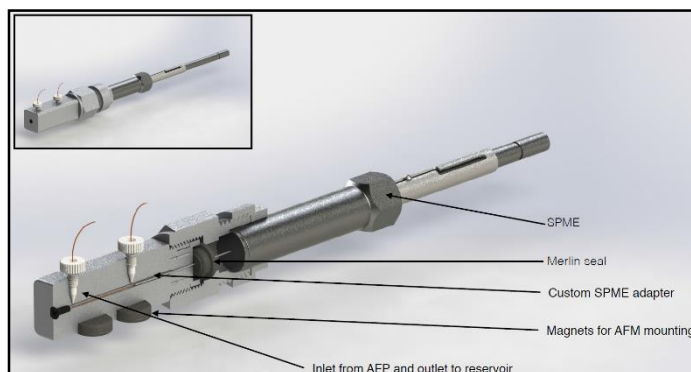


Figure 5-2 Custom SPME Adapter: The adapter is spliced in line with the existing 305 μm diameter glass capillary. The sorbent fiber of the GC is placed directly in line with the aspirated gases and VOC's.

5.5.3 FLAGELLATED CELL THRUST AND SPERM FUSION BINDING AFFINITY

Flagellar movement has been described as the fundamental expression of the vitality of a sperm cell [114]. The World Health Organization describes a sperm as grade-a if its velocity is greater than or equal to $25\mu\text{m/s}$ [115]. Sperm cells have a normal velocity of $100\mu\text{m/s}$ and exhibit a 125% increase as they approach the zona pellucida (ZP) of the oocyte [115]. The dynamics of this approach are complex and critical for binding, fusion and thus fertilization. Many parameters dictate successful fertilization including sperm velocity, density of forward facing receptors, radius of sperm head, length of sperm flagellum, elastic modulus of oocyte, and receptor-ligand bond energy. Of particular interest is the receptor located on the

spermatozoon head binds to ZP3 ligands on the oocyte [116]. A correlation may be made between quantifiable sperm traits and its genes to determine the genetic predisposition. To date, mostly theoretical estimations of sperm thrust exists [117]. Efforts to directly quantify these forces have been performed using optical tweezers [118], and AFM measurement of flagellum whip force [119]. However, enabled by the ability to perform force measurements by cellular aspiration without specifically binding a cell, the first ever direct measurement of thrust forces of a single flagellated cell is proposed.

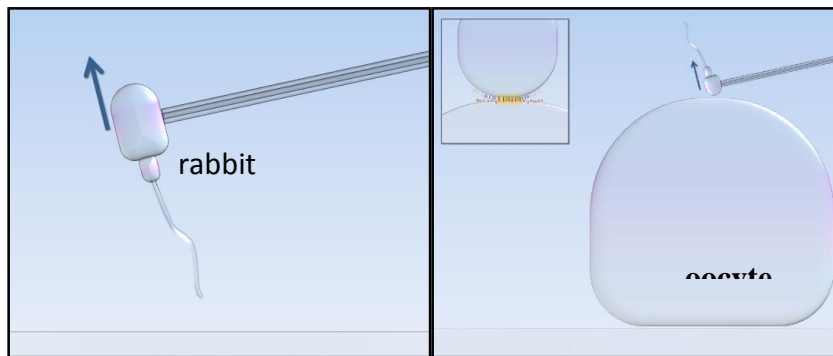


Figure 5-3 Spermatozoa Assay: (left) thrust force and (right) fusion binding affinity.

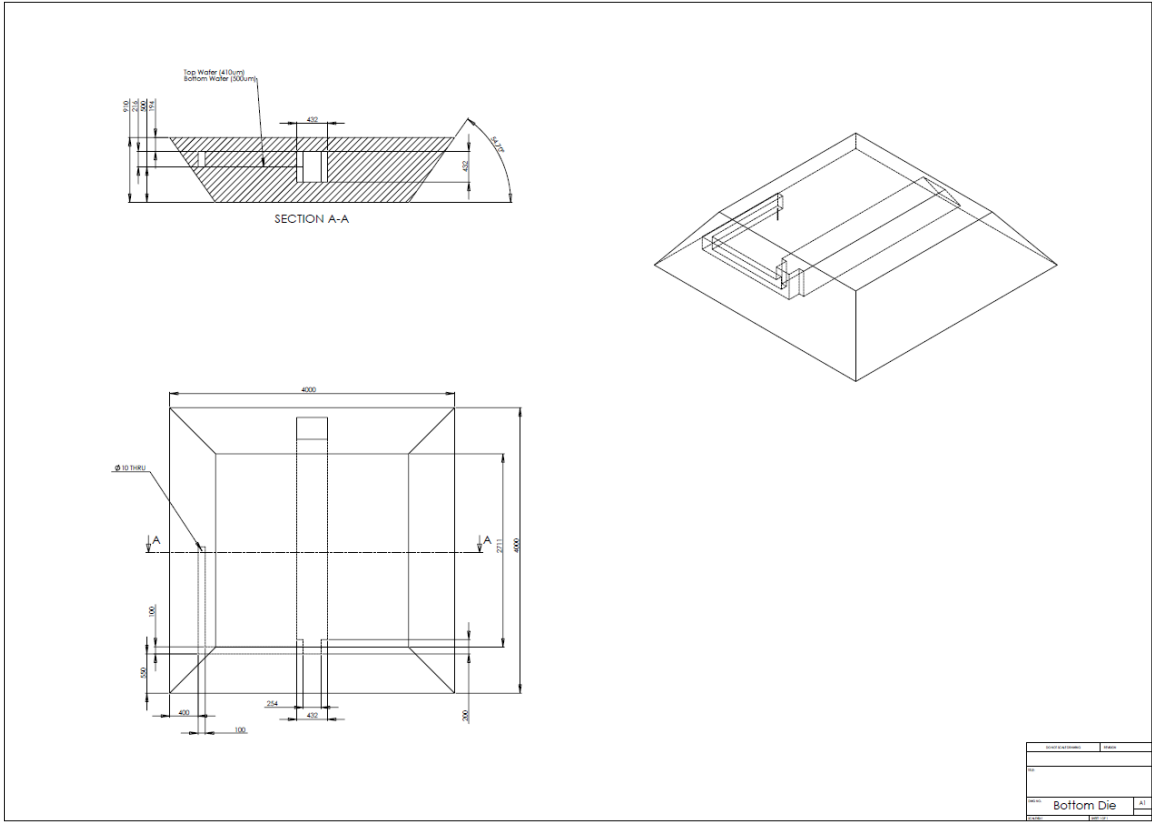
APPENDICES

Appendix A Values for parametric design of low stiffness cantilever

		w_B (μm)	t_B (nm)	w_C (μm)	t_C (nm)	w_T (μm)	t_T (nm)	l (μm)
Rectangular Cantilever	blue line	20	*	n/a	n/a	n/a	n/a	n/a
Range with traditional methods	red zone	20	*	19	1	20	200-700	n/a
Range using sacrificial polymer	orange zone	20	*	2	1	8	200-700	n/a
Commercial Probes (Bruker MSCT)	blue diamond	20	550nm	n/a	n/a	n/a	n/a	210
Objective	orange diamond	20	300	3	300	8	300	260-320
Dorig <i>et al</i> (2010)	red diamond	25	300	24.4	1	24.4	300	150

*varies according to the abscissa

Appendix B AFP Chip Architecture



Appendix D Layer processing parameters

Parameter \ Layer	ICP PECVD Nitride 200C	Oxford ICP PECVD	LS-LPCVD Nitride (100:17)	LS-LPCVD Nitride (100:15)
Tool	Oxford ICP PECVD	Oxford ICP PECVD	Tystar Nitride Furnace 4	Tystar Nitride Furnace 4
Pressure (mTorr)	10	10	158	158
He Leakup (mTorr)	0	0	--	--
Step Time (s)	0	0	0	0
Table (C)	100	200	830	830
Gas 1, Rate (sccm)	SiH ₄ , 14.1	SiH ₄ , 14.5	DCS, 100	DCS, 100
Gas 2, Rate (sccm)	N ₂ Blend, 12	N ₂ Blend, 12	NH ₃ , 17	NH ₃ , 15
Gas 3, Rate (sccm)	--	--	--	--
RF (W)	1	1	--	--
ICP (W)	500	550	--	--

REFERENCES

- [1] G. Binnig, C. F. Quate, and C. Gerber, “Atomic Force Microscope,” *Phys. Rev. Lett.*, vol. 56, no. 9, pp. 930–933, Mar. 1986.
- [2] J. E. Sader, J. A. Sanelli, B. D. Adamson, J. P. Monty, X. Wei, S. A. Crawford, J. R. Friend, I. Marusic, P. Mulvaney, and E. J. Bieske, “Spring constant calibration of atomic force microscope cantilevers of arbitrary shape,” *Rev Sci Instrum*, vol. 83, no. 10, p. 103705, Oct. 2012.
- [3] W. Xu, R. Mezencev, B. Kim, L. Wang, J. McDonald, and T. Sulchek, “Cell Stiffness Is a Biomarker of the Metastatic Potential of Ovarian Cancer Cells,” *PLoS ONE*, vol. 7, no. 10, p. e46609, Oct. 2012.
- [4] “Dynamic force spectroscopy of parallel individual Mucin1–antibody bonds.” [Online]. Available: <http://www.pnas.org/content/102/46/16638.short>. [Accessed: 07-Nov-2015].
- [5] W. Xu, R. Mezencev, B. Kim, L. Wang, J. McDonald, and T. Sulchek, “Cell Stiffness Is a Biomarker of the Metastatic Potential of Ovarian Cancer Cells,” *PLOS ONE*, vol. 7, no. 10, p. e46609, Oct. 2012.
- [6] T. Bongiorno, J. Kazlow, R. Mezencev, S. Griffiths, R. Olivares-Navarrete, J. F. McDonald, Z. Schwartz, B. D. Boyan, T. C. McDevitt, and T. Sulchek, “Mechanical stiffness as an improved single-cell indicator of osteoblastic human mesenchymal stem cell differentiation,” *Journal of Biomechanics*, vol. 47, no. 9, pp. 2197–2204, Jun. 2014.

- [7] E. Evans, K. Ritchie, and R. Merkel, “Sensitive force technique to probe molecular adhesion and structural linkages at biological interfaces,” *Biophysical Journal*, vol. 68, no. 6, pp. 2580–2587, Jun. 1995.
- [8] A. Ashkin, J. M. Dziedzic, and T. Yamane, “Optical trapping and manipulation of single cells using infrared laser beams,” , *Published online: 31 December 1987; / doi:10.1038/330769a0*, vol. 330, no. 6150, pp. 769–771, Dec. 1987.
- [9] B. Ladoux, E. Anon, M. Lambert, A. Rabodzey, P. Hersen, A. Buguin, P. Silberzan, and R.-M. Mège, “Strength Dependence of Cadherin-Mediated Adhesions,” *Biophysical Journal*, vol. 98, no. 4, pp. 534–542, Feb. 2010.
- [10] A. C. Martin, M. Kaschube, and E. F. Wieschaus, “Pulsed contractions of an actin–myosin network drive apical constriction,” *Nature*, vol. 457, no. 7228, pp. 495–499, Jan. 2009.
- [11] O. Chaudhuri, S. H. Parekh, W. A. Lam, and D. A. Fletcher, “Combined atomic force microscopy and side-view optical imaging for mechanical studies of cells,” *Nature Methods*, vol. 6, no. 5, pp. 383–387, 2009.
- [12] “Department of Physics, Cavendish Laboratory - Micromechanics and Optical Manipulation.” [Online]. Available: <http://www.phy.cam.ac.uk/research/bss/mmom.php>. [Accessed: 16-Nov-2013].
- [13] J.-L. Maître and C.-P. Heisenberg, “The role of adhesion energy in controlling cell–cell contacts,” *Current Opinion in Cell Biology*, vol. 23, no. 5, pp. 508–514, Oct. 2011.
- [14] J. Helenius, C.-P. Heisenberg, H. E. Gaub, and D. J. Muller, “Single-cell force spectroscopy,” *J Cell Sci*, vol. 121, no. 11, pp. 1785–1791, Jun. 2008.

- [15] T. Sulchek, R. W. Friddle, and A. Noy, "Strength of Multiple Parallel Biological Bonds," *Biophysical Journal*, vol. 90, no. 12, pp. 4686–4691, Jun. 2006.
- [16] A. Hategan, R. Law, S. Kahn, and D. E. Discher, "Adhesively-Tensed Cell Membranes: Lysis Kinetics and Atomic Force Microscopy Probing," *Biophysical Journal*, vol. 85, no. 4, pp. 2746–2759, Oct. 2003.
- [17] R. E. Mahaffy, S. Park, E. Gerde, J. Käs, and C. K. Shih, "Quantitative Analysis of the Viscoelastic Properties of Thin Regions of Fibroblasts Using Atomic Force Microscopy," *Biophysical Journal*, vol. 86, no. 3, pp. 1777–1793, Mar. 2004.
- [18] T. P. Burg, M. Godin, S. M. Knudsen, W. Shen, G. Carlson, J. S. Foster, K. Babcock, and S. R. Manalis, "Weighing of biomolecules, single cells and single nanoparticles in fluid," *Nature*, vol. 446, no. 7139, pp. 1066–1069, Apr. 2007.
- [19] S. R. Hassock, M. X. Zhu, C. Trost, V. Flockerzi, and K. S. Authi, "Expression and role of TRPC proteins in human platelets: evidence that TRPC6 forms the store-independent calcium entry channel," *Blood*, vol. 100, no. 8, pp. 2801–2811, Oct. 2002.
- [20] S. E. Chesla, P. Selvaraj, and C. Zhu, "Measuring Two-Dimensional Receptor-Ligand Binding Kinetics by Micropipette," *Biophysical Journal*, vol. 75, no. 3, pp. 1553–1572, Sep. 1998.
- [21] Andre Meister, Michael Gabi, Pascal Behr, Philipp Studer, Janos Voeroes, Philippe Niedermann, J. Bitterli, J. Polesel-Maris, M. Liley, H. Heinzelmann, and Tomaso Zambelli, "FluidFM: Combining Atomic Force Microscopy and Nanofluidics in a Universal Liquid Delivery System for Single Cell Applications and Beyond," *Nano Lett.*, vol. 9, no. 6, pp. 2501–2507, Jun. 2009.

- [22] A. Meister, M. Liley, J. Brugger, R. Pugin, and H. Heinzelmann, “Nanodispenser for attoliter volume deposition using atomic force microscopy probes modified by focused-ion-beam milling,” *Applied Physics Letters*, vol. 85, no. 25, pp. 6260–6262, 2004.
- [23] S. Deladi, J. W. Berenschot, N. R. Tas, G. J. M. Krijnen, J. H. de Boer, M. J. de Boer, and M. C. Elwenspoek, “Fabrication of micromachined fountain pen with in situ characterization possibility of nanoscale surface modification,” *J. Micromech. Microeng.*, vol. 15, no. 3, p. 528, Mar. 2005.
- [24] B. R. Davis, J. Yannariello-Brown, N. L. Prokopishyn, Z. Luo, M. R. Smith, J. Wang, N. D. Carsrud, and D. B. Brown, “Glass needle-mediated microinjection of macromolecules and transgenes into primary human blood stem/progenitor cells,” *Blood*, vol. 95, no. 2, pp. 437–444, Jan. 2000.
- [25] D. J. Stephens and R. Pepperkok, “The many ways to cross the plasma membrane,” *PNAS*, vol. 98, no. 8, pp. 4295–4298, Apr. 2001.
- [26] P. Dörig, P. Stiefel, P. Behr, E. Sarajlic, D. Bijl, M. Gabi, J. Vörös, J. A. Vorholt, and T. Zambelli, “Force-controlled spatial manipulation of viable mammalian cells and micro-organisms by means of FluidFM technology,” *Applied Physics Letters*, vol. 97, no. 2, pp. 023701–023701–3, Jul. 2010.
- [27] E. Potthoff, O. Guillaume-Gentil, D. Ossola, J. Polesel-Maris, S. LeibundGut-Landmann, T. Zambelli, and J. A. Vorholt, “Rapid and Serial Quantification of Adhesion Forces of Yeast and Mammalian Cells,” *PLoS ONE*, vol. 7, no. 12, p. e52712, Dec. 2012.

- [28] R. Meszaros, B. Merle, M. Wild, K. Durst, M. Göken, and L. Wondraczek, "Effect of thermal annealing on the mechanical properties of low-emissivity physical vapor deposited multilayer-coatings for architectural applications," *Thin Solid Films*, vol. 520, no. 24, pp. 7130–7135, Oct. 2012.
- [29] T. R. Albrecht, S. Akamine, T. E. Carver, and C. F. Quate, "Microfabrication of cantilever styli for the atomic force microscope," *Journal of Vacuum Science & Technology A: Vacuum, Surfaces, and Films*, vol. 8, no. 4, pp. 3386–3396, 1990.
- [30] D. P. E. Smith, "Limits of force microscopy," *Review of Scientific Instruments*, vol. 66, no. 5, p. 3191, May 1995.
- [31] C. M. Franz and P.-H. Puech, "Atomic Force Microscopy: A Versatile Tool for Studying Cell Morphology, Adhesion and Mechanics," *Cel. Mol. Bioeng.*, vol. 1, no. 4, pp. 289–300, Dec. 2008.
- [32] D. Rugar and P. Hansma, "Atomic Force Microscopy," *Physics Today*, vol. 43, no. 10, pp. 23–30, 1990.
- [33] Z. Shao, J. Mou, D. M. Czajkowsky, J. Yang, and J.-Y. Yuan, "Biological atomic force microscopy: what is achieved and what is needed," *Advances in Physics*, vol. 45, no. 1, pp. 1–86, 1996.
- [34] T. G. Kuznetsova, M. N. Starodubtseva, N. I. Yegorenkov, S. A. Chizhik, and R. I. Zhdanov, "Atomic force microscopy probing of cell elasticity," *Micron*, vol. 38, no. 8, pp. 824–833, Dec. 2007.
- [35] D. Sarid, *Scanning Force Microscopy*. Oxford University Press.
- [36] K. Babaei Gavan, H. J. R. Westra, E. W. J. M. van der Drift, W. J. Venstra, and H. S. J. van der Zant, "Size-dependent effective Young's modulus of silicon nitride

- cantilevers,” *Applied Physics Letters*, vol. 94, no. 23, pp. 233108–233108–3, Jun. 2009.
- [37] R. J. Cannara, M. Eglin, and R. W. Carpick, “Lateral force calibration in atomic force microscopy: A new lateral force calibration method and general guidelines for optimization,” *Review of Scientific Instruments*, vol. 77, no. 5, p. 053701, May 2006.
- [38] T. Sulchek, “Deflection Sensitivity Dependence on Geometry,” 02-Oct-2013.
- [39] T. Fukuma, J. I. Kilpatrick, and S. P. Jarvis, “Phase modulation atomic force microscope with true atomic resolution,” *Review of Scientific Instruments*, vol. 77, no. 12, p. 123703, Dec. 2006.
- [40] B. Mokaberi and A. A. G. Requicha, “Towards automatic nanomanipulation: drift compensation in scanning probe microscopes,” in *2004 IEEE International Conference on Robotics and Automation, 2004. Proceedings. ICRA '04*, 2004, vol. 1, pp. 416–421 Vol.1.
- [41] N. R. Devlin and D. K. Brown, “Fabricating millimeter to nanometer sized cavities concurrently for nanofluidic devices,” *Journal of Vacuum Science Technology B: Microelectronics and Nanometer Structures*, vol. 28, no. 6, pp. C6I7–C6I10, 2010.
- [42] Y. Koyata, M. Ikeuchi, and K. Ikuta, “Sealless 3-D microfluidic channel fabrication by sacrificial caramel template direct-patterning,” in *2013 IEEE 26th International Conference on Micro Electro Mechanical Systems (MEMS)*, 2013, pp. 311–314.

- [43] A. W. Martinez, S. T. Phillips, M. J. Butte, and G. M. Whitesides, "Patterned Paper as a Platform for Inexpensive, Low-Volume, Portable Bioassays," *Angewandte Chemie International Edition*, vol. 46, no. 8, pp. 1318–1320, 2007.
- [44] K. Ren, J. Zhou, and H. Wu, "Materials for Microfluidic Chip Fabrication," *Acc. Chem. Res.*, vol. 46, no. 11, pp. 2396–2406, Nov. 2013.
- [45] O. A. Saleh and L. L. Sohn, "An Artificial Nanopore for Molecular Sensing," *Nano Lett.*, vol. 3, no. 1, pp. 37–38, Jan. 2003.
- [46] J. Han and H. G. Craighead, "Separation of Long DNA Molecules in a Microfabricated Entropic Trap Array," *Science*, vol. 288, no. 5468, pp. 1026–1029, May 2000.
- [47] M. K. Ghatkesar, H. H. P. Garza, F. Heuck, and U. Staufer, "Scanning Probe Microscope-Based Fluid Dispensing," *Micromachines*, vol. 5, no. 4, pp. 954–1001, Oct. 2014.
- [48] C. Duan, W. Wang, and Q. Xie, "Review article: Fabrication of nanofluidic devices," *Biomicrofluidics*, vol. 7, no. 2, p. 026501, 2013.
- [49] R. Fan, R. Karnik, M. Yue, D. Li, A. Majumdar, and P. Yang, "DNA Translocation in Inorganic Nanotubes," *Nano Lett.*, vol. 5, no. 9, pp. 1633–1637, Sep. 2005.
- [50] C. Lee, E. H. Yang, N. V. Myung, and T. George, "A Nanochannel Fabrication Technique without Nanolithography," *Nano Lett.*, vol. 3, no. 10, pp. 1339–1340, Oct. 2003.

- [51] M. D. Wedlake and P. A. Kohl, "Thermal Decomposition Kinetics of Functionalized Polynorbornene," *Journal of Materials Research*, vol. 17, no. 03, pp. 632–640, 2002.
- [52] A. Faucheux, A. C. Gouget-Laemmel, P. Allongue, C. Henry-de-Villeneuve, F. Ozanam, and J.-N. Chazalviel, "Mechanisms of Thermal Decomposition of Organic Monolayers Grafted on (111) Silicon," *Langmuir*, vol. 23, no. 3, pp. 1326–1332, Jan. 2007.
- [53] M. G. Gupta, P. J. Joseph, and P. A. Kohl, "Photoacid generators for catalytic decomposition of polycarbonate," *J. Appl. Polym. Sci.*, vol. 105, no. 5, pp. 2655–2662, Sep. 2007.
- [54] P. A. Kohl, P. J. Joseph, H. Reed, S. Bidstrup-Allen, C. E. White, and C. Henderson, "Sacrificial compositions, methods of use thereof, and methods of decomposition thereof," US7052821 B2, 30-May-2006.
- [55] P. J. Joseph, H. A. Kelleher, S. A. B. Allen, and P. A. Kohl, "Improved fabrication of micro air-channels by incorporation of a structural barrier," *J. Micromech. Microeng.*, vol. 15, no. 1, p. 35, Jan. 2005.
- [56] P. Temple-Boyer, C. Rossi, E. Saint-Etienne, and E. Scheid, "Residual stress in low pressure chemical vapor deposition SiNx films deposited from silane and ammonia," *Journal of Vacuum Science & Technology A*, vol. 16, no. 4, pp. 2003–2007, Jul. 1998.
- [57] J. Laconte, D. Flandre, and J.-P. Raskin, *Micromachined Thin-Film Sensors for SOI-CMOS Co-Integration*. Springer Science & Business Media, 2006.

- [58] W. Fang and J. A. Wickert, "Determining mean and gradient residual stresses in thin films using micromachined cantilevers," *J. Micromech. Microeng.*, vol. 6, no. 3, p. 301, Sep. 1996.
- [59] D. Dergez, J. Schalko, A. Bittner, and U. Schmid, "Fundamental properties of a-SiNx:H thin films deposited by ICP-PECVD for MEMS applications," *Applied Surface Science*, vol. 284, pp. 348–353, Nov. 2013.
- [60] "Introduction to Microfabrication, Second Edition - Franssila." [Online]. Available:
about:reader?url=http%3A%2F%2Fonlinelibrary.wiley.com%2Fbook%2F10.1002%2F9781119990413. [Accessed: 10-Oct-2015].
- [61] "Chemical control of physical properties in silicon nitride films - Springer." [Online]. Available:
<http://link.springer.com.prx.library.gatech.edu/article/10.1007/s00339-012-7301-z>. [Accessed: 10-Oct-2015].
- [62] S. R. Quake and A. Scherer, "From Micro- to Nanofabrication with Soft Materials," *Science*, vol. 290, no. 5496, pp. 1536–1540, Nov. 2000.
- [63] K. Schoenwald and T. Sulchek, "Microfluidic to Nanofluidic Interface via a Thermally Decomposable Sacrificial Polymer," *Journal of Microelectromechanical Systems*, vol. PP, no. 99, pp. 1–1, 2015.
- [64] J. C. Bruyère, B. Reynes, C. Savall, and C. Roch, "Annealing of silicon nitride thin films prepared by plasma-enhanced chemical vapor deposition with helium dilution," *Thin Solid Films*, vol. 221, no. 1–2, pp. 65–71, Dec. 1992.

- [65] W. W. Flack, D. S. Soong, A. T. Bell, and D. W. Hess, "A mathematical model for spin coating of polymer resists," *Journal of Applied Physics*, vol. 56, no. 4, pp. 1199–1206, Aug. 1984.
- [66] L. M. Peurrung and D. B. Graves, "Film Thickness Profiles over Topography in Spin Coating," *J. Electrochem. Soc.*, vol. 138, no. 7, pp. 2115–2124, Jul. 1991.
- [67] S. A. Gupta and R. K. Gupta, "A Parametric Study of Spin Coating over Topography," *Ind. Eng. Chem. Res.*, vol. 37, no. 6, pp. 2223–2227, Jun. 1998.
- [68] A. D. Radadia, A. Salehi-Khojin, R. I. Masel, and M. A. Shannon, "The fabrication of all-silicon micro gas chromatography columns using gold diffusion eutectic bonding," *J. Micromech. Microeng.*, vol. 20, no. 1, p. 015002, Jan. 2010.
- [69] R. F. Wolffenbuttel, "Low-temperature intermediate Au-Si wafer bonding; eutectic or silicide bond," *Sensors and Actuators A: Physical*, vol. 62, no. 1–3, pp. 680–686, Jul. 1997.
- [70] S. Lani, A. Bosseboeuf, B. Belier, C. Clerc, C. Gousset, and J. Aubert, "Gold metallizations for eutectic bonding of silicon wafers," *Microsyst Technol*, vol. 12, no. 10–11, pp. 1021–1025, Sep. 2006.
- [71] Z. Zhu, M. Yu, Y. Zhu, P. Wang, C. Liu, W. Wang, M. Miao, J. Chen, and Y. Jin, "Low temperature Al based wafer bonding using Sn as intermediate layer," in *2012 13th International Conference on Electronic Packaging Technology and High Density Packaging (ICEPT-HDP)*, 2012, pp. 127–130.
- [72] C. H. Yun, J. Martin, L. Chen, and T. J. Frey, "Clean and Conductive Wafer Bonding for MEMS," *ECS Trans.*, vol. 16, no. 8, pp. 117–124, Oct. 2008.

- [73] Q.-Y. Tong and U. M. Gösele, “Wafer Bonding and Layer Splitting for Microsystems,” *Adv. Mater.*, vol. 11, no. 17, pp. 1409–1425, Dec. 1999.
- [74] X. X. Zhang and J.-P. Raskin, “Low-temperature wafer bonding: a study of void formation and influence on bonding strength,” *Journal of Microelectromechanical Systems*, vol. 14, no. 2, pp. 368–382, Apr. 2005.
- [75] K. Mitani and U. M. Gösele, “Formation of interface bubbles in bonded silicon wafers: A thermodynamic model,” *Appl. Phys. A*, vol. 54, no. 6, pp. 543–552, Jun. 1992.
- [76] A. Plöbbl and G. Kräuter, “Wafer direct bonding: tailoring adhesion between brittle materials,” *Materials Science and Engineering: R: Reports*, vol. 25, no. 1–2, pp. 1–88, Mar. 1999.
- [77] R. M. Hochmuth, “Micropipette aspiration of living cells,” *Journal of Biomechanics*, vol. 33, no. 1, pp. 15–22, Jan. 2000.
- [78] E. R. Murphy, T. Inoue, H. R. Sahoo, N. Zaborenko, and K. F. Jensen, “Solder-based chip-to-tube and chip-to-chip packaging for microfluidic devices,” *Lab Chip*, vol. 7, no. 10, pp. 1309–1314, Oct. 2007.
- [79] E. Meng, S. Wu, and Y.-C. Tai, “Silicon couplers for microfluidic applications,” *Fresenius J Anal Chem*, vol. 371, no. 2, pp. 270–275, Sep. 2001.
- [80] T. Humphreys, J. Andersson, U. Södervall, and T. Melvin, “World-to-chip interconnects for efficient loading of genomic DNA into microfluidic channels,” *J. Micromech. Microeng.*, vol. 19, no. 10, p. 105024, Oct. 2009.
- [81] R. Lo and E. Meng, “Integrated and reusable in-plane microfluidic interconnects,” *Sensors and Actuators B: Chemical*, vol. 132, no. 2, pp. 531–539, Jun. 2008.

- [82] D. Sabourin, D. Snakenborg, and M. Dufva, "Interconnection blocks: a method for providing reusable, rapid, multiple, aligned and planar microfluidic interconnections," *J. Micromech. Microeng.*, vol. 19, no. 3, p. 035021, Mar. 2009.
- [83] S. Jaffer and B. L. Gray, "Polymer mechanically interlocking structures as interconnects for microfluidic systems," *J. Micromech. Microeng.*, vol. 18, no. 3, p. 035043, Mar. 2008.
- [84] D. Sabourin, M. Dufva, T. Jensen, J. Kutter, and D. Snakenborg, "One-step fabrication of microfluidic chips with in-plane, adhesive-free interconnections," *J. Micromech. Microeng.*, vol. 20, no. 3, p. 037001, Mar. 2010.
- [85] B. . Gray, D. Jaeggi, N. . Mourlas, B. . van Drieënhuizen, K. . Williams, N. . Maluf, and G. T. . Kovacs, "Novel interconnection technologies for integrated microfluidic systems," *Sensors and Actuators A: Physical*, vol. 77, no. 1, pp. 57–65, Sep. 1999.
- [86] J. L. Hutter and J. Bechhoefer, "Calibration of atomic-force microscope tips," *Review of Scientific Instruments*, vol. 64, no. 7, pp. 1868–1873, Jul. 1993.
- [87] W. Zhou, J. Yang, Y. Li, A. Ji, and F. Yang, "Fracture properties of PECVD silicon nitride thin films by long rectangular membrane bulge test," in *3rd IEEE International Conference on Nano/Micro Engineered and Molecular Systems, 2008. NEMS 2008*, 2008, pp. 261–264.
- [88] H. Huang, K. J. Winchester, A. Suvorova, B. R. Lawn, Y. Liu, X. Z. Hu, J. M. Dell, and L. Faraone, "Effect of deposition conditions on mechanical properties of low-temperature PECVD silicon nitride films," *Materials Science and Engineering: A*, vol. 435–436, pp. 453–459, Nov. 2006.

- [89] M. Bahrami, M. M. Yovanovich, and J. R. Culham, "Pressure Drop of Fully-Developed, Laminar Flow in Microchannels of Arbitrary Cross-Section," *J. Fluids Eng.*, vol. 128, no. 5, pp. 1036–1044, Jan. 2006.
- [90] S. Takayama, W. Gu, J.-C. Meiners, H. Chen, and Y.-C. Tung, "Multiplexed microfluidic valve activator," WO2008016703 A1, 07-Feb-2008.
- [91] C. D. Blanchette, R. Law, W. H. Benner, J. B. Pesavento, J. A. Cappuccio, V. Walsworth, E. A. Kuhn, M. Corzett, B. A. Chromy, B. W. Segelke, M. A. Coleman, G. Bench, P. D. Hoeprich, and T. A. Sulchek, "Quantifying size distributions of nanolipoprotein particles with single-particle analysis and molecular dynamic simulations," *J. Lipid Res.*, vol. 49, no. 7, pp. 1420–1430, Jul. 2008.
- [92] P. E. Hillner, A. J. Gratz, S. Manne, and P. K. Hansma, "Atomic-scale imaging of calcite growth and dissolution in real time," *Geology*, vol. 20, no. 4, p. 359, 1992.
- [93] T. Wade, J. F. Garst, and J. L. Stickney, "A simple modification of a commercial atomic force microscopy liquid cell for in situ imaging in organic, reactive, or air sensitive environments," *Review of Scientific Instruments*, vol. 70, no. 1, pp. 121–124, Jan. 1999.
- [94] T. Sulchek, R. Hsieh, J. D. Adams, S. C. Minne, C. F. Quate, and D. M. Adderton, "High-speed atomic force microscopy in liquid," *Review of Scientific Instruments*, vol. 71, no. 5, pp. 2097–2099, May 2000.
- [95] G. Fu, S. R. Qiu, C. A. Orme, D. E. Morse, and J. J. De Yoreo, "Acceleration of Calcite Kinetics by Abalone Nacre Proteins," *Adv. Mater.*, vol. 17, no. 22, pp. 2678–2683, Nov. 2005.

- [96] S. R. Qiu and C. A. Orme, "Dynamics of Biomineral Formation at the Near-Molecular Level," *Chem. Rev.*, vol. 108, no. 11, pp. 4784–4822, Nov. 2008.
- [97] J. J. D. Yoreo, S. R. Qiu, and J. R. Hoyer, "Molecular modulation of calcium oxalate crystallization," *American Journal of Physiology - Renal Physiology*, vol. 291, no. 6, pp. F1123–F1132, Dec. 2006.
- [98] D. Gasperino, A. Yeckel, B. K. Olmsted, M. D. Ward, and J. J. Derby, "Mass Transfer Limitations at Crystallizing Interfaces in an Atomic Force Microscopy Fluid Cell: A Finite Element Analysis," *Langmuir*, vol. 22, no. 15, pp. 6578–6586, Jul. 2006.
- [99] B. Drake, C. B. Prater, A. L. Weisenhorn, S. A. Gould, T. R. Albrecht, C. F. Quate, D. S. Cannell, H. G. Hansma, and P. K. Hansma, "Imaging crystals, polymers, and processes in water with the atomic force microscope," *Science*, vol. 243, no. 4898, pp. 1586–1589, Mar. 1989.
- [100] S. A. C. Gould, B. Drake, C. B. Prater, A. L. Weisenhorn, S. Manne, G. L. Kelderman, H.-J. Butt, H. Hansma, P. K. Hansma, S. Magonov, and H. J. Cantow, "The atomic force microscope: A tool for science and industry," *Ultramicroscopy*, vol. 33, no. 2, pp. 93–98, Aug. 1990.
- [101] R. McKendry, J. Zhang, Y. Arntz, T. Strunz, M. Hegner, H. P. Lang, M. K. Baller, U. Certa, E. Meyer, H.-J. Güntherodt, and C. Gerber, "Multiple label-free biodetection and quantitative DNA-binding assays on a nanomechanical cantilever array," *PNAS*, vol. 99, no. 15, pp. 9783–9788, Jul. 2002.
- [102] M. Yue, H. Lin, D. E. Dedrick, S. Satyanarayana, A. Majumdar, A. S. Bedekar, J. W. Jenkins, and S. Sundaram, "A 2-D microcantilever array for multiplexed

- biomolecular analysis,” *Journal of Microelectromechanical Systems*, vol. 13, no. 2, pp. 290–299, Apr. 2004.
- [103] K. Schoenwald, Z. C. Peng, D. Noga, S. R. Qiu, and T. Sulchek, “Integration of atomic force microscopy and a microfluidic liquid cell for aqueous imaging and force spectroscopy,” *Review of Scientific Instruments*, vol. 81, no. 5, p. 053704, May 2010.
- [104] S. R. Qiu, A. Wierzbicki, C. A. Orme, A. M. Cody, J. R. Hoyer, G. H. Nancollas, S. Zepeda, and J. J. D. Yoreo, “Molecular modulation of calcium oxalate crystallization by osteopontin and citrate,” *PNAS*, vol. 101, no. 7, pp. 1811–1815, Feb. 2004.
- [105] B. A. Coles, R. G. Compton, J. Booth, Q. Hong, and G. H. W. Sanders, “A hydrodynamic AFM flow cell for the quantitative measurement of interfacial kinetics,” *Chem. Commun.*, no. 6, pp. 619–620, Jan. 1997.
- [106] T. Jung, X. Sheng, C. K. Choi, W.-S. Kim, J. A. Wesson, and M. D. Ward, “Probing Crystallization of Calcium Oxalate Monohydrate and the Role of Macromolecule Additives with in Situ Atomic Force Microscopy,” *Langmuir*, vol. 20, no. 20, pp. 8587–8596, Sep. 2004.
- [107] R. T. T. Gettens, Z. Bai, and J. L. Gilbert, “Quantification of the kinetics and thermodynamics of protein adsorption using atomic force microscopy,” *J. Biomed. Mater. Res.*, vol. 72A, no. 3, pp. 246–257, Mar. 2005.
- [108] L. Wang, W. Zhang, S. R. Qiu, W. J. Zachowicz, X. Guan, R. Tang, J. R. Hoyer, J. J. D. Yoreo, and G. H. Nancollas, “Inhibition of calcium oxalate monohydrate

- crystallization by the combination of citrate and osteopontin,” *Journal of Crystal Growth*, vol. 291, no. 1, pp. 160–165, May 2006.
- [109] C. L. Hansen, E. Skordalakes, J. M. Berger, and S. R. Quake, “A robust and scalable microfluidic metering method that allows protein crystal growth by free interface diffusion,” *PNAS*, vol. 99, no. 26, pp. 16531–16536, Dec. 2002.
- [110] A. Zhao, J. M. Bulger, L. P. Green, W. C. Harris, T. J. Hunt, W. R. Marchesseault, R. F. Shuman, M. C. French, and H. C. Lisy, “Improvement of film uniformity stability of PECVD silicon nitride deposition process by addition of fluorine removal to the plasma clean sequence,” in *Advanced Semiconductor Manufacturing Conference and Workshop, 2005 IEEE/SEMI*, 2005, pp. 143–148.
- [111] J. T. Knudsen, R. Eriksson, J. Gershenzon, and B. Ståhl, “Diversity and distribution of floral scent,” *Bot. Rev.*, vol. 72, no. 1, pp. 1–120, Jan. 2006.
- [112] M. E. Maffei, “Sites of synthesis, biochemistry and functional role of plant volatiles,” *South African Journal of Botany*, vol. 76, no. 4, pp. 612–631, Oct. 2010.
- [113] G. Arimura, R. Ozawa, T. Shimoda, T. Nishioka, W. Boland, and J. Takabayashi, “Herbivory-induced volatiles elicit defence genes in lima bean leaves,” *Nature*, vol. 406, no. 6795, pp. 512–515, Aug. 2000.
- [114] D. F. Katz, E. Z. Drobnis, and J. W. Overstreet, “Factors regulating mammalian sperm migration through the female reproductive tract and oocyte vestments,” *Gamete Research*, vol. 22, no. 4, pp. 443–469, 1989.
- [115] A. Gefen, “The Relationship Between Sperm Velocity and Pressures Applied to the Zona Pellucida During Early Sperm-Oocyte Penetration,” *Journal of Biomechanical Engineering*, vol. 132, no. 12, p. 124501, Nov. 2010.

- [116] P. Kozlovsky and A. Gefen, “The relative contributions of propulsive forces and receptor–ligand binding forces during early contact between spermatozoa and zona pellucida of oocytes,” *Journal of Theoretical Biology*, vol. 294, pp. 139–143, Feb. 2012.
- [117] D. J. Smith, E. A. Gaffney, H. Gadêlha, N. Kapur, and J. C. Kirkman-Brown, “Bend propagation in the flagella of migrating human sperm, and its modulation by viscosity,” *Cell Motility and the Cytoskeleton*, vol. 66, no. 4, pp. 220–236, Apr. 2009.
- [118] B. E. M, C. J. M, D. J. M, and A. A, “Force Production by Swimming Sperm Analysis Using Optical Tweezers,” *Journal of Cell Biology*, vol. 111, no. 5 PART 2, p. 421A, 1990.
- [119] V. Ierardi, A. Niccolini, M. Alderighi, A. Gazzano, F. Martelli, and R. Solaro, “AFM characterization of rabbit spermatozoa,” *Microscopy Research and Technique*, vol. 71, no. 7, pp. 529–535, 2008.

VITA

DAVID KIPP SCHOENWALD

Schoenwald was born in Fort Lauderdale, Florida. He earned a B.S in Mechanical Engineering at the University of Central Florida, Orlando, in 2007 before coming to Georgia Tech to pursue a doctorate in Bioengineering, earning a M.S in Mechanical Engineering along the way.